

Numerical studies on topological aspects of gauge theories

MATSUMOTO, Akira

*Department of Particle and Nuclear Physics,
School of High Energy Accelerator Science,
The Graduate University for Advanced Studies, SOKENDAI,
1-1 Oho, Tsukuba, Ibaraki 305-0801, Japan*

Abstract

The theta term reflects topological nature of gauge theories, and its effects are genuinely non-perturbative. Recent studies by 't Hooft anomaly matching presented some possible phase structures of 4D SU(2) gauge theory at $\theta = \pi$, which can be different from the known scenario at large N . It is an interesting challenge to reveal the phase structure by first-principle calculation. However, the Monte Carlo simulation of gauge theories with the theta term is known to be difficult due to the sign problem. Thus, our goal is to develop methods to investigate such theories avoiding the sign problem. First, we used the complex Langevin method (CLM) to simulate the theory directly for $\theta \neq 0$. We applied the CLM to 2D U(1) gauge theory, which can be solved analytically. We found that a naive implementation of the method fails due to the topological nature of the theory. We circumvented this problem by introducing a puncture and confirmed that the CLM can reproduce the exact results even at large θ . We also proved that the punctured model is equivalent to the infinite volume limit of the original model for $|\theta| < \pi$. Next, we applied the CLM to 4D SU(2) gauge theory. We used the stout smearing to deal with the contamination of the topological charge by short-range fluctuations. The effect of smearing is included dynamically in the CLM. We found, however, that the CLM becomes unstable due to topology changes. It seems to be difficult to study the phase structure by this method. We also propose an alternative approach to 4D SU(2) gauge theory based on analytic continuation of θ . We can obtain information of the phase structure at $\theta = \pi$ indirectly by the hybrid Monte Carlo method (HMC) with the imaginary theta term. We found that the result obtained in the high temperature region indicates the instanton gas behavior. We also obtained the result which is consistent with the spontaneous breaking of CP at low temperature.

Contents

1	Introduction	4
2	Lattice gauge theory with a theta term	6
2.1	2D U(1) gauge theory on the lattice	6
2.2	4D SU(2) gauge theory on the lattice	8
3	Complex Langevin analysis of 2D U(1) gauge theory	9
3.1	Application of the CLM to 2D U(1) gauge theory	10
3.2	Result of the CLM on the periodic lattice	12
3.3	Appearance of large drifts and topology change	14
3.4	Introducing a puncture on the torus	16
3.5	Application of the CLM to the punctured model	20
3.5.1	Drift terms for the punctured model	20
3.5.2	Distribution of the topological charge	20
3.6	Validity of the CLM for the punctured model	21
3.7	Behavior of the unitarity norm	23
3.8	Result of the CLM for the punctured model	26
4	Complex Langevin analysis of 4D SU(2) gauge theory	26
4.1	Application of the CLM to 4D SU(2) gauge theory	28
4.2	Result of CLM with the naive definition of the topological charge	30
4.3	Analyticity of the complex theta	32
4.4	Stout smearing in the CLM	32
4.5	Result of the CLM with the stout smearing	35
4.6	Origin of the large drift	36
5	4D SU(2) gauge theory with an imaginary theta	38
5.1	Conjectured phase diagram	39
5.2	Theta dependence of the topological charge density	40
5.3	Large volume limit	42
5.4	Continuum limit	42
5.5	Problem in the large theta region	44
6	Summary	45
A	Derivation of the partition function of 2D lattice gauge theories	48
A.1	K-functional	49
A.2	Partition function for the non-punctured model	52
A.3	Partition function for the punctured model	53
A.4	Evaluation of the observables	55
B	The punctured model with the sine definition Q_{\sin}	57
C	Derivation of the formulae for the stout smearing	58

1 Introduction

We can explore the topological nature of quantum field theories via topological terms. Recently, gauge theories with a theta term have been studied by 't Hooft anomaly matching. In particular, there is a constraint on the phase structure of 4D $SU(N)$ pure gauge theory by a 't Hooft anomaly involving CP and center symmetries at $\theta = \pi$ [1]. The constraint is consistent with the known scenario at large N , where the theory at $\theta = \pi$ is confined with spontaneously broken CP at low temperature and then has a transition to deconfined phase with restored CP at a finite temperature. However, it is highly nontrivial whether this structure persists for small N , since there are various ways to satisfy the anomaly matching condition. For example, the theory for small N at low temperature may be deconfined or gapless as well as spontaneously broken CP. Therefore it is an interesting challenge to investigate the phase structure by first-principle calculation at the smallest N , namely $N = 2$.

Since the effects of the theta term on quantum field theories are genuinely non-perturbative, the theory including the theta term should be analyzed by non-perturbative calculations. However, ordinary Monte Carlo simulations based on the lattice gauge theory is difficult due to the sign problem. The aim of this work is to develop a method to simulate gauge theories with a theta term avoiding the sign problem. Then, we try to reveal the phase structure of 4D $SU(2)$ gauge theory and test the consistency with the anomaly matching. In this work, we propose an approach using the complex Langevin method (CLM) [2, 3], which turns out to be useful for 2D gauge theories on a punctured torus. However, it is difficult to analyze 4D gauge theories by this method because the topological property is affected by UV fluctuations. Thus, we propose an alternative approach using analytic continuation of θ . We can access the phase structure for real θ from the simulations at imaginary θ . We found that this method can give us a lot of information in spite of the restriction by the phase boundary. We briefly explain our works in the following paragraphs.

First, we focus on the CLM, which is one of the approaches allowing us to avoid the sign problem. The advantage of this method is that the calculation cost depends just linearly on the system size, so that we can easily apply it to theories in higher dimensions. However, the CLM has the drawback that it possibly gives wrong results depending on the system and the parameter region. Fortunately, a practical criterion for correct convergence was proposed in the recent study [4]. Therefore, the CLM is now thought to be a useful method as long as the criterion is satisfied.

As a first step, we applied the CLM to 2D $U(1)$ gauge theory with a theta term [5]. This model is suitable for the testing ground since it can be solved analytically for a finite lattice spacing and a finite volume on an arbitrary manifold [6, 7, 8]. We found that a naive implementation of the CLM on the periodic lattice fails. We clarified that the configurations which appear when the topology change occurs during the simulation necessarily result in a large drift force. In fact, frequent appearance of the large drift force violates the criterion for correct convergence. If one avoids this problem by simply approaching the continuum limit, then the topology change never occurs during the simulation. It causes the other problem of the ergodicity.

In order to circumvent this problem, we introduced a puncture on the lattice, namely removing a plaquette from the action. It makes the manifold non-compact, so that the 2π periodicity of θ is lost. We obtained the exact results for this punctured model and proved that it is equivalent to the infinite volume limit of the original model within the range $|\theta| < \pi$. Thus, we can still extract the information of the original model from the punctured model. Rather surprisingly, we found that the CLM works and reproduces the exact results for the punctured model even at large θ . The topology change can occur freely thanks to the degrees of freedom around the puncture. As approaching the continuum limit, the large drift force does not appear because the problematic plaquette (puncture) is removed from the action.

Next, We analyzed 4D SU(2) gauge theory with a theta term by using the CLM [9]. This work is motivated by the prediction for the phase structure of the theory at $\theta = \pi$ by 't Hooft anomaly matching. The methods free from the sign problem, such as the CLM, allow us to calculate observables at $\theta \neq 0$ directly. We applied the CLM to the theory with the topological charge defined by the clover leaf formula [10] and found that it works in some cases. However, the topological property of the theory is unclear since the topological charge on the lattice is contaminated by the short-range fluctuations. It means that the topological charge does not approach an integer. The θ -dependent observables do not show the 2π periodicity. In fact, the situation is different from the case in 2D where the topological property is clear even on the finite lattice.

Then, we introduced the stout smearing [11] into the CLM in order to suppress the contamination of the topological charge. It successfully eliminates the short-range fluctuations, and the topological charge becomes close to an integer. However, we found that there is a relation between the topology change and the large drift force. They are correlated with each other just as we found in the study of 2D U(1) gauge theory. Thus, we need to modify the boundary condition of the 4D lattice to avoid this problem.

We are also studying 4D SU(2) gauge theory with an imaginary theta term. By considering analytic continuation, we can see the behavior of observables at real θ from the calculations at imaginary θ . Thus, it is possible to investigate the phase structure of the real θ region indirectly. Since the sign problem is absent in the theory with imaginary θ , we use the hybrid Monte Carlo (HMC) method. We also apply the stout smearing to the HMC in order to recover the topological property.

We found that the behavior of the topological charge density is consistent with the instanton gas approximation at high temperature, namely in the deconfined phase. We also obtained the result at low temperature, which is clearly different from those at high temperature. This result implies the spontaneous breaking of CP at $\theta = \pi$ in the confined phase. However, analytic continuation of the observables is valid only within the same phase. Thus, in this argument, we have to assume that the system remains in the same phase for $0 \leq \theta < \pi$. In other words, the θ -dependence of the deconfining temperature should not be significant. In order to clarify this point, we are trying to investigate the deconfining temperature in the imaginary θ region. It is expected that the deconfining temperature is an analytic even function of θ . We are also trying to take the continuum limit because we found that the results are sensitive to the finite lattice spacing effect.

There are some related works which attempt to investigate the phase structure of 4D

SU(2) gauge theory. For example, the so-called subvolume method is used to calculate the free energy of the theory at $\theta \neq 0$ [12, 13]. The result at high temperature is consistent with the prediction by the instanton gas approximation. On the other hand, the result at zero temperature suggests the spontaneous CP breaking at $\theta = \pi$, which is known to occur at large N . In the analytic study [14], a softly-broken supersymmetric model is used to access 4D SU(N) pure gauge theory at $\theta = \pi$. Assuming the CP broken phase at $\theta = \pi$, the constraint by 't Hooft anomaly matching on the relation between the CP restoration temperature T_{CP} and the deconfining temperature $T_{\text{dec}}(\pi)$ at $\theta = \pi$ is $T_{\text{CP}} \geq T_{\text{dec}}(\pi)$. Interestingly, the results of the work [14] imply that $T_{\text{CP}} = T_{\text{dec}}(\pi)$ for any $N \geq 3$, but $T_{\text{CP}} > T_{\text{dec}}(\pi)$ only for $N = 2$.

The rest of this paper is organized as follows. In Section 2, we briefly review 2D U(1) gauge theory and 4D SU(2) gauge theory with a theta term, and then consider the lattice regularization of them. In Section 3, we show the results of the complex Langevin analysis of 2D U(1) gauge theory. This section is based on the published paper [5]. In Section 4, we apply the CLM to 4D SU(2) gauge theory. The result was also reported in LATTICE2021 conference [9]. In Section 5, we try to investigate the phase structure of 4D SU(2) gauge theory via the imaginary theta term. Since this work is still ongoing, the refined results will be reported in the near future. Section 6 is devoted to a summary and discussions. In appendix A, we review the derivation of the exact partition function of 2D U(1) lattice gauge theory. In appendix B, we show the additional results of the CLM for 2D U(1) gauge theory using a different definition of the topological charge. In appendix C, we show the detailed derivation of the formulae used to apply the stout smearing to the CLM and the HMC. We discuss the effect of the stout smearing in Appendix D.

2 Lattice gauge theory with a theta term

In this section, we review how to define the gauge theories with a theta term on the lattice. We consider 2D U(1) gauge theory and 4D SU(2) gauge theory in the following sub-sections.

2.1 2D U(1) gauge theory on the lattice

First, we review 2D U(1) gauge theory with a theta term on a Euclidean space. The action of the gauge field A_μ ($\mu = 1, 2$) is given by

$$S_g = \frac{1}{4g^2} \int d^2x (F_{\mu\nu})^2, \quad (2.1)$$

where g is the gauge coupling constant and $F_{\mu\nu}$ is the field strength defined as

$$F_{\mu\nu} = \partial_\mu A_\nu - \partial_\nu A_\mu. \quad (2.2)$$

We can add the so-called topological theta term

$$S_\theta = -i\theta Q \quad (2.3)$$

in the action, where Q is the topological charge defined by

$$Q = \frac{1}{4\pi} \int d^2x \epsilon_{\mu\nu} F_{\mu\nu} , \quad (2.4)$$

and θ is a real parameter. The topological charge takes integer values on the compact space. The theta term is gauge invariant and renormalizable. It can be regarded as an imaginary chemical potential of the topological charge.

Next, we put this theory on an $L \times L$ periodic lattice with the lattice spacing a . We define the link variables $U_{n,\mu} \in \text{U}(1)$, where n labels the lattice site as $x_\mu = an_\mu$. We also define the plaquette

$$P_n := U_{n,\hat{1}} U_{n+\hat{1},\hat{2}} U_{n+\hat{2},\hat{1}}^{-1} U_{n,\hat{2}}^{-1} , \quad (2.5)$$

which is a gauge invariant object. Here we use the inverse $U_{n,\mu}^{-1}$ instead of the Hermitian conjugate $U_{n,\mu}^\dagger$ since we have to complexify the dynamical variables respecting holomorphicity in the CLM. The lattice counterpart of the field strength (2.2) can be defined as

$$F_{n,12} := \frac{1}{ia^2} \log P_n , \quad (2.6)$$

where we take the principal value for the complex log; namely $\log z = \log |z| + i \arg z$ with $-\pi < \arg z \leq \pi$. Since the plaquette can then be written in terms of $F_{n,\mu\nu}$ as

$$P_n = e^{ia^2 F_{n,12}} , \quad (2.7)$$

we define the lattice counterpart of the gauge action (2.1) as

$$S_g := -\frac{\beta}{2} \sum_n (P_n + P_n^{-1}) = -\beta \sum_n \cos(a^2 F_{n,12}) , \quad (2.8)$$

which reproduces a natural discretization

$$S_g \simeq \frac{1}{4g^2} \sum_n a^2 (F_{n,\mu\nu})^2 , \quad (2.9)$$

in the continuum limit up to an irrelevant constant with the identification

$$\beta = \frac{1}{(ga)^2} . \quad (2.10)$$

In the present 2D $\text{U}(1)$ lattice gauge theory, the topological charge can be defined as

$$Q_{\log} := \frac{1}{4\pi} \sum_n a^2 \epsilon^{\mu\nu} F_{n,\mu\nu} = -\frac{i}{2\pi} \sum_n \log P_n , \quad (2.11)$$

which gives an integer value even at finite a . This can be proved easily by using $\prod_n P_n = 1$ since each link variable appears twice in this product with opposite directions. We call this definition (2.11) the “log definition”. As an alternative definition, we also consider

$$Q_{\sin} := -\frac{i}{4\pi} \sum_n (P_n - P_n^{-1}) = \frac{1}{2\pi} \sum_n \sin(a^2 F_{n,12}) , \quad (2.12)$$

which approaches (2.4) in the continuum limit recalling (2.7). Note that the topological charge on the lattice defined in this way can take non-integer values in general before taking the continuum limit. We call this definition (2.12) the “sine definition”.

Thus, we define the action of 2D U(1) lattice gauge theory as

$$S = S_g + S_\theta, \quad (2.13)$$

where S_g is given by (2.8) and S_θ is given by (2.3) with Q defined either by (2.11) or by (2.12). Since this theory is superrenormalizable, we can take the continuum limit $a \rightarrow 0$ with fixed g , which is set to unity throughout this paper without loss of generality. In this unit, the physical volume of the 2D torus is given by

$$V_{\text{phys}} = (La)^2 = \frac{L^2}{\beta}. \quad (2.14)$$

Note also that this theory has the 2π periodicity of the parameter $\theta \in \mathbb{R}$ since the partition function

$$Z = \int \mathcal{D}A e^{-S_g + i\theta Q} \quad (2.15)$$

is invariant under the shift $\theta \rightarrow \theta + 2\pi$.

2.2 4D SU(2) gauge theory on the lattice

In this sub-section, we review 4D SU(2) gauge theory with a theta term on a Euclidean space. The action for the gauge field A_μ^a ($a = 1, 2, 3$) ($\mu = 1, \dots, 4$) is given by

$$S_g = \frac{1}{4g^2} \int d^4x F_{\mu\nu}^a F_{\mu\nu}^a, \quad (2.16)$$

where $F_{\mu\nu}^a$ is the field strength

$$F_{\mu\nu}^a = \partial_\mu A_\nu^a - \partial_\nu A_\mu^a - \epsilon^{abc} A_\mu^b A_\nu^c. \quad (2.17)$$

Here we define the basis of SU(2) generators as

$$\tau^a := \frac{\sigma^a}{2}, \quad (2.18)$$

where σ^a ($a = 1, 2, 3$) are Pauli matrices. The generators satisfy the following relations.

$$\text{Tr} [\tau^a \tau^b] = \frac{1}{2} \delta^{ab} \quad (2.19)$$

$$[\tau^a, \tau^b] = i\epsilon^{abc} \tau^c \quad (2.20)$$

$$\tau_{ij}^a \tau_{kl}^a = \frac{1}{2} \left(\delta_{il} \delta_{jk} - \frac{1}{2} \delta_{ij} \delta_{kl} \right) \quad (2.21)$$

For the 4D gauge theory, the topological charge Q is defined by

$$Q = \frac{1}{64\pi^2} \int d^4x \epsilon_{\mu\nu\rho\sigma} F_{\mu\nu}^a F_{\rho\sigma}^a, \quad (2.22)$$

which takes integer values on the compact space. We define the theta term $S_\theta = -i\theta Q$ with the real parameter θ , and the action is given by $S = S_g + S_\theta$.

Next, we consider the lattice discretization of the theory. We introduce link variables $U_{n,\mu} \in \text{SU}(2)$ and define the plaquette

$$P_n^{\mu\nu} := U_{n,\mu} U_{n+\hat{\mu},\nu} U_{n+\hat{\nu},\mu}^{-1} U_{n,\nu}^{-1}, \quad (2.23)$$

where the index n labels the lattice site and $\hat{\mu}$ represents the unit vector along the μ -th direction. Note that we use $U_{n,\mu}^{-1}$ instead of $U_{n,\mu}^\dagger$ to respect holomorphicity, which is necessary to justify the CLM. We define the plaquette action by

$$S_g = -\frac{\beta}{4} \sum_n \sum_{\mu \neq \nu} \text{Tr} P_n^{\mu\nu} \quad (2.24)$$

with the lattice coupling constant β . For the topological charge on the lattice, we apply the simplest discretization [10] given by the so called "clover leaf" formula.

$$Q_{\text{cl}} = -\frac{1}{32\pi^2} \sum_n \frac{1}{2^4} \sum_{\mu,\nu,\rho,\sigma=\pm 1}^{\pm 4} \tilde{\epsilon}_{\mu\nu\rho\sigma} \text{Tr} [P_n^{\mu\nu} P_n^{\rho\sigma}] \quad (2.25)$$

Here the orientation of the plaquette is generalized to negative directions. Correspondingly, the anti-symmetric tensor $\tilde{\epsilon}_{\mu\nu\rho\sigma}$ also has negative indices, for example

$$1 = \tilde{\epsilon}_{1234} = -\tilde{\epsilon}_{2134} = -\tilde{\epsilon}_{(-1)234} = \dots \quad (2.26)$$

The definition (2.25) in 4D can be regarded as an analogy of (2.12) in 2D.

Usually the topological charge Q_{cl} does not take integer values on the finite lattice due to the discretization effect. We can recover the topological property of the gauge field by eliminating short-range fluctuations. Some smoothing techniques, such as the gradient flow, stout smearing and so on, make the topological charge close to integers. In the analysis of 4D $\text{SU}(2)$ gauge theory, we apply the stout smearing to the CLM, which is discussed in section 4.4.

3 Complex Langevin analysis of 2D $\text{U}(1)$ gauge theory

Since the theta term is purely imaginary, the Monte Carlo simulation of the gauge theory with the theta term is extremely difficult due to the sign problem. We try to overcome this problem by using the complex Langevin method (CLM) [2, 3, 15, 16, 17, 4]. We show the results of the complex Langevin simulation of 2D $\text{U}(1)$ gauge theory with a theta term, which suggest that a naive implementation of the method fails. The CLM fails due to topological nature of the theory. We avoid the problem by introducing a puncture on the lattice. Although the 2π periodicity of θ is lost, the CLM reproduces the exact result. This section is based on the published paper [5].

3.1 Application of the CLM to 2D U(1) gauge theory

First, we review how to apply the CLM to 2D U(1) gauge theory. The dynamical variables are complexified in the CLM. In the present case of U(1) gauge theory, we extend the link variables $U_{n,\mu} \in \text{U}(1)$ to $U_{n,\mu} \in \mathbb{C} \setminus \{0\}$, which corresponds to extending the gauge field $A_\mu \in \mathbb{R}$ to $A_\mu \in \mathbb{C}$ in the continuum theory. Then we consider a fictitious time evolution of the link variables $U_{n,\mu}(t)$ governed by the complex Langevin equation

$$U_{n,\mu}(t + \Delta t) = U_{n,\mu}(t) \exp \left[-i\Delta t D_{n,\mu} S + i\sqrt{\Delta t} \eta_{n,\mu}(t) \right], \quad (3.1)$$

where $\eta_{n,\mu}(t)$ is a real Gaussian noise normalized by $\langle \eta_{n,\mu}(t) \eta_{k,\nu}(t) \rangle = 2\delta_{nk} \delta_{\mu\nu} \delta_{t,t'}$. The drift term $D_{n,\mu} S$ is first calculated by the differential operation with respect to the unitary link variable (Lie group element)

$$D_{n,\mu} S = \left. \frac{d}{d\epsilon} S(e^{i\epsilon} U_{n,\mu}) \right|_{\epsilon \rightarrow 0}, \quad (3.2)$$

and then it is defined for the complexified link variables by analytic continuation in order to respect holomorphicity. The drift term $D_{n,\mu} S_g$ from the gauge action (2.8) can be calculated straightforwardly.

$$\begin{aligned} D_{n,1} S_g &= -i\frac{\beta}{2} \left(P_n - P_n^{-1} - P_{n-\hat{2}} + P_{n-\hat{2}}^{-1} \right) \\ D_{n,2} S_g &= i\frac{\beta}{2} \left(P_n - P_n^{-1} - P_{n-\hat{1}} + P_{n-\hat{1}}^{-1} \right) \end{aligned} \quad (3.3)$$

The drift term $D_{n,\mu} S_\theta$ from the theta term depends on the definition of the topological charge. If one uses the log definition (2.11), the drift term is identically zero except for $P_n = -1$, where it becomes singular due to the branch cut of the complex log. This behavior comes from the topological nature of the log definition. In fact, one of the plaquettes has to be $P_n = -1$ when the topological charge (2.11) changes discontinuously. It is not straightforward to define the drift term as a holomorphic function of $U_{n,\mu}$ in this case.

On the other hand, if one uses the sine definition (2.12), the drift term can be calculated straightforwardly.

$$\begin{aligned} D_{n,1} S_\theta &= -i\frac{\theta}{4\pi} \left(P_n + P_n^{-1} - P_{n-\hat{2}} - P_{n-\hat{2}}^{-1} \right) \\ D_{n,2} S_\theta &= i\frac{\theta}{4\pi} \left(P_n + P_n^{-1} - P_{n-\hat{1}} - P_{n-\hat{1}}^{-1} \right) \end{aligned} \quad (3.4)$$

It may be viewed as an approximation of the δ -function like behavior mentioned above. Moreover, it can be readily extended to a holomorphic function of $U_{n,\mu}$. For this reason, we use the sine definition in this setup.

The criterion [4] for the validity of the CLM states that the probability distribution of the drift term should fall off exponentially or faster. There are two cases in which

this criterion cannot be met. The first case occurs when the configuration comes close to the poles of the drift terms (3.3), (3.4), which correspond to configurations with $P_n = 0$ for some n . If such configurations appears frequently during the Langevin process, the criterion tends to be violated. This problem is called the singular-drift problem [18, 19], which was found first in simple models [20, 21]. The second case occurs when the dynamical variables make large excursions in the imaginary directions [15]. This problem is called the excursion problem. In the present model, this corresponds to the situation in which the link variables have absolute values $|U_{n,\mu}|$ far from unity.

These problems can occur since the link variables $U_{n,\mu}$ are not restricted to be unitary in the CLM. In order to avoid them, it is important to perform the gauge cooling. The idea of gauge cooling [22] is to reduce the non-unitarity of link variables as much as possible by gauge transformations corresponding to the complexified Lie group after each step of the Langevin process. This procedure can be added without affecting the argument for justifying the CLM as demonstrated explicitly in [17, 4]. Recently, the mechanism of the gauge cooling for stabilizing the complex Langevin simulation has been investigated [23].

The deviation of the link variables from $U(1)$ can be measured by the unitarity norm

$$\mathcal{N} := \frac{1}{2L^2} \sum_{n,\mu} \left\{ U_{n,\mu}^* U_{n,\mu} + (U_{n,\mu}^* U_{n,\mu})^{-1} - 2 \right\}. \quad (3.5)$$

The gauge cooling reduces this quantity by a complexified gauge transformation, namely $\mathbb{C} \setminus \{0\}$ transformation in the present case, which is determined as follows.

First we consider an infinitesimal gauge transformation

$$\delta U_{n,\mu} = (\epsilon_n - \epsilon_{n+\hat{\mu}}) U_{n,\mu}, \quad (3.6)$$

with small parameters $\epsilon_n \in \mathbb{R}$. The change of the unitarity norm due to the transformation is given by

$$\begin{aligned} \delta \mathcal{N} &= \frac{1}{2L^2} \sum_{n,\mu} \left\{ 2(\epsilon_n - \epsilon_{n+\hat{\mu}}) U_{n,\mu}^* U_{n,\mu} - 2(\epsilon_n - \epsilon_{n+\hat{\mu}}) (U_{n,\mu}^* U_{n,\mu})^{-1} \right\} \\ &= \frac{1}{2L^2} \sum_n 2\epsilon_n G_n, \end{aligned} \quad (3.7)$$

where we define the gradient G_n as

$$G_n := \sum_{\mu} \left\{ U_{n,\mu}^* U_{n,\mu} - U_{n-\hat{\mu},\mu}^* U_{n-\hat{\mu},\mu} - (U_{n,\mu}^* U_{n,\mu})^{-1} + (U_{n-\hat{\mu},\mu}^* U_{n-\hat{\mu},\mu})^{-1} \right\}. \quad (3.8)$$

Therefore, we find that the unitarity norm is reduced efficiently by choosing $\epsilon_n \propto -G_n$.

Based on this result, we consider a finite gauge transformation

$$U_{n,\mu} \mapsto g_n U_{n,\mu} g_{n+\hat{\mu}}^{-1}; \quad g_n = e^{-\alpha G_n} \quad (3.9)$$

with a parameter $\alpha > 0$. Applying this transformation, the unitarity norm turns out to be

$$\mathcal{N}(\alpha) = \frac{1}{2L^2} \sum_{n,\mu} \left\{ U_{n,\mu}^* U_{n,\mu} e^{-2\alpha(G_n - G_{n+\hat{\mu}})} + (U_{n,\mu}^* U_{n,\mu})^{-1} e^{2\alpha(G_n - G_{n+\hat{\mu}})} - 2 \right\}, \quad (3.10)$$

depending on α in (3.9). We search for an optimal α that minimizes (3.10) and then satisfies

$$\frac{d\mathcal{N}(\alpha)}{d\alpha} = 0. \quad (3.11)$$

Note here that α should be a small number since the gauge cooling is performed after each step of the Langevin process. We therefore expand (3.11) with respect to α up to the first order and obtain the solution

$$\alpha = \frac{1}{2} \frac{\sum_n G_n^2}{\sum_{n,\mu} (G_n - G_{n+\hat{\mu}})^2 [U_{n,\mu}^* U_{n,\mu} + (U_{n,\mu}^* U_{n,\mu})^{-1}]}. \quad (3.12)$$

We use this value of α as an estimation of the optimal value that minimizes (3.10). We repeat this transformation several times until the unitarity norm changes by a fraction less than 10^{-5} .

When we solve the discretized complex Langevin equation (3.1), the drift term can be extremely large, in particular during the thermalization process. This causes a large discretization error, which either makes the thermalization slow or destabilizes the simulation. We can avoid this problem by using a smaller step size Δt , but the computational cost for a fixed Langevin time increases proportionally to $(\Delta t)^{-1}$. The adaptive step size [24] is a useful technique, which amounts to reducing the step size only when the drift term becomes large.

In our simulation, we measure the magnitude of the drift term defined as

$$u = \max_{n,\mu} |D_{n,\mu} S| \quad (3.13)$$

at each step, and choose the Langevin step size Δt in (3.1) as

$$\Delta t = \begin{cases} \Delta t_0 & \text{for } u < v_0, \\ \frac{v_0}{u} \Delta t_0 & \text{otherwise,} \end{cases} \quad (3.14)$$

where Δt_0 is the default step size, and v_0 is the threshold for the magnitude of drift term. In the present work, the default step size is set to $\Delta t_0 = 10^{-5}$, and the threshold is set to $v_0 = 2\beta$, corresponding to a bound $u \leq 2\beta$ for $\theta = 0$.

3.2 Result of the CLM on the periodic lattice

In this section, we show our results obtained by the CLM implemented on the periodic lattice. We adopt the sine definition (2.12) of the topological charge since it gives the holomorphic drift term (3.4). We have performed simulations at various θ for $(\beta, L) = (3, 10), (12, 20)$ corresponding to a fixed physical volume $V_{\text{phys}} := L^2/\beta = 10^2/3$ with different lattice spacings. First, we discuss the validity of the CLM at $\theta = \pi$ for example, where the sign problem is most severe, but the situation is the same for any value of $\theta \neq 0$.

In Fig. 3.1(Left), we show the histogram of the magnitude u of the drift term defined by (3.13). The distribution falls off rapidly for the fine lattice $(\beta, L) = (12, 20)$, but it

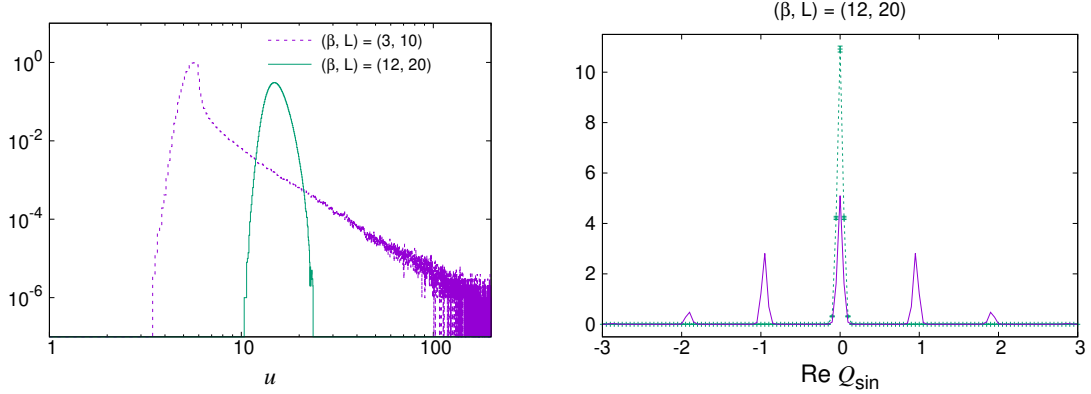


Figure 3.1: The results obtained by the CLM on the periodic lattice using the sine definition Q_{\sin} of the topological charge. (Left) The histogram of the magnitude u of the drift term defined by (3.13) is shown for $(\beta, L) = (3, 10)$, $(12, 20)$ with $\theta = \pi$. (Right) The histogram of $\text{Re } Q_{\sin}$ is plotted for $(\beta, L) = (12, 20)$ with $\theta = \pi$. The exact result obtained for $(\beta, L) = (12, 20)$ with $\theta = 0$ is also shown by the solid line for comparison.

decays slowly with a power law for the coarse lattice $(\beta, L) = (3, 10)$. Thus the criterion for correct convergence is satisfied for $(\beta, L) = (12, 20)$ but not for $(\beta, L) = (3, 10)$ due to the large drifts.

In Fig. 3.1(Right), we plot the histogram of $\text{Re } Q_{\sin}$ obtained by the CLM for the fine lattice $(\beta, L) = (12, 20)$ with $\theta = \pi$, which has a sharp peak at $\text{Re } Q_{\sin} = 0$. In the same figure, we also plot the exact result for $(\beta, L) = (12, 20)$ at $\theta = 0$ for comparison, which exhibits some sharp peaks near integer values. This result indicates that the transitions between different topological sectors are highly suppressed in the simulation on the fine lattice, which causes a problem with the ergodicity. This problem occurs also at $\theta = 0$ for large β , and it is called the “topology freezing problem”. In fact, the results obtained by simulations suffering from this problem correspond to the expectation values restricted to the single topological sector specified by the initial configuration.

For the coarse lattice $(\beta, L) = (3, 10)$ with $\theta = \pi$, on the other hand, the histogram of $\text{Re } Q_{\sin}$ obtained by the CLM has broad peaks that overlap with each other, which looks similar to the exact result with $\theta = 0$. This implies that the topology freezing problem is absent for $(\beta, L) = (3, 10)$. See also Fig. 3.3.

Below we define some observables investigated in our simulation. First, we define the average plaquette by

$$w = \frac{1}{V} \frac{\partial}{\partial \beta} \log Z. \quad (3.15)$$

Hereafter, V denotes the number of plaquettes in the action, which is $V = L^2$ for the periodic lattice. The topological charge density is defined by

$$\frac{1}{V} \langle Q \rangle = -i \frac{1}{V} \frac{\partial}{\partial \theta} \log Z, \quad (3.16)$$

which is zero at $\theta = 0$ and purely imaginary for $\theta \neq 0$. Finally, the topological suscepti-

bility is defined by

$$\chi = \frac{1}{V} (\langle Q^2 \rangle - \langle Q \rangle^2) = -\frac{1}{V} \frac{\partial^2}{\partial \theta^2} \log Z, \quad (3.17)$$

which is real for any θ . Note that the topological susceptibility χ is related to the topological charge density (3.16) through

$$\chi = -i \frac{1}{V} \frac{\partial}{\partial \theta} \langle Q \rangle. \quad (3.18)$$

This relation is general and independent of the definition of Q . Thus, it should be satisfied as long as the CLM works correctly.

In Fig. 3.2, we show the observables obtained by the CLM on the periodic lattice. We also plot the exact results for comparison, which are derived in Appendix A.4. In the left column, we present our results for the coarse lattice $(\beta, L) = (3, 10)$, which suffer from the wrong convergence. In the right column, we present our results for the fine lattice $(\beta, L) = (12, 20)$, which suffer from the topology freezing problem. In either case, our results do not reproduce the exact results as anticipated. Note that our results at $\theta = 0$ agree with the exact results for $(\beta, L) = (3, 10)$ but not for $(\beta, L) = (12, 20)$. This is because the topology freezing problem occurs for large β even at $\theta = 0$.

Thus we find that the CLM with the naive implementation fails for both the fine lattice and the coarse lattice for different reasons. For the coarse lattice, the topology change occurs but the criterion for correct convergence is not satisfied due to the large drifts. For the fine lattice, the criterion for correct convergence is satisfied, but the ergodicity is violated due to the topology freezing problem. We could not find a parameter region in which neither of the problems occurs. In fact, we will see in the next section that these problems are related to each other at least in the present model.

3.3 Appearance of large drifts and topology change

In this section, we provide detailed discussions on the relationship between the appearance of large drifts and the topology change on the periodic lattice. First, we define the notion of topological sector by $\text{Re } Q_{\log}$ evaluated by (2.11) for each configuration. It can be used in the CLM since $\text{Re } Q_{\log}$ takes integer values even for complexified configurations.

During the simulation, a transition between different topological sectors occurs when one of the plaquettes crosses the branch cut. In other words, $\text{Re } Q_{\log}$ increases by one if the phase of the plaquette jumps from $-\pi$ to π , and vice versa. We found that large drift terms can appear when this transition occurs. We can see the relation in Fig. 3.3, where we plot the histories of $\text{Re } Q_{\log}$ and the magnitude u of the drift term (3.13) in the same Langevin time. There is clear correlation between the large drift term and the topology change. We also confirmed that the large drift term appears for the link variables composing the plaquette that crosses the branch cut.

In order to understand this observation further, we focus on the Langevin time evolution of a particular link variable $U_{K,1}$. The drift term for this link depends on the plaquettes P_K and $P_{K-\hat{2}}$ sharing the link. For simplicity, we set $P_{K-\hat{2}} = 1$ and consider

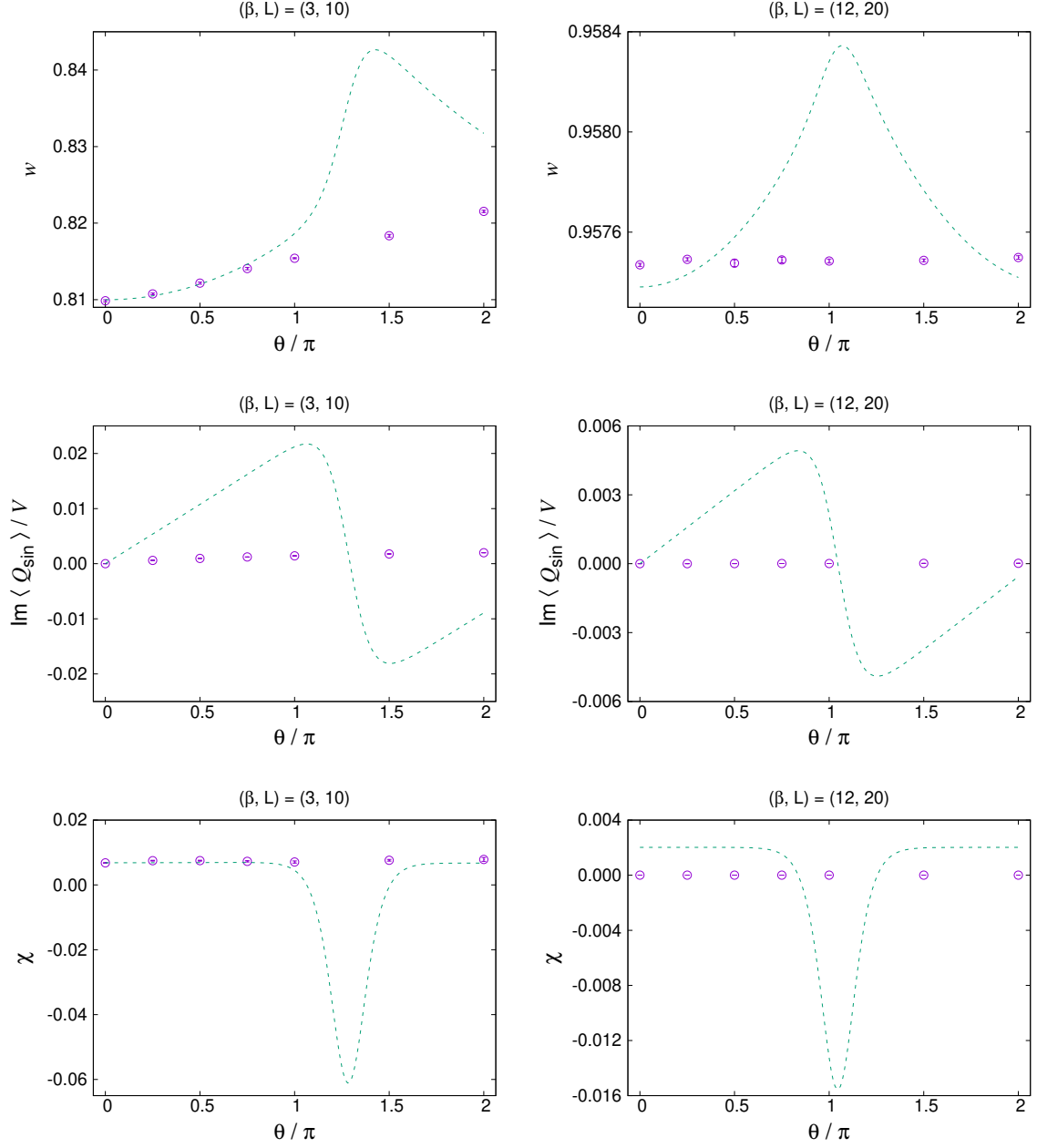


Figure 3.2: The results of various observables obtained by the CLM on the periodic lattice with the sine definition Q_{sin} . The average plaquette (Top), the imaginary part of the topological charge density (Middle), the topological susceptibility (Bottom) are plotted against θ/π for $(\beta, L) = (3, 10)$ (Left) and $(12, 20)$ (Right). The exact results are also shown by the dashed lines for comparison.

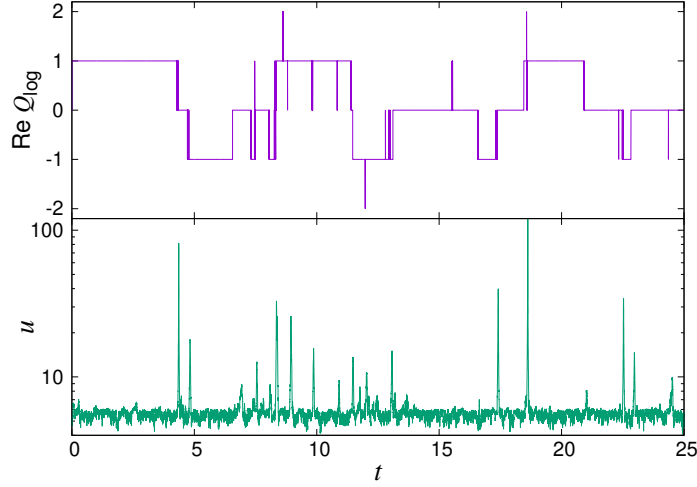


Figure 3.3: The results obtained by the CLM on the periodic lattice with the sine definition Q_{sin} for $(\beta, L) = (3, 10)$ with $\theta = \pi$. The upper plot shows the history of the topological charge Q_{log} with the log definition, whereas the lower plot shows the history of the magnitude u of the drift term in the log scale.

the drift term v as a function of P_K

$$v = \beta \sin \phi - i \frac{\theta}{2\pi} (\cos \phi - 1) , \quad (3.19)$$

where we have defined a complex phase of P_K by $\phi := -i \log P_K$. In Fig. 3.4(Left), we plot the drift term as a flow diagram for $\beta = \theta = 1$. Since the contribution of the drift term v to the change of ϕ in the Langevin step is given by $\Delta\phi = -v\Delta t$, we actually plot $(-v)$ in the complex ϕ plane.

In what follows we assume that $\beta > \theta/2\pi$. Then we find from Eq. (3.19) that there are two fixed points corresponding to $v = 0$. One is $\phi = 0$ and the other is $\phi = i \log[(\theta/2\pi + \beta)/(\theta/2\pi - \beta)]$, which is close to $\pm\pi$. As we can see from Fig. 3.4(Left), the fixed point $\phi = 0$ is attractive, which confirms that P_K tends to become unity when β is large. The other fixed point $\phi \sim \pm\pi$ is repulsive, and the magnitude $|v|$ grows exponentially as one flows away in the imaginary direction. In Fig. 3.4(Right), we plot the magnitude $|v|$ as a function of $\text{Im} \phi$ for $\text{Re} \phi = \pm\pi$. As we mentioned above, when the transition between topological sectors occurs, one of the plaquettes crosses the branch cut $\text{Re} \phi = \pm\pi$. When this happens, the configuration can easily flow in the imaginary direction, which causes a large drift.

3.4 Introducing a puncture on the torus

Since the problem we found for the periodic lattice originates from the topological nature of the theory, a simple remedy would be to change the topology of the base manifold to a non-compact one. Here we consider introducing a puncture on the 2D torus. Once we introduce a puncture, the drift term $D_{n,\mu} S_\theta$ with the log definition of the topological

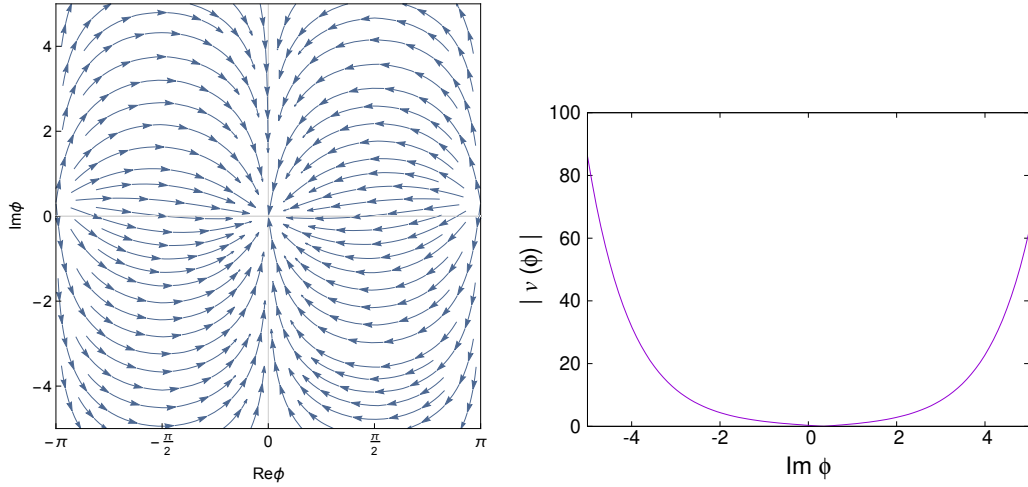


Figure 3.4: (Left) A flow diagram representing $-v$ defined by (3.19) is shown as a function of ϕ for $\beta = \theta = 1$. (Right) The absolute value $|v(\phi)|$ is plotted against $\text{Im } \phi$ for $\text{Re } \phi = \pi$.

charge has nonzero contributions for the link variables surrounding the puncture. Thus, we can include the effect of the theta term correctly in the CLM up to the singular behavior on the branch cut. We will discuss its validity in Section 3.6. For the rest of this paper, we basically use the log definition to simplify our discussions. The topological charge on the punctured torus is no longer restricted to integer values, and it can change freely unlike the periodic case. Nevertheless, we found that the effect of the puncture disappears in the infinite volume limit for $|\theta| < \pi$ as we demonstrate explicitly in this section using the exact results.

There are various ways to introduce a puncture on the periodic lattice. Here we consider removing a plaquette simply. More precisely, we define the punctured model by removing one plaquette P_K at the site $n = K$ from the gauge action (2.8) and the topological charge (2.11). There are many other way to put a puncture, and it is also possible to use just the open boundary condition. But in any case, one can obtain exact results for a finite lattice as explained in Appendix A. In fact, the model with the puncture (the open boundary) is equivalent to the non-punctured (periodic) model in the infinite volume limit for $|\theta| < \pi$.

We show the equivalence of the punctured model and the non-punctured model in the infinite volume limit. Here we use the log definition of the topological charge, but a similar statement holds also for the sine definition.¹ The partition function for the non-punctured model is given by

$$Z_{\text{nonpunc}} = \sum_{n=-\infty}^{+\infty} [\mathcal{I}(n, \theta, \beta)]^V \quad (3.20)$$

¹In the case of the sine definition, the equivalence of the two models in the infinite volume limit holds for $|\theta| < \theta_c(\beta)$, where $\theta_c(\beta) \sim \pi\{1 + 1/(2\beta)\}$ for large β .

for the non-punctured lattice with the volume $V = L^2$ as derived in Appendix A.2, where the function $\mathcal{I}(n, \theta, \beta)$ is defined by

$$\mathcal{I}(n, \theta, \beta) = \frac{1}{2\pi} \int_{-\pi}^{\pi} d\phi \exp \left[\beta \cos \phi + i \left(\frac{\theta}{2\pi} - n \right) \phi \right]. \quad (3.21)$$

In the infinite volume limit $V \rightarrow \infty$, the sum over n in (3.20) is dominated by the term which gives the largest absolute value $|\mathcal{I}(n, \theta, \beta)|$. This term corresponds to the n that minimizes $|\frac{\theta}{2\pi} - n|$. Thus the free energy in the infinite volume limit is obtained as

$$\lim_{V \rightarrow \infty} \frac{1}{V} \log Z_{\text{nonpunc}} = \log \mathcal{I}(0, \tilde{\theta}, \beta) \quad (3.22)$$

where $\tilde{\theta}$ is defined by $\tilde{\theta} := \theta - 2\pi k$ with the integer k chosen so that $-\pi < \tilde{\theta} \leq \pi$.

On the other hand, the partition function for the punctured model is given by

$$Z_{\text{punc}} = [\mathcal{I}(0, \theta, \beta)]^V \quad (3.23)$$

on the punctured lattice with the volume $V = L^2 - 1$ as shown in Appendix A.3, which implies that the free energy

$$\frac{1}{V} \log Z_{\text{punc}} = \log \mathcal{I}(0, \theta, \beta) \quad (3.24)$$

is actually independent of V . Hence all the observables derived from it has no finite size effects. Note also that this model no longer has the 2π periodicity of θ . By comparing (3.22) and (3.24), one can see that the two models are equivalent in the infinite volume limit as long as $|\theta| < \pi$.

The observables defined in Section 3.2 can be calculated from the partition functions (3.20) and (3.23) for the two models by numerical integration. The details of derivation is explained in Appendix A.4. In Fig. 3.5, we plot the average plaquette (3.15), the imaginary part of the topological charge density (3.16) and the topological susceptibility (3.17) for two different volumes $L = 10, 20$ with the same $\beta = 12$. The results for the punctured model is equivalent to the results for the infinite volume limit of the non-punctured model within the range $|\theta| < \pi$.

We can obtain the free energy (3.24) for the punctured model in the continuum limit explicitly. The integrating over ϕ in Eq. (3.21) is evaluated for $\beta \gg 1$ as

$$\mathcal{I}(n, \theta, \beta) \simeq \frac{1}{\sqrt{2\pi\beta}} e^{\beta - \frac{1}{2\beta} \left(\frac{\theta}{2\pi} - n \right)^2}, \quad (3.25)$$

then we get

$$\frac{1}{V} \log Z_{\text{punc}} \simeq e^\beta - \frac{1}{2} \log 2\pi\beta - \frac{\theta^2}{8\pi^2\beta}. \quad (3.26)$$

From this result, we obtain various observables for the continuum limit of the punctured model as

$$w \simeq 1 - \frac{1}{2\beta} + \frac{\theta^2}{8\pi^2\beta^2}, \quad (3.27)$$

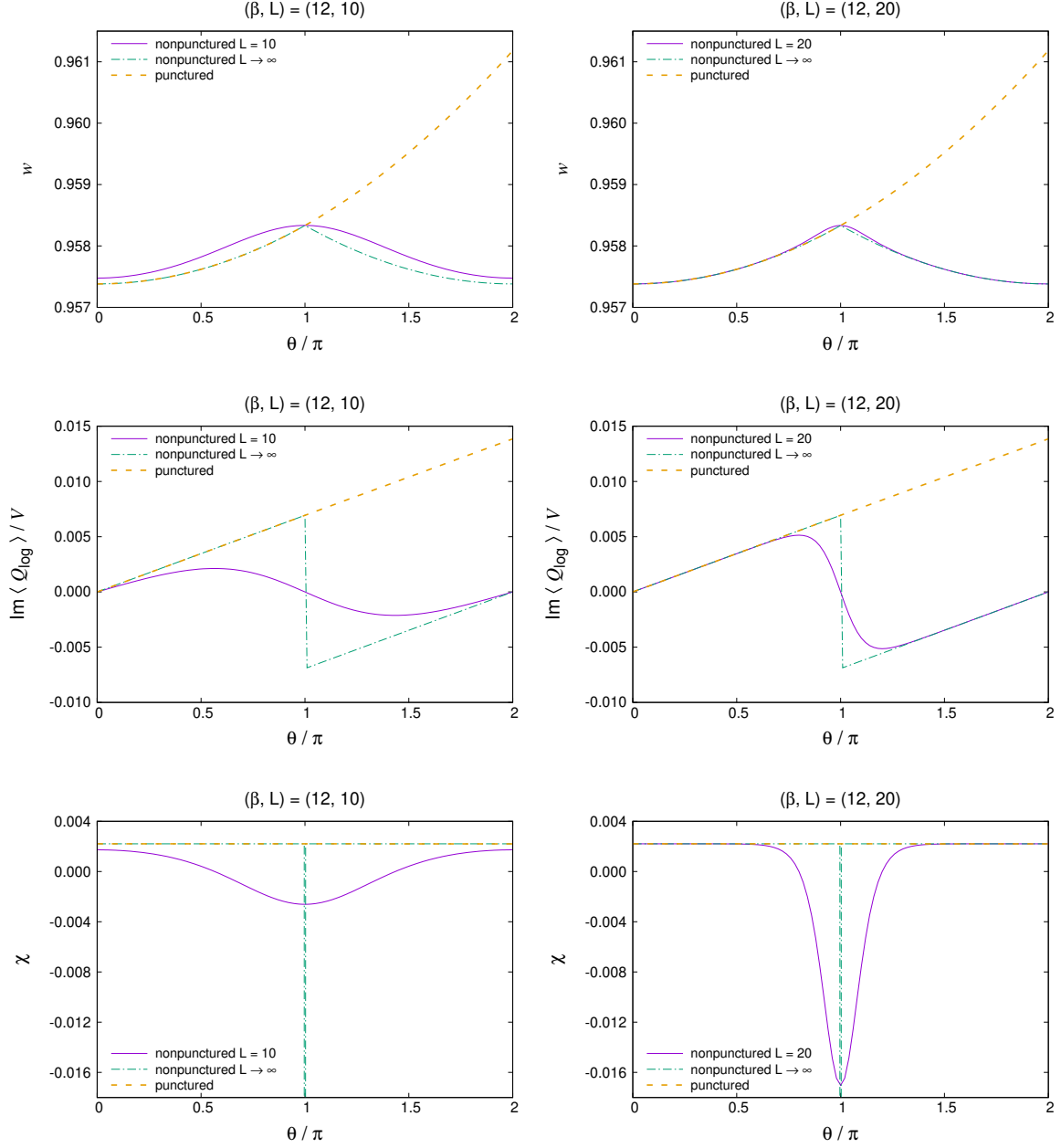


Figure 3.5: The exact results for various observables obtained for the log definition Q_{\log} of the topological charge. The average plaquette (Top), the imaginary part of the topological charge density (Middle), the topological susceptibility (Bottom) obtained for the non-punctured (solid line) and punctured (dashed line) models are plotted against θ for $L = 10$ (Left) and $L = 20$ (Right) with the same $\beta = 12$. Note that the results for the punctured model are actually independent of L . For the non-punctured model, we also plot the results in the infinite volume limit $L \rightarrow \infty$ with $\beta = 12$ by the dash-dotted lines for comparison.

$$\frac{\langle Q \rangle}{V} \simeq \frac{i\theta}{4\pi^2\beta}, \quad (3.28)$$

$$\chi \simeq 1 - \frac{1}{2\beta} + \frac{\theta^2}{8\pi^2\beta^2}, \quad (3.29)$$

which explains the θ dependence observed in Fig. 3.5.

3.5 Application of the CLM to the punctured model

In this section, we discuss the application of the CLM to the punctured model using the log definition Q_{\log} of the topological charge. Our results reproduce the exact results as long as the system is close enough to the continuum limit. We also show that the topology freezing problem is avoided without causing large drifts thanks to the puncture.

3.5.1 Drift terms for the punctured model

We have discussed the drift terms in the non-punctured model in Section 3.1. For the punctured model, the drift terms for the four link variables surrounding the puncture, namely $U_{K,1}$, $U_{K+\hat{2},1}$, $U_{K,2}$ and $U_{K+\hat{1},2}$, are modified.

$$D_{n,1}S = \begin{cases} -i\frac{\beta}{2}(P_n - P_n^{-1} - P_{n-\hat{2}} + P_{n-\hat{2}}^{-1}) & \text{for } n \neq K, K + \hat{2} \\ -i\frac{\beta}{2}(-P_{K-\hat{2}} + P_{K-\hat{2}}^{-1}) + i\frac{\theta}{2\pi} & \text{for } n = K \\ -i\frac{\beta}{2}(P_{K+\hat{2}} - P_{K+\hat{2}}^{-1}) - i\frac{\theta}{2\pi} & \text{for } n = K + \hat{2} \end{cases} \quad (3.30)$$

$$D_{n,2}S = \begin{cases} -i\frac{\beta}{2}(-P_n + P_n^{-1} + P_{n-\hat{1}} - P_{n-\hat{1}}^{-1}) & \text{for } n \neq K, K + \hat{1} \\ -i\frac{\beta}{2}(P_{K-\hat{1}} - P_{K-\hat{1}}^{-1}) - i\frac{\theta}{2\pi} & \text{for } n = K \\ -i\frac{\beta}{2}(-P_{K+\hat{1}} + P_{K+\hat{1}}^{-1}) + i\frac{\theta}{2\pi} & \text{for } n = K + \hat{1} \end{cases} \quad (3.31)$$

Here we have ignored the issue of the branch cut of the log definition discussed in Section 3.1. This is justified if all the plaquettes in the action never cross the branch cut. In other words, the plaquettes should satisfy $|\text{Im} \log P_n| < \pi$ for $\forall n \neq K$ during the Langevin simulation. We will see that this assumption is justified for sufficiently large β in Section 3.6.

Note that the drift term from the theta term appears only for the link variables surrounding the puncture. and it is actually a constant independent of the configuration. While these properties are peculiar to the log definition Q_{\log} , similar ones hold also for the sine definition Q_{\sin} for large β . We discuss the case with the sine definition in Appendix B, where we obtain qualitatively the same results as those with the log definition.

3.5.2 Distribution of the topological charge

As we have seen in Section 3.4, the punctured model is equivalent to the infinite volume limit of the non-punctured model for $|\theta| < \pi$. However, the punctured model does not have the 2π periodicity of θ , which exists in the original non-punctured model. In order to understand this point further, we discuss the θ dependence of the partition function in

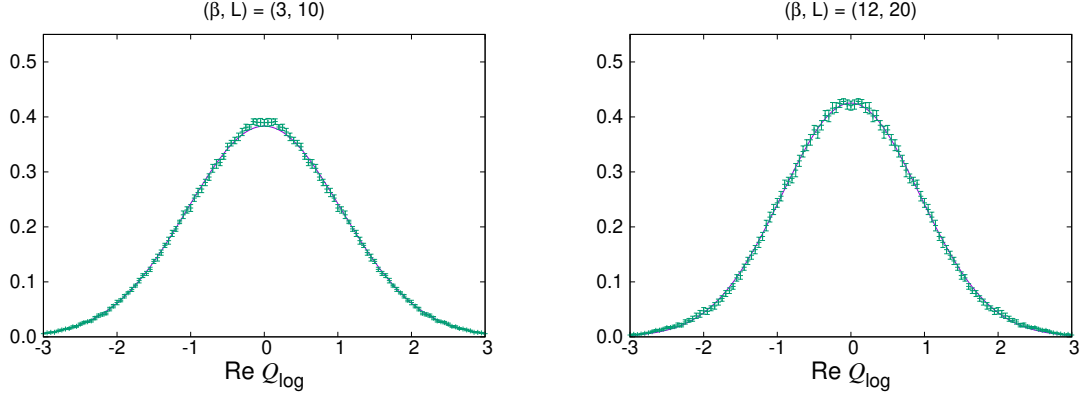


Figure 3.6: The topological charge distribution for $\theta = 0$ obtained by the Langevin simulation for the punctured model using the log definition Q_{\log} is plotted for $(\beta, L) = (3, 10)$ (Left) and $(\beta, L) = (12, 20)$ (Right). The solid lines represent the exact results obtained by evaluating ((3.33)) using the partition function (3.23).

this section. Let us first note that the partition function for arbitrary θ is related to the topological charge distribution $\rho(q)$ for $\theta = 0$ through Fourier transformation.

$$\begin{aligned}
Z(\theta) &= \int dU e^{-S_g[U] + i\theta Q[U]} \\
&= \int dU e^{-S_g[U]} \int dq e^{i\theta q} \delta(Q[U] - q) \\
&= Z(0) \int dq e^{i\theta q} \rho(q)
\end{aligned} \tag{3.32}$$

Therefore, the absence of the 2π periodicity in θ in the punctured model is directly related to its property that the topological charge can take non-integer values even if we use the log definition Q_{\log} . By making an inverse Fourier transform, we can obtain the topological charge distribution $\rho(q)$ for $\theta = 0$ from the θ -dependent partition function.

$$\rho(q) = \frac{1}{Z(0)} \int_{-\infty}^{\infty} \frac{d\theta}{2\pi} Z(\theta) e^{-i\theta q}. \tag{3.33}$$

We can calculate this quantity for the punctured model by the Langevin simulation for $\theta = 0$. While the sign problem is absent for $\theta = 0$, the topology freezing can still be a problem for large β . In Fig. 3.6, we show the results for $(\beta, L) = (3, 10)$ and $(\beta, L) = (12, 20)$, which agree well with the exact results obtained by evaluating (3.33) using the partition function (3.23). The agreement of these results confirms that the topology freezing problem is absent in the punctured model at least for $\theta = 0$.

3.6 Validity of the CLM for the punctured model

In this section, we discuss the validity of the CLM for the punctured model. Fig. 3.7(Left) shows the histogram of the drift term for $(\beta, L) = (3, 10)$, $(12, 20)$ with $\theta = \pi$, which are

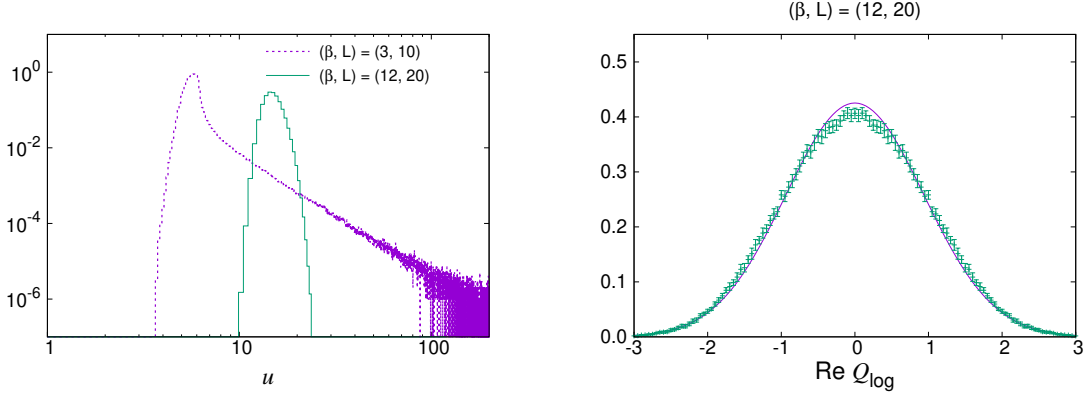


Figure 3.7: The results obtained by the CLM for the punctured model using the log definition Q_{\log} of the topological charge. (Left) The histogram of the magnitude u of the drift term defined by (3.13) is shown for $(\beta, L) = (3, 10)$ and $(12, 20)$ with $\theta = \pi$. (Right) The histogram of $\text{Re } Q_{\log}$ is shown for $(\beta, L) = (12, 20)$ with $\theta = \pi$. The exact result obtained for $(\beta, L) = (12, 20)$ with $\theta = 0$ is shown by the solid line for comparison.

the same parameters used in Section 3.2 for the non-punctured model. We find that the criterion for the correct convergence is satisfied for the fine lattice $(\beta, L) = (12, 20)$ but not for the coarse lattice $(\beta, L) = (3, 10)$, similarly to the case of the non-punctured model. On the other hand, the behavior of the topological charge is different from the non-punctured model. In Fig. 3.7(Right), we show the histogram of $\text{Re } Q_{\log}$ obtained by the CLM for $(\beta, L) = (12, 20)$ with $\theta = \pi$. It is widely distributed in contrast to the plot in Fig. 3.1(Right) for the same $(\beta, L) = (12, 20)$ for the non-punctured model. In fact, it turns out to be close to the exact result obtained for the same $(\beta, L) = (12, 20)$ with $\theta = 0$, which is plotted in the same figure². Thus we find that the topology freezing problem at large β is avoided in the punctured model and then the CLM remains valid.

Next, we discuss the reason why the punctured model can avoid the topology freezing problem without causing large drifts. The difference from the non-punctured model is that one of the plaquettes, P_K , is removed from the action. Note that the topological charge Q_{\log} for the punctured model satisfies

$$Q_{\log}|_{\text{puncture}} - \frac{i}{2\pi} \log P_K = -\frac{i}{2\pi} \sum_n \log P_n = Q_{\log}|_{\text{non-puncture}} . \quad (3.34)$$

The right hand side is the topological charge defined for the corresponding non-punctured model, whose real part takes integer values. The phase of P_K in the left hand side has a real part which lies within the interval $[-\frac{1}{2}, \frac{1}{2})$. When the puncture P_K crosses the brunch cut, its phase changes discontinuously, which causes the topology change. While Q_{\log} for the non-punctured model jumps by ± 1 , Q_{\log} for the punctured model changes smoothly in this process.

²Note that precise agreement is not expected here since the histogram of $\text{Re } Q_{\log}$ is not a holomorphic quantity, for which the CLM does not allow a clear interpretation.

As we discussed in Section 3.3 for the non-punctured model, one of the plaquettes needs to cross the branch cut in order to change the topological charge. When β is large, this process is highly suppressed for all the plaquettes included in the action. This is the reason why the topology freezing problem occurs in the non-punctured model. On the other hand, in the punctured model, the plaquette P_K is removed from the action, and therefore it can cross the branch cut freely even for large β .

This is demonstrated in Fig. 3.8, where we plot the probability distribution of the phase of the puncture P_K as well as that of the other plaquettes $P_{n \neq K}$ for $(\beta, L) = (3, 10), (12, 20)$. We find that the phase of the removed plaquette P_K is almost uniformly distributed for both (β, L) . On the other hand, the distribution of the phase of the other plaquettes depends on (β, L) . It has a compact support for the fine lattice $(\beta, L) = (12, 20)$ but not for the coarse lattice $(\beta, L) = (3, 10)$. For the fine lattice, there is no distribution at the branch cut, which means that the plaquettes $P_{n \neq K}$ does not cross the branch cut at all. For the coarse lattice, there is a small but finite distribution at the branch cut, which means that the value of β is not large enough to suppress the branch cut crossing of the plaquettes $P_{n \neq K}$ completely.

This is consistent with the fact that the histogram of the drift term in Fig. 3.7(Right) fall off fast for $(\beta, L) = (12, 20)$ but not for $(\beta, L) = (3, 10)$ considering the discussion in Section 3.3. In fact, we obtain a similar flow diagram to Fig. 3.4(Left) for the log definition of the topological charge. Therefore, large drifts can appear when one of the plaquettes $P_{n \neq K}$ crosses the branch cut, which indeed occurs for $(\beta, L) = (3, 10)$ also for the punctured model. For $(\beta, L) = (12, 20)$, on the other hand, the topology change can still occur because the removed plaquette P_K crosses the branch cut freely. All the other plaquettes included in the action are forced to stay close to unity because of large β . This justifies our assumption that the issue of the brunch cut can be neglected in deriving the drift terms (3.30) and (3.31). Since the plaquette P_K does not contribute to the drift terms, it never causes large drifts even if it crosses the branch cut frequently. This is the reason why the punctured model can avoid the topology freezing problem without causing large drifts.

3.7 Behavior of the unitarity norm

Next, we discuss how the unitarity norm (3.5) behaves in our complex Langevin simulations. As we can see from (3.30) and (3.31), the link variables around the puncture have a constant drift force in the imaginary direction due to the theta term. At each Langevin step, these link variables are multiplied by $e^{\pm \theta \Delta t / 2\pi}$, and then the removed plaquette is multiplied by $e^{2\theta \Delta t / \pi}$. Therefore, it is possible that the magnitude $|U_{n,\mu}|$ of these four link variables increases or decreases exponentially, so that the unitarity norm grows exponentially with the Langevin time.

In Fig. 3.9, we plot the history of the unitarity norm (3.5) for various θ with $(\beta, L) = (5, 16)$, where the criterion for correct convergence of the CLM is satisfied. As long as it is satisfied, similar results are obtained for other (β, L) . Indeed we observe an exponential growth at early time, but the unitarity norm saturates to a constant depending on θ at sufficiently long Langevin time. This saturation is caused by the propagation of non-

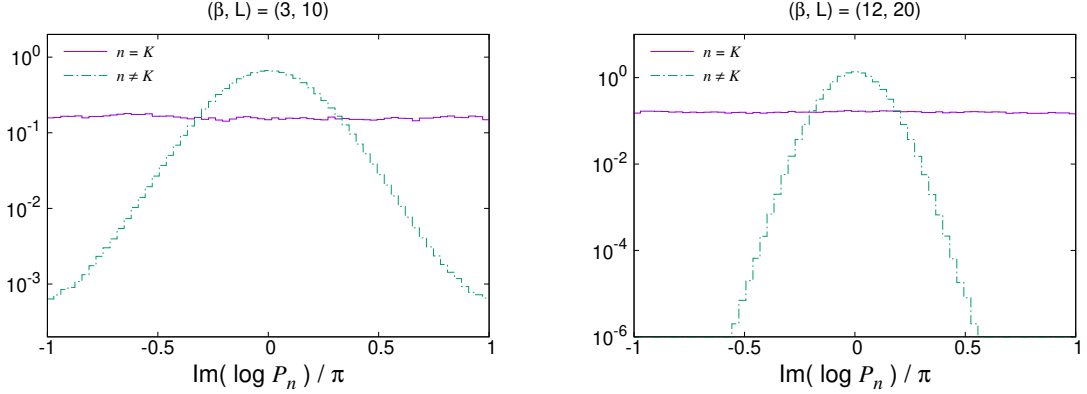


Figure 3.8: The distribution of the phase of the plaquettes is plotted for the punctured model with the log definition (2.11) of the topological charge for $(\beta, L) = (3, 10)$ (Left) and $(\beta, L) = (12, 20)$ (Right) with $\theta = \pi$. We show the results for the plaquette ($n = K$) removed from the action and those for all the other plaquettes ($n \neq K$) by different lines.

unitarity from the four links around the puncture propagates to all the other links. We find that thermalization of various observables can be achieved after the saturation of the unitarity norm.

In fact, we find that the unitarity norm of each link variable is not distributed uniformly on the lattice due to the existence of the puncture. In order to see the distribution, we define the local unitarity norm by

$$\mathcal{N}(n) = \frac{1}{4} \sum_{(k,\mu) \in P_n} \{U_{k,\mu}^* U_{k,\mu} + (U_{k,\mu}^* U_{k,\mu})^{-1} - 2\}, \quad (3.35)$$

which is an average of the unitarity norm for the four link variables composing each plaquette P_n . The unitarity norm defined by (3.5) is an average of $\mathcal{N}(n)$ over all the plaquettes including the removed one; namely $\mathcal{N} = \sum_n \mathcal{N}(n) / L^2$. In Fig. 3.10(Left), we plot $\mathcal{N}(n)$ against $n = (n_1, n_2)$ for $(\beta, L) = (12, 20)$ with $\theta = \pi$. The puncture is located at the center $n = K = (10, 10)$. We observe a sharp peak at the puncture, which goes up to $\mathcal{N}(K) \sim 6 \times 10^3$. The plaquettes adjacent to the puncture have a local unitarity norm $\sim 1.5 \times 10^3$. This implies that the unitarity norm is mostly dominated by the four link variables surrounding the puncture.

What actually matters for the validity of the CLM is not so much the local unitarity norm $\mathcal{N}(n)$ as the absolute value $|P_n|$ of each plaquette, which we plot in Fig. 3.10(Right) against $n = (n_1, n_2)$ for the same parameters as in Fig. 3.10(Left). The absolute value $|P_K|$ of the removed plaquette is close to $(\sqrt{\mathcal{N}(K)})^4 \sim 3.6 \times 10^7$, which implies that $|U_{K,1}|$, $|U_{K+1,2}|$, $|U_{K+2,1}^{-1}|$ and $|U_{K,2}^{-1}|$ are close to $\sqrt{\mathcal{N}(K)} \sim 77$. Except for the removed plaquette, the absolute value of the plaquette deviates slightly from unity for large β . In fact, this deviation of $|P_n|$ for $n \neq K$ from unity has a physical meaning since $\text{Im} \langle Q_{\log} \rangle = -\sum_{n \neq K} \langle \log |P_n| \rangle / 2\pi$ as one can see from (3.34). From the exact result (3.28) obtained for large β , we can estimate $|P_n| \sim e^{-\theta/(2\pi\beta)} \sim 0.96$ for $\theta = \pi$ and $\beta = 12$, which agrees

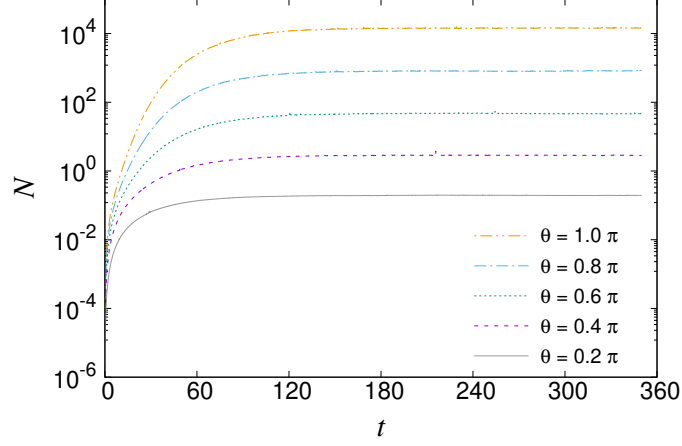


Figure 3.9: The history of the unitarity norm \mathcal{N} is plotted for the punctured model with the log definition (2.11) of the topological charge for various θ with $(\beta, L) = (5, 16)$.

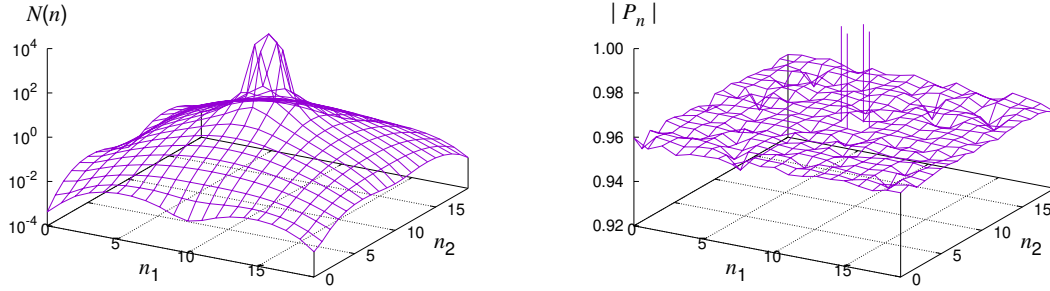


Figure 3.10: The result of the CLM for the punctured model with the log definition (2.11) of the topological charge for $(\beta, L) = (12, 20)$ with $\theta = \pi$. (Left) The local unitarity norm $\mathcal{N}(n)$ for each plaquette P_n defined by (3.35) is plotted against $n = (n_1, n_2)$. (Right) The absolute value of the plaquette P_n is plotted similarly. The puncture corresponds to $n = K = (10, 10)$ in this plot.

with the value observed in Fig. 3.10(Right). If we flip the sign of θ , which corresponds to the parity transformation, we find that $|P_n| \mapsto |P_n|^{-1}$ for all n .

Note also that P_K never appears in the drift term, so that its absolute value can be large without causing large drifts. We have confirmed that the criterion for correct convergence is satisfied for sufficiently large β , and the exact results for various observables can be reproduced correctly as we will see in the next section. This remains to be the case even for large θ and/or large V_{phys} , where the unitarity norm becomes large. Thus the present model provides a counterexample to the common wisdom that the CLM fails when the unitarity norm becomes large.

3.8 Result of the CLM for the punctured model

In this section, we present the observables for the punctured model obtained by the CLM and compare them with the exact results. Note that, in the definitions (3.15), (3.16) and (3.17) of the observables, V denotes the number of plaquettes in the action, which is $V = L^2 - 1$ for the punctured model. In contrast, we define the physical volume V_{phys} by (2.14) not only for the non-punctured model but also for the punctured model, which simplifies the relationship between β and L for fixed V_{phys} .

In Fig. 3.11, we show our results for the average plaquette w , the topological charge density $\langle Q \rangle / V$ and the topological susceptibility χ against θ for $(\beta, L) = (3, 10)$, $(12, 20)$. These parameters correspond to the fixed physical volume $V_{\text{phys}} = L^2 / \beta = 10^2 / 3$. The exact results obtained with the same parameters are also shown for comparison. We find from our results, especially for the average plaquette, that the exact results are reproduced for $(\beta, L) = (12, 20)$, but there is slight deviation for $(\beta, L) = (3, 10)$. This is consistent with our observation in Section 3.6 that the condition for correct convergence is satisfied for $(\beta, L) = (12, 20)$ but not for $(\beta, L) = (3, 10)$.

For the topological charge and the topological susceptibility, we find that our results agree with the exact results also for $(\beta, L) = (3, 10)$. We consider that the agreement observed here for $(\beta, L) = (3, 10)$ is accidental. On the other hand, the results for the non-punctured model with the same (β, L) are far from the exact results as shown in Fig. 3.2(Left). This difference can be understood by considering that the effect of the theta term is included correctly by the drift terms for the link variables around the puncture. The frequent branch cut crossing of the other plaquettes spoils the validity of the CLM.

4 Complex Langevin analysis of 4D SU(2) gauge theory

We analyzed 4D SU(2) gauge theory with a theta term, which attracts our interest since a nontrivial phase structure at $\theta = \pi$ is predicted by the 't Hooft anomaly matching. We can apply the CLM to the 4D gauge theory straightforwardly since its calculation cost depends only linearly on the system size. First, we apply the CLM to the theory with the topological charge naively defined by the clover leaf formula [10]. Then we

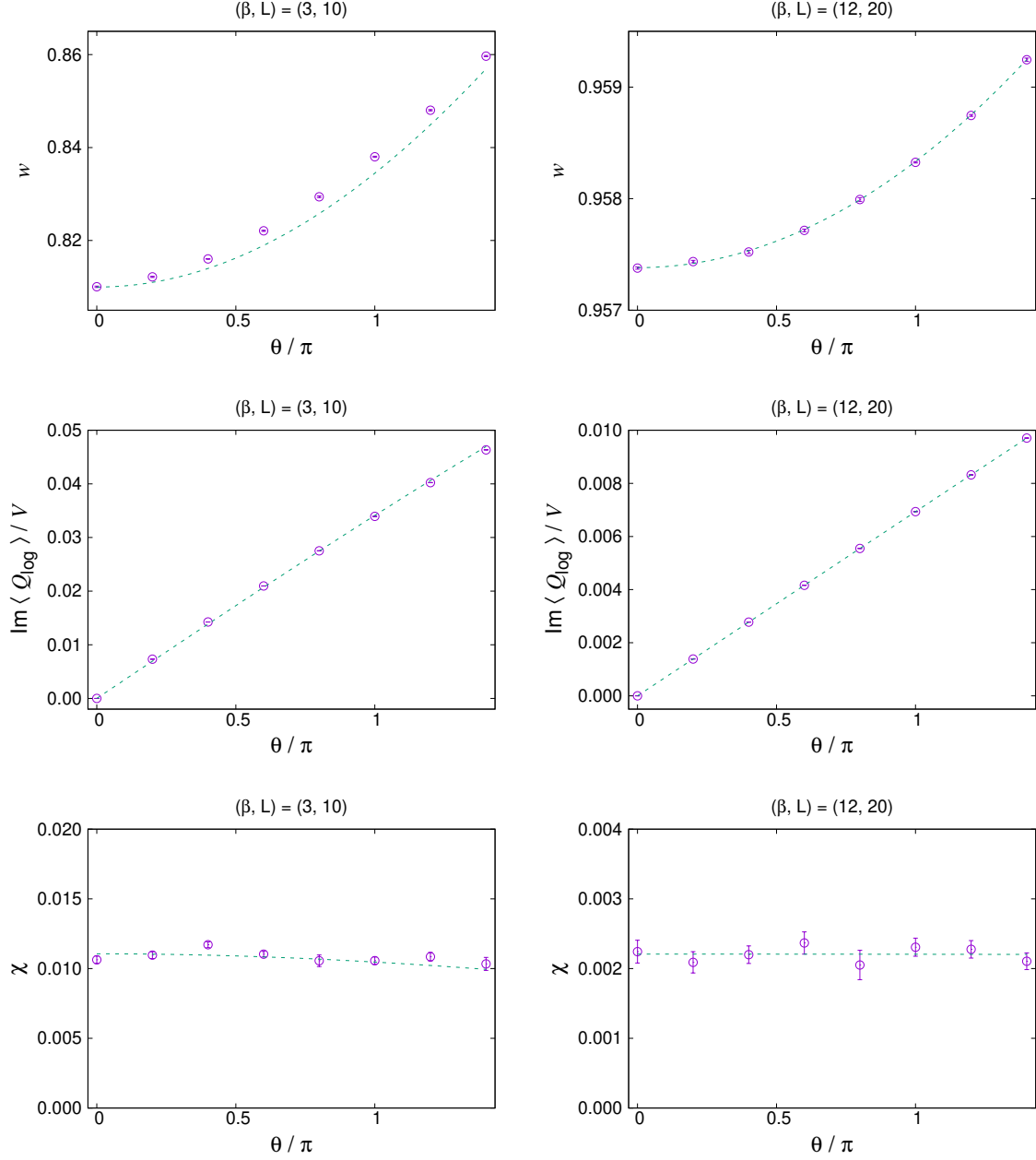


Figure 3.11: The results for various observables obtained by the CLM for the punctured model with the log definition Q_{\log} . The average plaquette (Top), the imaginary part of the topological charge density (Middle), the topological susceptibility (Bottom) are plotted against θ for $(\beta, L) = (3, 10)$ (Left) and $(12, 20)$ (Right). The exact results for the same (β, L) are shown by the dashed lines for comparison.

found that it works in some parameter regions. However, the topological property of the theory is unclear since the topological charge on the lattice is contaminated by the short-range fluctuations. Namely, the topological charge does not approach an integer simply by approaching the continuum limit. The situation is different from the case of 2D where the topological property is clear even on the finite lattice. We tried to deal with this problem by using the stout smearing [11]. We found that it successfully eliminates the short-range fluctuations, but it seems to be difficult to obtain reliable results on the periodic lattice. In fact, there are problems of the singular drift and the topology freezing, which we encountered in the study of 2D U(1) gauge theory. The contents of this section was reported in LATTICE2021 conference [9].

4.1 Application of the CLM to 4D SU(2) gauge theory

We briefly review how to apply the CLM to 4D SU(2) gauge theory. Since real dynamical variables are complexified in the CLM, we extend the link variables $U_{n,\mu} \in \text{SU}(2)$ to $U_{n,\mu} \in \text{SL}(2, \mathbb{C})$, which corresponds to complexifying the gauge field A_μ^a in the continuum theory. Then we consider a fictitious time evolution of the link variables $U_{n,\mu}$ described by the complex Langevin equation

$$U_{n,\mu}(t + \epsilon) = \exp \left[-i\epsilon D_{n,\mu}^a S \tau^a + i\sqrt{\epsilon} \eta_{n,\mu}(t) \right] U_{n,\mu}(t), \quad (4.1)$$

where $\tau^a = \sigma^a/2$ are SU(2) generators. We discretize the fictitious time t by a small step $\epsilon \ll 1$. The factor $D_{n,\mu}^a$ represents the differential operation with respect to the link variables (Lie group elements), which is defined by

$$D_{n,\mu}^a S = \left. \frac{d}{d\epsilon} S(e^{i\epsilon\tau^a} U_{n,\mu}) \right|_{\epsilon \rightarrow 0}. \quad (4.2)$$

The term including $D_{n,\mu}^a S$ is called the drift term. We also have a real Gaussian noise $\eta_{n,\mu}(t) = \eta_{n,\mu}^a(t) \tau^a$ normalized by

$$\langle \eta_{n,\mu}^a(t) \eta_{m,\nu}^b(t') \rangle = 2\delta_{nm} \delta_{\mu\nu} \delta^{ab} \delta_{tt'}. \quad (4.3)$$

We use the action $S = S_g + S_\theta$ of the theory on the lattice defined by (2.24) and $S_\theta = -i\theta Q_{\text{cl}}$ with (2.25).

In order to justify the result of the CLM, we need to confirm that the probability distribution of the drift term falls off exponentially or faster. We can easily check this criterion by plotting the histogram of the magnitude of the largest drift

$$u := \frac{1}{\sqrt{2}} \max_{n,\mu} \|D_{n,\mu}^a S \tau^a\|, \quad (4.4)$$

where the norm of the matrix A is defined by $\|A\|^2 := \text{Tr}[A^\dagger A]$.

As we did in the study of 2D U(1) gauge theory, we stabilize the complex Langevin simulation by gauge cooling [22]. The condition of the correct convergence tends to be violated if the link variables deviates far away from SU(2). The gauge cooling reduces

the non-unitarity of link variables as much as possible. Thus, it helps the condition to be satisfied. It was shown that this procedure does not affect any gauge invariant observable [17, 4]. The procedure of gauge cooling for 4D SU(2) gauge theory is following. First, we define the unitarity norm

$$\mathcal{N} := \frac{1}{8V} \sum_{n,\mu} \text{Tr} [U_{n,\mu}^\dagger U_{n,\mu} - \mathbb{1}] \geq 0 \quad (4.5)$$

which measures the non-unitarity of the configuration. If all the link variables are unitary, the norm is minimized $\mathcal{N} = 0$. The gauge cooling is a $\text{SL}(2, \mathbb{C})$ gauge transformation

$$U_{n,\mu} \longrightarrow g_n U_{n,\mu} g_{n+\mu}^{-1} \quad (4.6)$$

where $g_n \in \text{SL}(2, \mathbb{C})$ is determined so that the unitarity norm can be reduced. Next, we consider an infinitesimal gauge transformation

$$g_n = e^{\Delta_n^a t^a} \approx \mathbb{1} + \Delta_n^a t^a \quad (4.7)$$

with small parameters $\Delta_n^a \ll 1$ on each lattice site. The change of unitarity norm by this transformation is given by

$$\Delta \mathcal{N} = \frac{2}{4NV} \sum_n \Delta_n^a G_n^a, \quad (4.8)$$

where G_n^a is defined by

$$G_n^a = \text{Tr} \left[\sum_\mu \left(U_{n,\mu} U_{n,\mu}^\dagger - U_{n-\mu,\mu}^\dagger U_{n-\mu,\mu} \right) t^a \right]. \quad (4.9)$$

Since G_n^a indicate the direction of the gauge transformation in which \mathcal{N} decreases, we use it for the finite gauge transformation

$$g_n = e^{-\alpha G_n^a t^a} \quad (4.10)$$

with a parameter $\alpha \geq 0$. We choose the value of α which minimize the unitarity norm $\mathcal{N}(\alpha)$ after the transformation. The optimal value of α can be estimated by solving

$$\frac{d\mathcal{N}(\alpha)}{d\alpha} = 0 \quad (4.11)$$

by expanding the left hand side up to the first order of α . As a result, we obtain the explicit form of the solution as

$$\alpha \approx \frac{\sum_n \|G_n\|^2}{\sum_{n,\mu} \|G_n U_{n,\mu} - U_{n,\mu} G_{n+\mu}\|^2}. \quad (4.12)$$

We use this value of α for the transformation (4.10). In the gauge cooling procedure, we repeat this transformation until the change of \mathcal{N} becomes less than 0.01%. We apply the gauge cooling every Langevin step in order to suppress a rapid growth of non-unitarity. We also use the adaptive step size, which is explained in the end of Section 3.1. In the present case, we use the threshold

$$v_0 = \frac{3\beta}{2} (1 + \sqrt{2}), \quad (4.13)$$

which corresponds to the possible maximum value of u for $\theta = 0$.

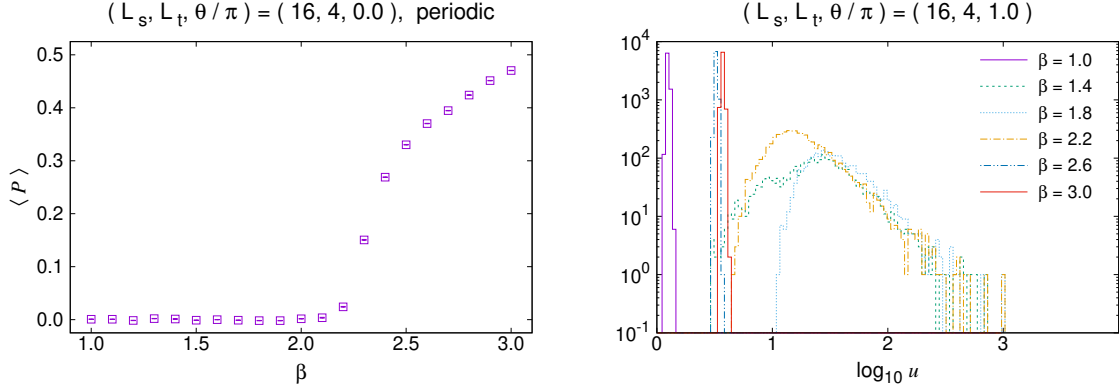


Figure 4.1: The results of the CLM on the $16^3 \times 4$ lattice for various β . (Left) The expectation value of the Polyakov line is plotted against β for $\theta = 0$. (Right) The histograms of the maximum drift term (4.4) are shown for various β with $\theta = \pi$ in log scale. The horizontal axis is $\log_{10} u$.

4.2 Result of CLM with the naive definition of the topological charge

First, we show the results of the CLM with the naive definition of the topological charge Q_{cl} defined in (2.25). In Fig. 4.1(Left), we plot the expectation value of Polyakov line against β , which is obtained for $\theta = 0$. It is zero for small β corresponding to the confined phase, and it becomes finite as we increase β due to the deconfine transition. We also show the histogram of the drift term in Fig. 4.1(Right) at $\theta = \pi$ for various β . From these result, we found that the CLM works for $\beta \approx 1.0$ in the confined phase and $\beta \gtrsim 2.6$ in the deconfined phase. Although the reliable region of the CLM depends on θ and the lattice size, we typically obtain similar results for different parameters.

In order to see the dependence on θ , we show the histograms of the drift term for various θ in Fig. 4.2 with $\beta = 1.0$ (Left) and $\beta = 2.7$ (Right). For $\beta = 1.0$, the CLM works up to $\theta \approx \pi$ but not for large θ . It is natural behavior since the effect of the theta term is significant for larger θ . On the other hand, for $\beta = 2.7$ the validity of the CLM does not simply depend on θ . It can depends on the random number seed in the simulation, which indicates that there is a problem of ergodicity in the large β region. It will be clearer when we use the stout smearing as discussed Section 4.5.

We show the behavior of the topological charge density in Fig. 4.3 obtained by the CLM. We plot the dimensionless quantity $\langle Q \rangle / \chi_0 V$, where χ_0 is the topological susceptibility at $\theta = 0$ defined by

$$\chi_0 := \frac{1}{V} \langle (\langle Q \rangle - Q)^2 \rangle \Big|_{\theta=0} \quad (4.14)$$

and $V = L_s^3 \times L_t$ is a lattice volume. The corresponding histograms of the drift term are shown in Fig. 4.2. Thus some data points in this plot are not reliable. In fact, we cannot see the 2π periodicity of θ in this result. It behaves like $\langle Q \rangle / \chi_0 V \approx i\theta$, which is consistent with the relation (3.18) at least for small θ .

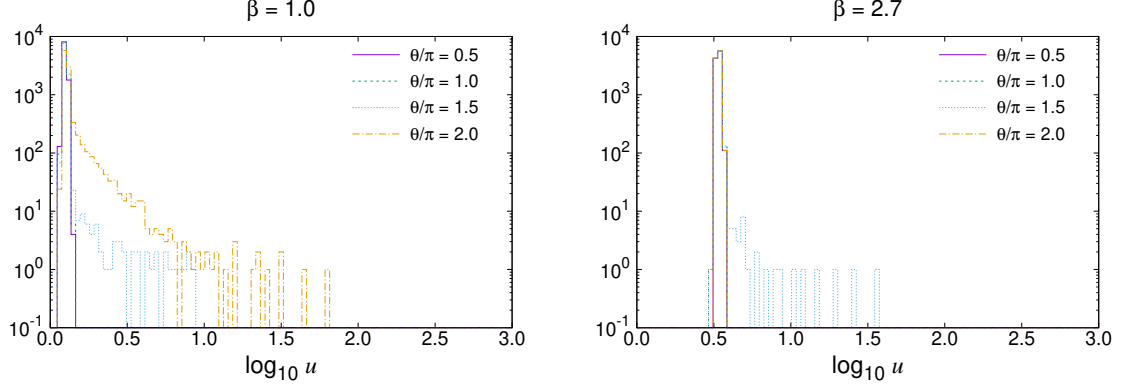


Figure 4.2: The results of the CLM on the $16^3 \times 4$ lattice for various θ . The histograms of the maximum drift term (4.4) are shown for $\beta = 1.0$ (Left) and $\beta = 2.7$ (Right) in log scale. The horizontal axis is $\log_{10} u$.

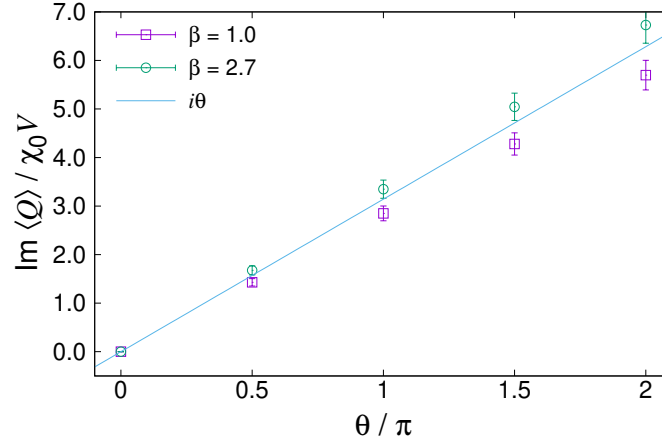


Figure 4.3: The results of the CLM on the $16^3 \times 4$ lattice. The imaginary part of $\langle Q \rangle / \chi V$ is plotted against θ / π for $\beta = 1.0$ and 2.7 .

In spite of the validity of the CLM, it is difficult to reproduce the 2π periodicity of θ since the topological charge on the lattice does not approach an integer by increasing β naively. The situation is different from 2D U(1) gauge theory. In that case, there is the log definition (2.11) of the topological charge, which gives an integer even on the finite lattice. We can also obtain an integer value with the sine definition (2.12) by taking the continuum limit. The problem in 4D SU(2) gauge theory is that the topological charge is contaminated by severe short range fluctuations. We discuss a method to overcome this problem in Section 4.4.

4.3 Analyticity of the complex theta

In this section, we discuss the analyticity of the complexified θ , which supports the consistency of the discussion in Section 5. Although the CLM with the real θ is severely limited, it works at least around $\beta = 1.0$.³ We found that the topological charge density $\langle Q \rangle / V$ behaves as

$$\frac{\langle Q \rangle}{V} \approx i\chi_0\theta \quad (4.15)$$

for $\theta \in \mathbb{R}$ as we can see in Fig. 4.3. This result is consistent with the general formula (3.18) in the theory with the theta term. We can try to see whether the relation (4.15) is extended to the complex plane of $\theta \in \mathbb{C}$. Namely, we can confirm the analyticity of the complexified θ at $\beta = 1.0$ by the CLM.

We parameterize the complex θ by

$$\theta = \pi r e^{i\pi\alpha} \quad (4.16)$$

with $r \geq 0$ and $\alpha \in \mathbb{R}$. The figure 4.4 shows the real/imaginary part of $\langle Q \rangle / i\theta$ obtained by the CLM for various r and α . It is expected to satisfy

$$\frac{\langle Q \rangle}{i\theta} \approx \chi_0 V \in \mathbb{R}. \quad (4.17)$$

The value of $\chi_0 V$ directly calculated at $\theta = 0$ is also plotted. We confirmed that the criterion for the correct convergence is satisfied for these parameters. The results are consistent with the expected behavior (4.17) within the error bar. Therefore, the relation (4.15) seems to be extended to the complex θ plane at least for $\beta = 1.0$.

4.4 Stout smearing in the CLM

The theory with a theta term has the 2π periodicity of θ , which plays an important role in the appearance of the nontrivial phase structure at $\theta = \pi$. However, it is difficult to retain this property on the lattice because the topological charge (2.25) defined by the naive discretization does not take integer values. It approaches integers only for the configurations sufficiently close to the continuum limit. In fact, it is difficult to suppress

³We cannot use the stout smearing for $\beta = 1$ since the unitarity norm quickly grows up during the smearing.

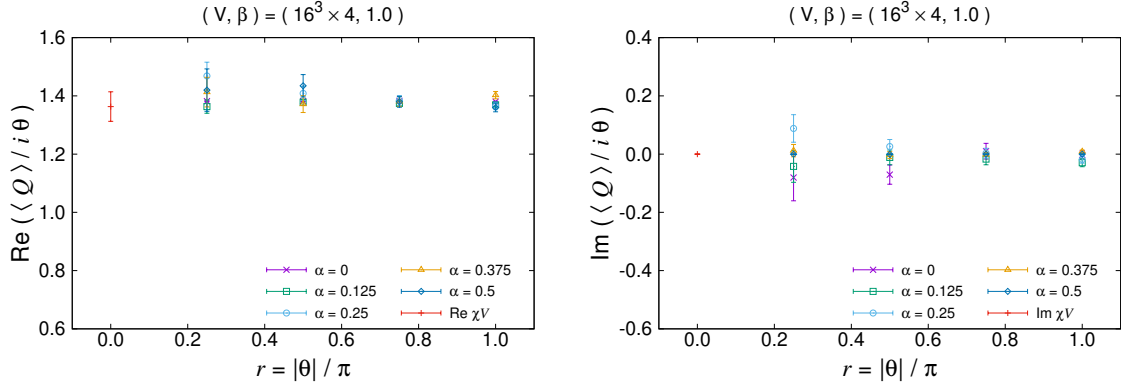


Figure 4.4: The real part (Left) and the imaginary part (Right) of $\langle Q \rangle / i\theta$ obtained by the CLM at $\beta = 1.0$ for various $\theta \in \mathbb{C}$. The value of χV calculated at $\theta = 0$ is also plotted. we use the $16^3 \times 4$ lattice.

short range fluctuations enough simply by increasing β . Thus, we need a smearing method which makes the configuration sufficiently smooth even for small β . In this work, we use the stout smearing [11], which is applicable to the CLM. In fact, its application to the CLM was discussed in the analysis of QCD at nonzero baryon density [25]. In this section, we review how to apply the stout smearing to the complex Langevin simulation of the gauge theory with the theta term.

The procedure of the stout smearing is given by the iteration of the smearing step, starting from the original configuration $U_{n,\mu}$.

$$U_{n,\mu} = U_{n,\mu}^{(0)} \rightarrow U_{n,\mu}^{(1)} \rightarrow \dots \rightarrow U_{n,\mu}^{(N_\rho)} = \tilde{U}_{n,\mu} \quad (4.18)$$

After N_ρ iterations we obtain the smeared configuration $\tilde{U}_{n,\mu}$. In one (isotropic) smearing step from k to $k+1$, the link variable $U_{n,\mu}^{(k)} \in \text{SL}(2, \mathbb{C})$ is mapped to $U_{n,\mu}^{(k+1)} \in \text{SL}(2, \mathbb{C})$ defined by following formulae.

$$U_{n,\mu}^{(k+1)} = e^{iY_{n,\mu}} U_{n,\mu}^{(k)} \quad (4.19)$$

$$iY_{n,\mu} = -\frac{\rho}{2} \text{Tr} [J_{n,\mu} \tau^a] \tau^a \quad (4.20)$$

$$J_{n,\mu} = U_{n,\mu} \Omega_{n,\mu} - \bar{\Omega}_{n,\mu} U_{n,\mu}^{-1} \quad (4.21)$$

$$\Omega_{n,\mu} = \sum_{\sigma \neq \mu} (U_{n+\hat{\mu},\sigma} U_{n+\hat{\sigma},\mu}^{-1} U_{n,\sigma}^{-1} + U_{n+\hat{\mu}-\hat{\sigma},\sigma}^{-1} U_{n-\hat{\sigma},\mu}^{-1} U_{n-\hat{\sigma},\sigma}) \quad (4.22)$$

$$\bar{\Omega}_{n,\mu} = \sum_{\sigma \neq \mu} (U_{n,\sigma} U_{n+\hat{\sigma},\mu} U_{n+\hat{\mu},\sigma}^{-1} + U_{n-\hat{\sigma},\sigma}^{-1} U_{n-\hat{\sigma},\mu} U_{n+\hat{\mu}-\hat{\sigma},\sigma}) \quad (4.23)$$

The parameter $\rho > 0$ should be chosen appropriately, depending on the system.

We use the topological charge (2.25) calculated from the smeared configuration $\tilde{U}_{n,\mu}$

$$Q := Q_{\text{cl}}(\tilde{U}) \quad (4.24)$$

to define the theta term $S_\theta = -i\theta Q$ on the lattice. For the complex Langevin simulation, we need to calculate the drift term $D_{n,\mu}^a S_\theta$ from the theta term. Although S_θ is a complicated function of the original link variable $U_{n,\mu}$, it is possible to calculate the drift force

$$F_{n,\mu} = i\tau^a D_{n,\mu}^a S_\theta \quad (4.25)$$

by reversing the smearing steps (4.18). We define the drift force for the link variables $U_{n,\mu}^{(k)}$ as

$$F_{n,\mu}^{(k)} = i\tau^a D_{n,\mu}^{(k)a} S_\theta, \quad (4.26)$$

where $D_{n,\mu}^{(k)a}$ represents a differential operation with respect to $U_{n,\mu}^{(k)}$. As a first step to calculate (4.25), the calculation of the drift force $\tilde{F}_{n,\mu} = F_{n,\mu}^{(N_\rho)}$ for the smeared link $\tilde{U}_{n,\mu} = U_{n,\mu}^{(N_\rho)}$ is straightforward. Once we obtain the initial drift force $\tilde{F}_{n,\mu}$, the subsequent ones are given by the map from $F_{n,\mu}^{(k)}$ to $F_{n,\mu}^{(k-1)}$ iteratively.

$$\tilde{F}_{n,\mu} = F_{n,\mu}^{(N_\rho)} \rightarrow F_{n,\mu}^{(N_\rho-1)} \rightarrow \dots \rightarrow F_{n,\mu}^{(0)} = F_{n,\mu} \quad (4.27)$$

The map of the drift force is given by the following formulae, where the final step from $F'_{n,\mu} = F_{n,\mu}^{(1)}$ to $F_{n,\mu} = F_{n,\mu}^{(0)}$ is shown as an example.

$$F_{n,\mu} = e^{-iY_{n,\mu}} F'_{n,\mu} e^{iY_{n,\mu}} + \rho \text{Tr} [(U_{n,\mu} M_{n,\mu} + \bar{M}_{n,\mu} U_{n,\mu}^{-1}) \tau^a] \tau^a \quad (4.28)$$

$$\begin{aligned} M_{n,\mu} = & -\Omega_{n,\mu} \Lambda_{n,\mu} \\ & + \sum_{\nu(\neq\mu)} [U_{n+\hat{\mu},\nu} U_{n+\hat{\nu},\mu}^{-1} (U_{n,\nu}^{-1} \Lambda_{n,\nu} + \Lambda_{n+\hat{\nu},\mu} U_{n,\nu}^{-1}) \\ & + U_{n+\hat{\mu}-\hat{\nu},\nu}^{-1} U_{n-\hat{\nu},\mu}^{-1} (\Lambda_{n-\hat{\nu},\mu} - \Lambda_{n-\hat{\nu},\nu}) U_{n-\hat{\nu},\nu} \\ & - \Lambda_{n+\hat{\mu},\nu} U_{n+\hat{\nu},\mu} U_{n+\hat{\nu},\mu}^{-1} U_{n,\nu}^{-1} + U_{n+\hat{\mu}-\hat{\nu},\nu}^{-1} \Lambda_{n+\hat{\mu}-\hat{\nu},\nu} U_{n-\hat{\nu},\mu}^{-1} U_{n-\hat{\nu},\nu}] \end{aligned} \quad (4.29)$$

$$\begin{aligned} \bar{M}_{n,\mu} = & -\Lambda_{n,\mu} \bar{\Omega}_{n,\mu} \\ & + \sum_{\nu(\neq\mu)} [(\Lambda_{n,\nu} U_{n,\nu} + U_{n,\nu} \Lambda_{n+\hat{\nu},\mu}) U_{n+\hat{\nu},\mu} U_{n+\hat{\mu},\nu}^{-1} \\ & + U_{n-\hat{\nu},\nu}^{-1} (\Lambda_{n-\hat{\nu},\mu} - \Lambda_{n-\hat{\nu},\nu}) U_{n-\hat{\nu},\mu} U_{n+\hat{\mu}-\hat{\nu},\nu} \\ & - U_{n,\nu} U_{n+\hat{\nu},\mu} U_{n+\hat{\mu},\nu}^{-1} \Lambda_{n+\hat{\mu},\nu} + U_{n-\hat{\nu},\nu}^{-1} U_{n-\hat{\nu},\mu} \Lambda_{n+\hat{\mu}-\hat{\nu},\nu} U_{n+\hat{\mu}-\hat{\nu},\nu}] \end{aligned} \quad (4.30)$$

$$\Lambda_{m,\nu} = \text{Tr} [\hat{\Lambda}_{m,\nu} \tau^b] \tau^b \quad (4.31)$$

$$\hat{\Lambda}_{m,\nu} = -\frac{1}{2\kappa_{m,\nu}^2} \left(1 - \frac{\sin 2\kappa_{m,\nu}}{2\kappa_{m,\nu}} \right) \text{Tr} [F'_{m,\nu} iY_{m,\nu}] iY_{m,\nu} + \frac{\sin \kappa_{m,\nu}}{\kappa_{m,\nu}} e^{-iY_{m,\nu}} F'_{m,\nu} \quad (4.32)$$

$$\kappa_{n,\mu} = \sqrt{-\det Y_{n,\mu}} \quad (4.33)$$

Note that $Y_{n,\mu}$, $\Omega_{n,\mu}$ and $\bar{\Omega}_{n,\mu}$ are defined by (4.20), (4.22) and (4.23) respectively. They are calculated from $U_{n,\mu}$ in this case. The drift term calculated in this way respects the holomorphicity. The calculation time and the memory size required for the simulation are proportional to the number of steps N_ρ .

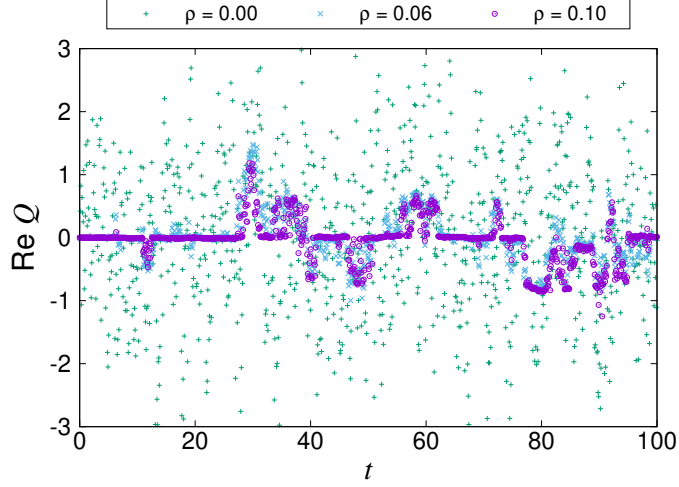


Figure 4.5: The history of the topological charge defined by (4.24) in the Langevin simulation for $\theta = 0$. The lattice size is $24^3 \times 4$, and the coupling constant is $\beta = 2.5$. The horizontal axis is the fictitious time t of the Langevin simulation.

4.5 Result of the CLM with the stout smearing

In this section, we show the results of the complex Langevin simulation. So far, we have found that the CLM using the naive definition (2.25) of the topological charge without the smearing works in the high-temperature region (deconfined phase). As a first step, we focus on the high-temperature region and try to see the effect of the stout smearing on the topological charge.

Before introducing the theta term, we check the effect of the smearing by changing the smearing parameters for $\theta = 0$. The number of steps N_ρ and the step size ρ should be large enough to eliminate the short range fluctuations. However, it is difficult to increase N_ρ a lot since the calculation time and the memory size increase with N_ρ . If ρ is too large, the nontrivial topological excitation will be destroyed. For $\beta > 2.4$, which corresponds to the high-temperature region in our setup, we find that $N_\rho = 20$ is enough to recover the topological property. In figure 4.5, we show the history of the topological charge defined by (4.24) in the real Langevin simulation for $\theta = 0$. There are three series of data with $\rho = 0, 0.06$ and 0.1 . We plot the topological charge without the smearing namely $\rho = 0$ for comparison. The topological charge with $\rho = 0$ is noisy, and it is difficult to see the topological property. Once we introduce the smearing, we can see the transitions between the topological sectors clearly.

Next, we show the results of the complex Langevin simulation for $\theta = \pi/4$. In this simulation, the lattice size is $24^3 \times 4$, and the smearing parameters are $N_\rho = 20$ and $\rho = 0.06$. In figure 4.6, we show the histogram of the magnitude u of the largest drift term defined in (4.4). The distribution falls off rapidly for $\beta = 2.55$, but it does not for $\beta = 2.5$. Thus, the criterion for correct convergence is satisfied only for $\beta = 2.55$. Typically, the coupling constant β should be large enough to satisfy the criterion. We found that the CLM works if $\beta \gtrsim 2.55$ for $\theta = \pi/4$ on the $24^3 \times 4$ lattice.

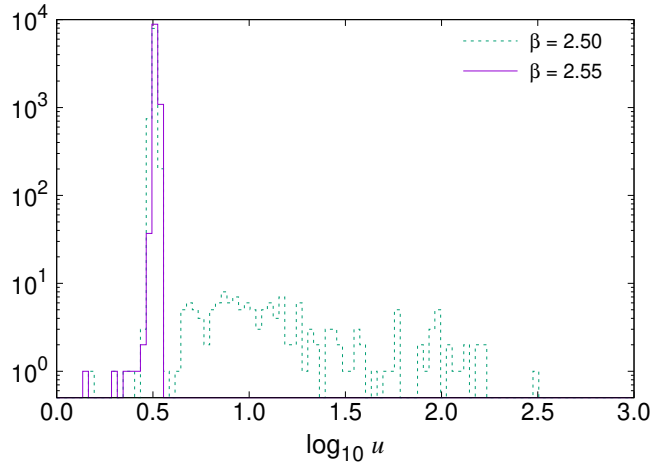


Figure 4.6: The histogram of the maximum drift term (4.4) for $\theta = \pi/4$ in log scale. The horizontal axis is $\log_{10} u$. The lattice size is $24^3 \times 4$, and the smearing parameters are $N_\rho = 20$ and $\rho = 0.06$.

In figure 4.7, we show the history of the topological charge for $\beta = 2.55$. Since the gauge group is extended to $SL(2, \mathbb{C})$ in the CLM, the topological charge has an imaginary part in general. We plot both of the real part and the imaginary part. There are some topological excitations in the history of $\text{Re}Q$. The imaginary part vanishes after the smearing in most cases, but it increases rapidly when the real part changes.

The expectation value of the topological charge has a nonzero imaginary part if CP is broken. Since the theta term breaks CP explicitly for $\theta/\pi \notin \mathbb{Z}$, it is consistent that $\text{Im}Q$ becomes nonzero in our simulation. We find that the fluctuation of $\text{Re}Q$ is necessary to obtain the nonzero $\text{Im}Q$. Indeed, the imaginary part are close to zero while the configuration stays in a single topological sector.

We also find that the rapid growth of $\text{Im}Q$ makes the simulation unstable. The imaginary part originates from the non-unitarity of the configuration, which can be a source of the large drift. We need to set β large enough to avoid this problem. However, the fluctuation of Q is highly suppressed for larger β , and the autocorrelation time of Q becomes longer than the simulation time. It is the topology freezing problem, which we encountered in the study of 2D $U(1)$ gauge theory as well. Therefore, it is difficult to avoid the large drift simply by increasing β further.

4.6 Origin of the large drift

In this section, we investigate the origin of the large drift further. As we discussed in Section 3.6 for 2D $U(1)$ gauge theory, the CLM fails if the plaquettes in the action cross the branch cut frequently. We can possibly understand the failure of the CLM for the 4D $SU(2)$ case in a similar way. Thus we investigated the probability distribution of the phase of plaquette during the complex Langevin simulation.

First, we define the complex phase $\phi \in \mathbb{C}$ of the plaquette $P \in SL(2, \mathbb{C})$ by the phase

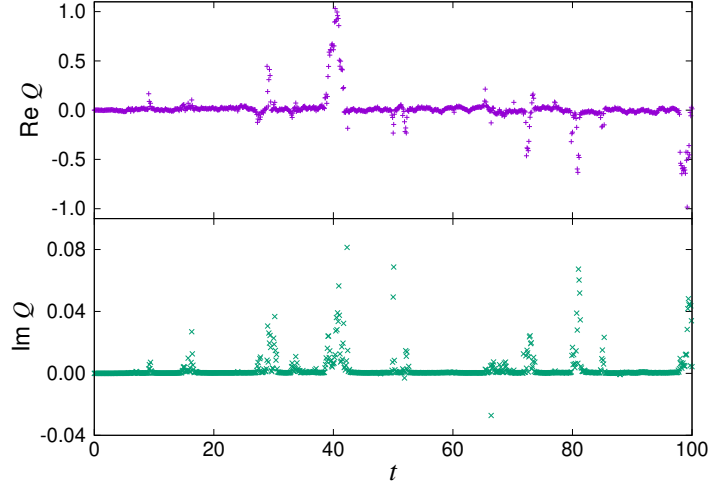


Figure 4.7: The history of the topological charge for $\theta = \pi/4$. The upper plot show the real part and the lower plot show the imaginary part. The lattice size is $24^3 \times 4$, and the coupling constant is $\beta = 2.55$. The horizontal axis is the fictitious time t of the Langevin simulation.

of the eigenvalues $e^{\pm i\phi}$. This phase appears in the trace of the plaquette.

$$\text{Tr}[P] = \text{Tr}[e^{i\phi} + e^{-i\phi}] \quad (4.34)$$

Note that we can set the real part of ϕ be $\text{Re}\phi \geq 0$ without loss of generality. The eigenvalues of the $\text{SL}(2, \mathbb{C})$ matrix P are given by solutions of the equation $\lambda^2 - \lambda \text{Tr}[P] + 1 = 0$, namely,

$$\lambda = \frac{1}{2} \text{Tr}[P] \pm \sqrt{\left(\frac{1}{2} \text{Tr}[P]\right)^2 - 1}. \quad (4.35)$$

Thus we extract the phase ϕ by the complex log of λ with $\text{Re}\phi \geq 0$.

$$\phi = -i \log \lambda \quad (4.36)$$

In fact, this definition is a natural extension of the phase of $\text{U}(1)$ plaquette which we discussed in Section 3.6.

In Fig. 4.8, we show the probability distribution of the phase on the complex ϕ plane for $\beta = 2.4$ and 2.5 . We plot the phase of the plaquette after the smearing as well as that of the original plaquette. For $\beta = 2.4$, where the CLM fails due to the large drift, there is a finite distribution around $\text{Re}\phi = \pi$. In addition, the distribution widely spread to imaginary direction. On the other hand, for $\beta = 2.55$, where the criterion for the correct convergence is satisfied, there is no distribution around $\text{Re}\phi = \pi$ especially for the plaquette after the smearing. The distribution does not spread to the imaginary direction a lot.

From these results, we can see an analogous behavior of the phase of plaquette to that for 2D $\text{U}(1)$ gauge theory, which is shown in Fig. 3.8. The large drift term appears when

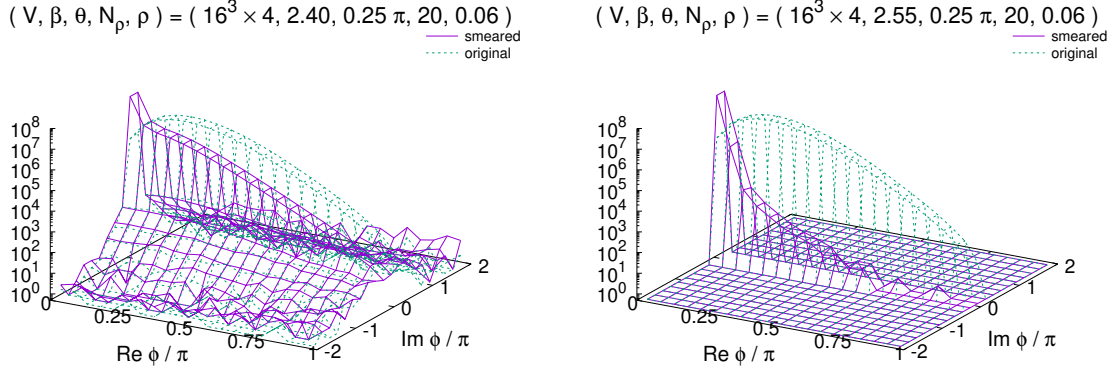


Figure 4.8: The distribution of the phase ϕ of the plaquette in log scale for $\theta = 0.25\pi$ with $\beta = 2.4$ (Left) and 2.5 (Right). We use the $16^3 \times 4$ lattice and set the smearing parameters $(N_\rho, \rho) = (20, 0.06)$. The phase of the plaquette after the smearing is plotted as well as that of the original plaquette.

the phase approaches the branch cut $\text{Re}\phi = \pi$. Although it is not clear like the case of 2D $U(1)$, the topology change seems to be related to the branch cut crossing of the plaquette also for 4D $SU(2)$. Therefore, the problems of the large drift and the topology freezing are correlated on the periodic lattice. Note that we may not realize this problem without the stout smearing because we cannot see this behavior clearly from the naive topological charge.

For 2D $U(1)$ gauge theory, we can avoid this problem by putting a puncture on the lattice. It is possible that we can avoid the problem also for the case of 4D $SU(2)$ by modifying the boundary condition of the lattice. However, nontrivial topological excitations will flow away from the boundaries during the smearing process. So, the implementation of the smearing on the open lattice is not straightforward. It is a significant difference from the case of 2D $U(1)$, where the smearing is not necessary thanks to its milder UV fluctuations.

In addition, since the CP symmetry at $\theta = \pi$ is explicitly broken by the boundary effect, it will be difficult to see the CP restored phase on the open lattice. Note that there is no similar problem in 2D $U(1)$ gauge theory, where the parity symmetry at $\theta = \pi$ is never restored even in the high temperature region. Therefore, we think that it is difficult to investigate the phase diagram of 4D $SU(2)$ gauge theory by the CLM. Instead, we discuss an alternative approach based on analytic continuation in Section 5.

5 4D $SU(2)$ gauge theory with an imaginary theta

We study 4D $SU(2)$ gauge theory with an imaginary theta $\theta \in i\mathbb{R}$, where the action $S = S_g - i\theta Q$ is real. In the current situation, it seems to be difficult to investigate the phase structure directly by the CLM. Instead, we can extract some information of the phase structure by the theory with the imaginary theta. Since the sign problem is absent in this case, we can use the ordinary HMC method. We apply the stout smearing, which

is discussed in Section 4.4, to the HMC in order to make the topological charge close to an integer. We found that the behavior of the topological charge density for the imaginary theta is consistent with that of the instanton gas in the high temperature region. This section is based on the ongoing project. The refined results will be reported in the near future.

5.1 Conjectured phase diagram

First, we present one of the possible phase diagrams on the (θ^2, T) -plane in Fig. 5.1. We extend the parameter θ from the real region $\theta^2 > 0$ to the pure imaginary region $\theta^2 < 0$. In the real θ region, CP symmetry is spontaneously broken on the line at $\theta = \pi$, which terminates at the CP-restoration temperature T_{CP} . It is predicted by 't Hooft anomaly matching that T_{CP} is higher than or equal to the deconfining temperature $T_{\text{dec}}(\pi)$ at $\theta = \pi$. There are similar CP broken lines at $\theta = (2n + 1)\pi$ for $n \in \mathbb{Z}$ because of the 2π periodicity of θ .

For $T < T_{\text{CP}}$, it is expected that, in the real θ region within the range $|\theta| < \pi$, the topological charge density behaves as

$$\frac{\langle Q \rangle}{V} \simeq i\chi_0\theta, \quad (5.1)$$

where χ_0 is the topological susceptibility at $\theta = 0$. The topological charge density changes discontinuously at $\theta = \pi$ because of the first order phase transition. In fact, this is a natural expectation as an analogy to the behavior of $\langle Q \rangle/V$ in 2D U(1) gauge theory. By analytic continuation to the imaginary theta $\theta = i\tilde{\theta}$ with $\tilde{\theta} \in \mathbb{R}$, the corresponding behavior of the topological charge in the imaginary θ region is given by

$$\frac{\langle Q \rangle}{V} \simeq -\chi_0\tilde{\theta}. \quad (5.2)$$

There is also a line of the deconfine transition, which is extended to the imaginary θ region by analytic continuation. The deconfining temperature $T_{\text{dec}}(\theta)$ depends on θ in general. It should be an even function of θ since it is CP invariant. Thus the leading θ dependence of $T_{\text{dec}}(\theta)$ is expected to be θ^2 , namely,

$$\frac{T_{\text{dec}}(\theta)}{T_{\text{dec}}(0)} \simeq 1 - R_2\theta^2, \quad (5.3)$$

with a parameter R_2 . In Fig. 5.1, we show this line with the gradient $R_2 > 0$. In fact, some works on SU(3) gauge theory suggest $R_2 > 0$ for SU(3) [26, 27]. We expect that it is hold also for SU(2).⁴

In the imaginary θ region, we put a line indicating the end of instanton gas phase. For the sufficiently high temperature, we expect that the dilute instanton gas approximation (DIGA) is valid, in which we ignore the interaction of instanton. However, the topological charge density $\langle Q \rangle/V$ increases with $-i\theta$, so that the interaction is no longer negligible

⁴On the other hand, in the large N limit, it is expected that the gradient behaves as $R_2 \propto 1/N^2$.

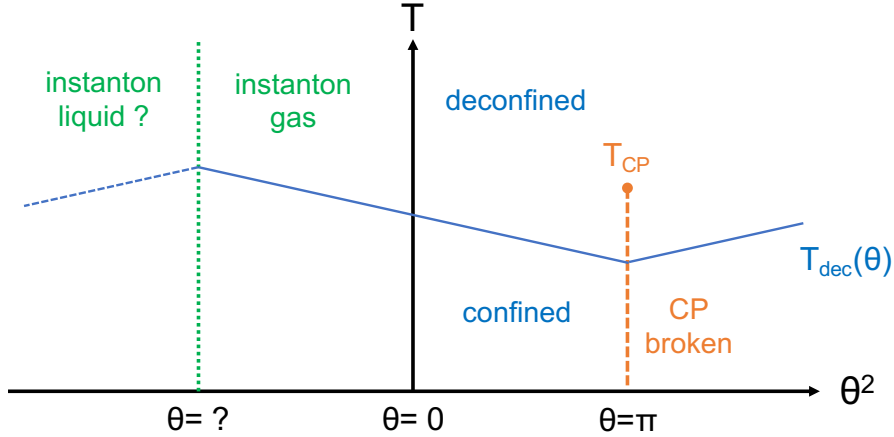


Figure 5.1: The possible phase diagram on the (θ^2, T) -plane. The CP symmetry is spontaneously broken on the orange line at $\theta = \pi$, which terminates at $T = T_{\text{CP}}$. The θ -dependent deconfining temperature $T_{\text{dec}}(\theta)$ is described by the blue line. The dilute instanton gas approximation will break down around the green line at sufficiently large $|\tilde{\theta}|$ in the imaginary θ region.

at some point. It is natural to expect that DIGA breaks down there, entering a different phase. Although we do not know what kind of phase exists there, we can obtain some indications from other models. For example, the study of 2D $O(3)$ sigma model suggested a liquid-like phase [28].

As long as DIGA is justified, the topological charge density behaves as

$$\frac{\langle Q \rangle}{V} \simeq i\chi_0 \sin \theta \quad (5.4)$$

in the real θ region. By analytic continuation, we expect that the topological charge density behaves as

$$\frac{\langle Q \rangle}{V} \simeq -\chi_0 \sinh \tilde{\theta} \quad (5.5)$$

in the pure imaginary θ region. This behavior will be observed up to the line where DIGA breaks down.

5.2 Theta dependence of the topological charge density

We study 4D $SU(2)$ gauge theory with the imaginary theta term by the HMC method. We use the gauge action (2.24) and the theta term $S_\theta = -i\theta Q$ for $\theta = i\tilde{\theta} \in i\mathbb{R}$ with the topological charge defined by (4.24). We apply the stout smearing to the HMC similarly as we did to the CLM in Section (4.4).

We investigate the imaginary θ dependence of the topological charge density $\langle Q \rangle/V$. We expect that it behaves linearly as (5.2) in the deconfined phase $T < T_{\text{dec}}(\pi)$. On the other hand, for the sufficiently high temperature $T > T_{\text{CP}} \geq T_{\text{dec}}(\pi)$, it will behave as (5.5). In Fig. 5.2, we plotted the dimensionless quantity $-\langle Q \rangle/(\chi_0 V)$ against $\tilde{\theta}/\pi = \theta/(i\pi)$

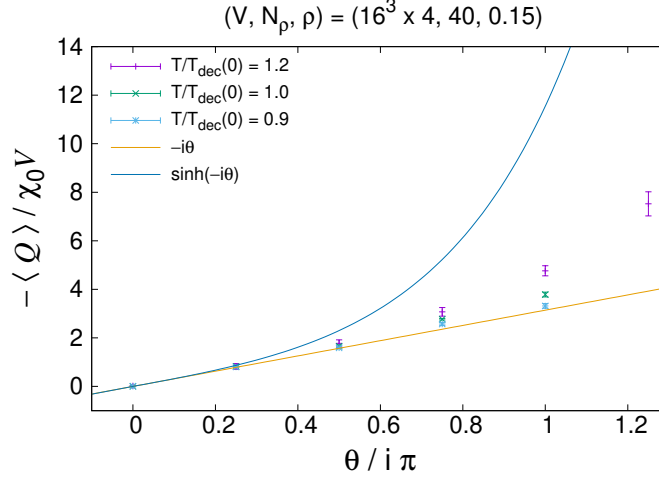


Figure 5.2: The imaginary θ dependence of the topological charge density for various temperatures. The results of $-\langle Q \rangle / (\chi_0 V)$ obtained by HMC on the $V = 16^3 \times 4$ lattice are plotted against $\theta / (i\pi)$. We set the smearing parameters to $N_\rho = 40$ and $\rho = 0.15$. We also plot the expected behaviors (5.2) and (5.5) by solid lines.

for $T/T_{\text{dec}}(0) = 0.9, 1.0$ and 1.2 . The lattice volume is $V = L_s^3 \times L_t = 16^3 \times 4$ in this calculation. Note that we determine the temperature by the equation obtained from [29]

$$\frac{T}{\Lambda_L} = \frac{1}{L_t} \exp \left(\frac{51}{121} \log \frac{11}{6\pi^2\beta} + \frac{3\pi^2\beta}{11} - c_3 \frac{18432\pi^4}{121\beta^3} \right), \quad (5.6)$$

where Λ_L is a lattice cutoff scale and $c_3 = 5.529(63) \times 10^{-4}$. The deconfining temperature is given by $T_{\text{dec}}(0)/\Lambda_L = 21.45(14)$. We set the smearing parameters to $N_\rho = 40$ and $\rho = 0.15$, which is discussed in Appendix D.

For $T/T_{\text{dec}}(0) = 0.9$, the data points are consistent with the expected behavior (5.2) within the errors. We also confirmed that the Polyakov line remains almost zero for any $\tilde{\theta}$ within $0 \leq \tilde{\theta} \leq \pi$, which can be seen in Fig. 5.3. It indicates that the system at $T/T_{\text{dec}}(0) = 0.9$ is still in the confined phase at least in the imaginary θ region.

For $T/T_{\text{dec}}(0) = 1.2$, the data points deviate from the linear behavior (5.2) but it does not agree with (5.5) either. We expect that it approaches (5.5) in the continuum limit, which is discussed in Section 5.4. We also confirmed that the system is in the deconfined phase at this temperature in the imaginary θ region. The imaginary θ dependence of the Polyakov line is shown in Fig. 5.3.

We obtained the results at $T/T_{\text{dec}}(0) = 1.0$ as well. The data points of the topological charge density in Fig. 5.2 are between the results of the other two temperatures. The results of the Polyakov line in Fig. 5.3 fluctuates a lot because the system is very close to the deconfine transition point. In this temperature, we inevitably cross the line of the deconfine transition if we try analytic continuation, as we can see in Fig. 5.1. Thus, we cannot access the real θ region from the imaginary θ region in this case.

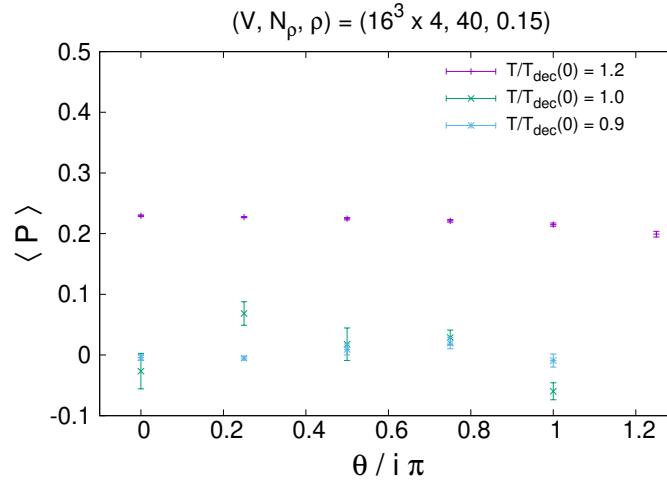


Figure 5.3: The imaginary θ dependence of the Polyakov line for various temperatures. The results obtained by HMC on the $V = 16^3 \times 4$ lattice are plotted against $\theta/(i\pi)$. We set the smearing parameters to $N_\rho = 40$ and $\rho = 0.15$.

5.3 Large volume limit

In this section, we consider the finite volume effect. We performed the simulations by changing spacial lattice size for the fixed β and the fixed temperature $T/T_{\text{dec}}(0) = 1.2$. We use the $V = L_s^3 \times 4$ lattice for $L_s = 12, 14, 16$ and 18 . The results of the topological charge density is shown in Fig. 5.4. The difference among the results of various spacial volumes is as much as the size of error bars.

Next, we focus on the large $\tilde{\theta}$ region, where the finite volume effect will be significant. In Fig. 5.5 we plot the result of $-\langle Q \rangle / (\chi_0 V)$ against $1/L_s^3$ for $\tilde{\theta}/\pi = 0.75$ and 1.0 . We cannot see a significant L_s dependence so far. Therefore, the finite volume effect seems to be small even for the $V = 16^3 \times 4$ lattice at least for $\tilde{\theta} \leq \pi$. It is also possible that we can see some volume dependence when we increase statistics. It is still worth trying the infinite volume extrapolation.

We expect that the finite spacing effect is more significant than the finite volume effect as we will see in Section 5.4. In the continuum limit, indeed, the topological property should be clearer, namely the topological charge on the lattice approaches an integer.

5.4 Continuum limit

In this section, we discuss the continuum limit. We performed simulations for two sets of (β, V) without changing the physical volume nor the temperature. We show the results of the topological charge density for $V = 16^3 \times 4$ and $20^3 \times 5$ in Fig. 5.6. We found that the result for the fine lattice $V = 20^3 \times 5$ almost agrees with the expected behavior (5.5) within the errors, although the size of the error bar increases with $\tilde{\theta}$ as we discuss in Section 5.5. It is expected that the results approach (5.5) in the continuum limit.⁵ Thus,

⁵It is also possible that the result deviates from (5.5) at larger $\tilde{\theta}$ due to the end of instanton gas phase.

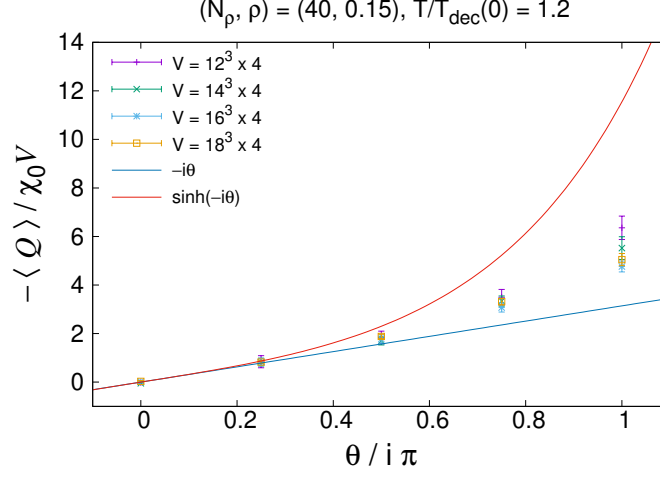


Figure 5.4: The imaginary θ dependence of the topological charge density for various spacial volumes. The results of $-\langle Q \rangle / (\chi_0 V)$ obtained by the HMC for $T/T_{\text{dec}}(0) = 1.2$ are plotted against $\theta/(i\pi)$. We set the smearing parameters to $N_\rho = 40$ and $\rho = 0.15$.

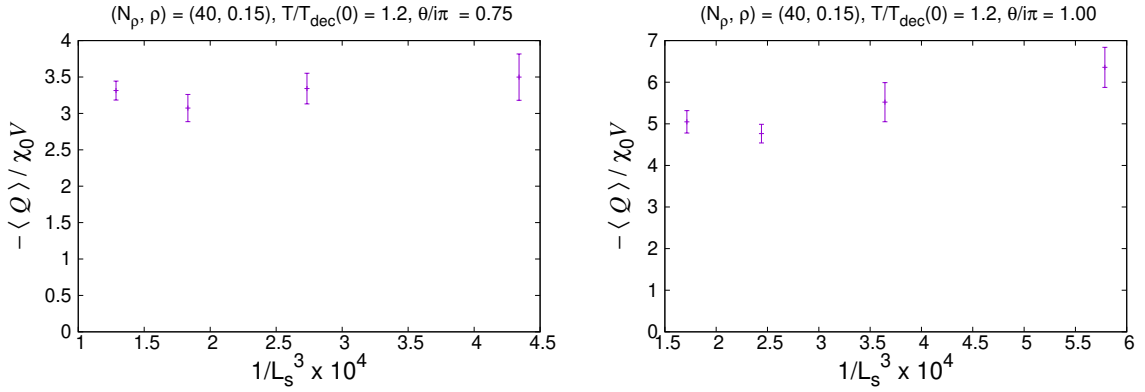


Figure 5.5: The L_s dependence of the topological charge density for $\tilde{\theta}/\pi = 0.75$ (Left) and 1.0 (Right). The results of $-\langle Q \rangle / (\chi_0 V)$ obtained by HMC on the $V = L_s^3 \times 4$ lattice for $T/T_{\text{dec}}(0) = 1.2$ are plotted against $1/L_s^3$. We set the smearing parameters to $N_\rho = 40$ and $\rho = 0.15$.

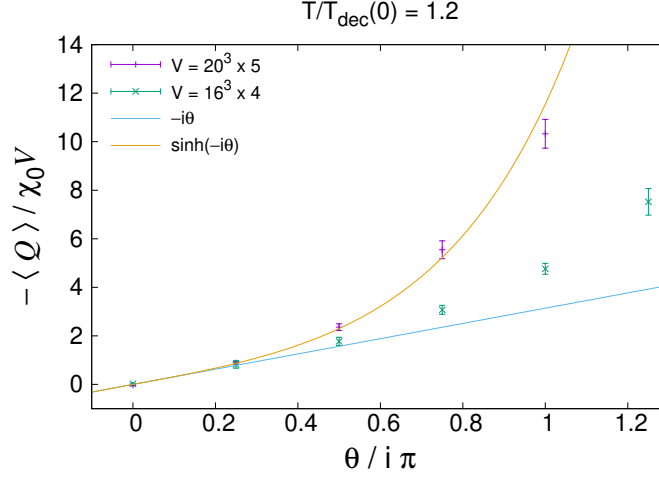


Figure 5.6: The imaginary θ dependence of the topological charge density for different lattice spacings. The results of $-\langle Q \rangle / (\chi_0 V)$ obtained by HMC for $T/T_{\text{dec}}(0) = 1.2$ are plotted against $\theta/(i\pi)$. Two sets of data points correspond to the results for $V = 16^3 \times 4$ and $20^3 \times 5$. The physical volume and the temperature are fixed by adjusting β . We set the smearing parameters to $(N_\rho, \rho) = (40, 0.15)$ for the coarse lattice and $(N_\rho, \rho) = (40, 0.09)$ for the fine lattice.

these results suggest that the topological charge behaves as (5.4) at $T/T_{\text{dec}}(0) = 1.2$ in the real θ region. Namely, the dilute instanton gas approximation should be valid, and the CP symmetry is restored at $\theta = \pi$ at this temperature.

From the results above, we can constrain the phase structure of 4D SU(2) gauge theory under an assumption. If we assume that the system remains in the deconfined phase at $T/T_{\text{dec}}(0) = 1.2$ for $0 \leq \theta \leq \pi$, the CP symmetry at $\theta = \pi$ should be recovered at the same or lower temperature, namely $T_{\text{CP}} \leq 1.2T_{\text{dec}}(0)$. We can continue the similar analysis to make this constraint stronger.

Note that, in these calculations, we used different sets of the smearing parameters because the appropriate one to obtain integer values of Q depends on the lattice size.⁶ We used $(N_\rho, \rho) = (40, 0.15)$ for the coarse lattice and $(N_\rho, \rho) = (40, 0.09)$ for the fine lattice. To eliminate an ambiguity in the determination of these parameters, it will be useful to consider the $\rho \rightarrow 0$ extrapolation by using results with various values of ρ .

5.5 Problem in the large theta region

We found that a problem of autocorrelation appears when we increase $\tilde{\theta}$ in the simulations with imaginary θ . Indeed, we have to decrease the step size of the leap frog in HMC to keep a reasonable acceptance rate. This problem is different from the topology freezing problem, which appears in the large β region. In fact, the autocorrelation is more severe at lower temperature. We show the history of the topological charge for different values of

⁶The appropriate value of ρ depends on β itself as well, but the difference is not significant for the present temperatures.

θ at $T/T_{\text{dec}}(0) = 0.9$ in Fig. 5.7. We can see that the autocorrelation becomes significant as we increase $\tilde{\theta}$. It makes the error bars large in the results above. Furthermore, since we have to decrease the step size of the leap frog, we need a longer computational time for larger $\tilde{\theta}$ with the same t_{HMC} . We need to avoid this problem in order to investigate larger $\tilde{\theta}$ region.

6 Summary

Recently, gauge theories with a theta term attract a lot of interest in the context of 't Hooft anomaly matching. For instance, the phase structure of 4D SU(2) gauge theory at $\theta = \pi$ is constrained by an anomaly matching condition, which can be totally different from that of the large N theory. It is an interesting challenge to investigate the phase structure by first-principle calculation. However, the sign problem prevents us from studying gauge theories with the theta term by the Monte Carlo simulation. In this work, we developed methods to investigate the phase structure of such a theory avoiding the sign problem. We confirmed that the complex Langevin method (CLM) reproduces the exact results for 2D U(1) gauge theory with a puncture (or open boundaries). However, it turned out to be difficult to extend this method to 4D SU(2) gauge theory due to severe UV fluctuations. Then we proposed an alternative method using analytic continuation. We can investigate the phase structure at $\theta = \pi$ indirectly by the HMC with imaginary θ . We summarize the results in this section.

First, we have tried to apply the CLM to gauge theories with a theta term to overcome the sign problem. We focused on 2D U(1) gauge theory, which is exactly solvable on a finite lattice with various boundary conditions. We found that a naive implementation of the method fails due to the topological nature of the theory. While the gauge configurations are complexified in the CLM, one can still define the notion of topological sectors by $\text{Re } Q_{\log} \in \mathbb{Z}$. When a transition between different topological sectors occurs, one of the plaquettes crosses the branch cut inevitably. It results in the frequent appearance of large drift terms. This problem indeed happens at small β , where we found that the criterion for correct convergence of the CLM is not satisfied. By increasing β , the large drift terms do not appear, and the criterion for correct convergence is satisfied. However, the topology change never occurs during the simulation, and then the ergodicity is violated. This is known as the topology freezing problem. The results obtained in this case can be regarded as the expectation values for an ensemble restricted to a particular topological sector specified by the initial configuration.

In order to avoid this problem, we have considered the punctured model, which can be obtained by removing a plaquette from the action. While the quantity $\text{Re } Q_{\log}$ is no longer restricted to integer values, we can still formally classify the complexified configurations into topological sectors by adding back the contribution from the removed plaquette to $\text{Re } Q_{\log}$. The removed plaquette is allowed to cross the branch cut easily even for large β , which results in frequent transitions of topological sectors. Note that, as far as β is sufficiently large, all the other plaquettes are close to unity, and hence large drift

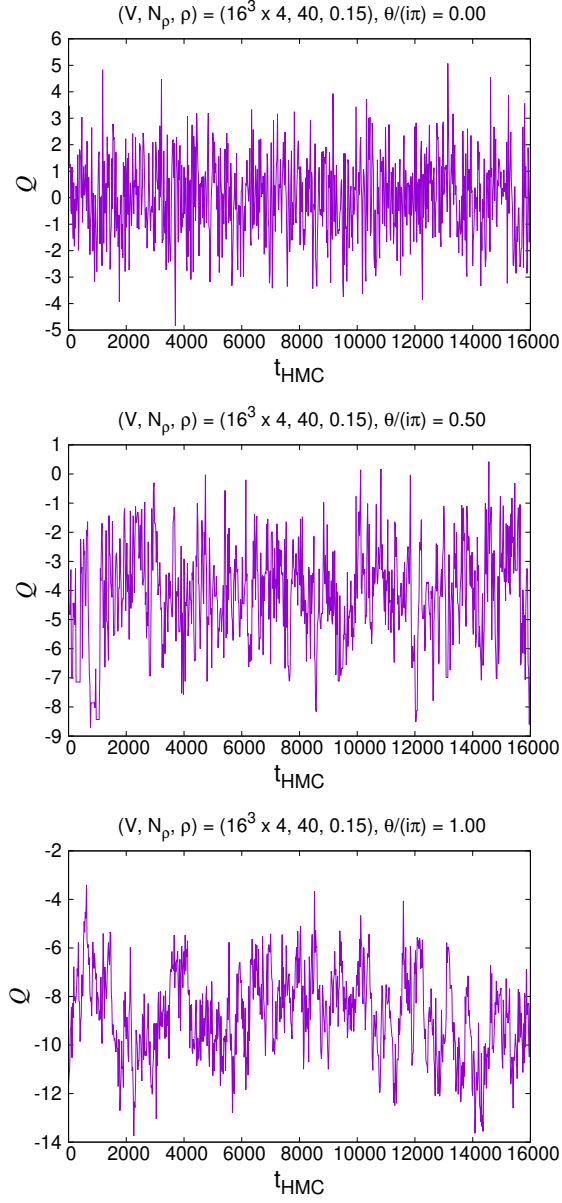


Figure 5.7: The history of the topological charge in HMC for $\tilde{\theta}/\pi = 0$ (Top), 0.5 (Middle) and 1.0 (Bottom) at $T/T_{\text{dec}}(0) = 0.9$ on the $V = 16^3 \times 4$ lattice. We set the smearing parameters to $N_\rho = 40$ and $\rho = 0.15$.

term never appears. Therefore, the criterion for correct convergence of the CLM can be satisfied by simply approaching the continuum limit without causing the topology freezing problem. Indeed the results obtained by the CLM for the punctured model agree with the exact results even at large θ .

In fact, the punctured model is equivalent to the infinite volume limit of the original model for $|\theta| < \pi$. In this limit, the topological charge can take arbitrarily large values, so the discretization of Q to integers is no more important. This equivalence can be confirmed directly by the explicit form of the partition function. In fact, the exact results also indicate the absence of finite volume effects in the punctured model unlike the original model, which exhibits finite volume effects near the critical point $\theta \sim \pi$. It is conceivable that the smoothing of the topological charge distribution somehow removes finite volume effects. If this is correct, a similar conclusion should hold more generally.

Next, we applied the CLM to 4D SU(2) gauge theory. We found that the criterion for correct convergence is satisfied in some parameter regions. However, the naively defined topological charge does not take an integer value due to the contamination by short range fluctuations. For this reason, we introduced the stout smearing to the CLM to recover the topological property. The effect of the smearing can be included in the Langevin dynamics itself as well as in observables. We confirmed that the real part of the topological charge becomes close to an integer after the smearing. On the other hand, the imaginary part vanishes mostly, but it grows rapidly when the real part changes. This behavior is consistent with the topological nature of the theory, although it is difficult to deal with in the numerical simulation.

We need to increase β to suppress the large drift. On the other hand, we cannot increase it due to the topology freezing. It seems to be necessary to resolve either of the topology freezing or the large drift in the CLM. However, the appearance of large drift seems to be related to the topology change, as we found in the study of 2D U(1) gauge theory. In that case, we need to modify the boundary condition or try some possible ways to suppress the large drifts, such as improving the gauge cooling or the smearing method.

We also study 4D SU(2) gauge theory with an imaginary theta term. By considering analytic continuation, we can see the behavior of the observables for real θ via simulations with the imaginary θ . Then we can investigate the phase structure of the real θ region indirectly from the imaginary θ region. However, analyticity of the observables should be broken at the boundary of different phases. We can justify analytic continuation only within the same phase. In spite of this restriction, it is still possible to give some constraints on the phase structure, for example an upper limit of the CP restoration temperature T_{CP} at $\theta = \pi$.

Since the sign problem is absent in the theory with the imaginary θ , we used the hybrid Monte Carlo (HMC) method. We also applied the stout smearing to the HMC as we did to the CLM in order to recover the topological property. We calculated the topological charge density for various $\theta = i\tilde{\theta} \in i\mathbb{R}$. The result suggests that it behaves as $\langle Q \rangle/V \simeq -\chi_0 \sinh \tilde{\theta}$ at $T = 1.2T_{\text{dec}}(0)$, where χ_0 is the topological susceptibility at $\theta = 0$ and $T_{\text{dec}}(\theta)$ is the θ -dependent deconfining temperature. The corresponding behavior in the real θ region should be $\langle Q \rangle/V \simeq i\chi_0 \sin \theta$, which agrees with the prediction by the dilute instanton gas approximation. Since the CP symmetry is restored at $\theta = \pi$ in this

case, the CP restoration temperature T_{CP} should be equal to or lower than $1.2T_{\text{dec}}(0)$. Although we have to assume that $T_{\text{dec}}(\theta) \leq T_{\text{dec}}(0)$ for $0 \leq \theta \leq \pi$, this is a feasible assumption based on the studies of SU(3) gauge theory [27]. In fact, our result is consistent with that obtained by the subvolume method [12, 13].

On the other hand, the topological charge density at $T = 0.9T_{\text{dec}}(0)$ behaves just linearly as $\langle Q \rangle/V \simeq -\chi_0 \tilde{\theta}$. The corresponding behavior in the real θ region should be $\langle Q \rangle/V \simeq i\chi_0 \theta$ up to $\theta = \pi$, which implies the spontaneous breaking of CP. However, since we do not know whether $0.9T_{\text{dec}}(0)$ is still below $T_{\text{dec}}(\pi)$ or not, analytic continuation within the same phase may not be possible. Therefore, it is important to clarify the θ -dependent deconfining temperature $T_{\text{dec}}(\theta)$. If we assume that it is a simple quadratic function of θ , we can estimate the coefficient of θ^2 by investigating $T_{\text{dec}}(\theta)$ at imaginary θ .

We also found that the observables are sensitive to the finite spacing effect of the lattice. It is important to take the continuum limit to obtain quantitatively more reliable results. As a future prospect, we can use an improved action instead of the simple plaquette action (2.24). It is expected that the short range fluctuations are suppressed, and then the required number of the smearing step will be smaller. Thus, we can approach the continuum limit easily.

Acknowledgments

This thesis is based on the collaborative researches with K. Hatakeyama, M. Hirasawa, M. Honda, Y. Ito, J. Nishimura and A. Yosprakob. I would like to thank these collaborators for beneficial discussion and suggestions. In particular, I would like to give a special thank to my supervisor J. Nishimura for a lot of supports. I also would like to thank H. Fukaya, S. Hashimoto, T. Ishikawa, D. Kadoh, R. Kitano, S. Nishigaki, Y. Tanizaki and N. Yamada for valuable discussions.

The computations were carried out on the PC clusters in KEK Computing Research Center and KEK Theory Center. This work is supported by the Particle, Nuclear and Astro Physics Simulation Program No.2020-009 (FY2020) and No.2021-005 (FY2021) of Institute of Particle and Nuclear Studies, High Energy Accelerator Research Organization (KEK).

A Derivation of the partition function of 2D lattice gauge theories

For the 2D lattice gauge theories, we can obtain the partition function explicitly on any manifold at finite lattice spacing and finite volume [8]. Then we can calculate various observables from the partition function. In this section, we review the derivation using the so-called K-functional [7].

A.1 K-functional

We consider a lattice gauge theory with a theta term on a 2D lattice manifold \mathcal{M} . Here we choose $U(N)$ gauge group, which is a generalization of $U(1)$ considered so far. Note that the topology of the gauge field is trivial for $SU(N)$ in 2D gauge theories.

As a building block for evaluation of the partition function, we define the K-functional K_A for the region $A \subset \mathcal{M}$ by [7]

$$K_A(\Gamma) = \int \left(\prod_{U_i \in A \setminus C} dU_i \right) e^{-S_A}, \quad (\text{A.1})$$

where the integral goes over all the link variables inside A except those on the boundary $C = \partial A$. We show the schematic picture of the link variables considered here in Fig. A.1. The action S_A of the theory used in (A.1) is given by

$$S_A = \sum_{P_i \in A} \text{Tr} \left[-\frac{\beta}{2} (P_i + P_i^{-1}) - \frac{\theta}{2\pi} \log P_i \right], \quad (\text{A.2})$$

where the sum goes over all the plaquettes P_i included in the region A . Here we use the log definition (2.11) of the topological charge, but the results for the sine definition (2.12) can be obtained in a similar way as we mention at the end of Section A.4.

Although the K-functional depends on the link variables on the boundary C , due to the gauge invariance, the independent degree of freedom is

$$\Gamma = \prod_{U_i \in C} U_i, \quad (\text{A.3})$$

which is a consecutive product of link variables along the loop C . Note that the final result is independent of the starting point of the loop C since a different choice simply corresponds to applying a gauge transformation to Γ , which leaves the K-functional invariant.

We can calculate the K-functional for any region A by gluing the K-functional for each plaquette P one by one, which is given by

$$K(P) = \exp \text{Tr} \left[\frac{\beta}{2} (P + P^{-1}) + \frac{\theta}{2\pi} \log P \right]. \quad (\text{A.4})$$

Note that the K-functional (A.4) is a function of the group element $P \in U(N)$, which is invariant under the gauge transformation

$$P \rightarrow gPg^{-1}; \quad g \in U(N). \quad (\text{A.5})$$

It is known that any function having this property can be expressed by the character expansion

$$K(P) = \sum_r \lambda_r \chi_r(P), \quad (\text{A.6})$$

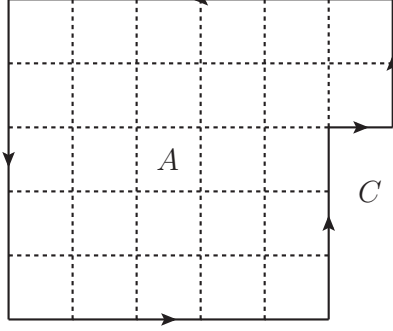


Figure A.1: An example of the region A , which has a boundary $C = \partial A$. The K-functional for this region is defined by integrating out internal link variables represented by the dashed lines. The result depends on Γ defined by (A.3) for the loop C represented by the solid line with arrows.

which is analogous to the Fourier expansion of a periodic function. Here $\chi_r(P)$ is the character of the group, which is defined by the trace of the group element P for the irreducible representation r , and it satisfies the orthogonality relation

$$\int dU \chi_{r_1}(U^{-1}) \chi_{r_2}(U) = \delta_{r_1, r_2}. \quad (\text{A.7})$$

Using this relation, the coefficient λ_r in the expansion (A.6) can be extracted as

$$\lambda_r = \int dU \chi_r(U^{-1}) K(U). \quad (\text{A.8})$$

As an example, let us obtain the K-functional $K_{2 \times 1}$ for a 2×1 rectangle by gluing two neighboring plaquettes $P_1 = U_1 \Omega$ and $P_2 = \Omega^{-1} U_2$ as shown in Fig. A.2. Here the group elements U_1 and U_2 are the products of three link variables, and Ω represents the link variable shared by P_1 and P_2 . Integrating out the shared link variable Ω , we obtain

$$\begin{aligned} K_{2 \times 1}(U_1 U_2) &= \int d\Omega K(P_1) K(P_2) \\ &= \sum_{r_1, r_2} \lambda_{r_1} \lambda_{r_2} \int d\Omega \chi_{r_1}(U_1 \Omega) \chi_{r_2}(\Omega^{-1} U_2) \\ &= \sum_r d_r \left(\frac{\lambda_r}{d_r} \right)^2 \chi_r(U_1 U_2), \end{aligned} \quad (\text{A.9})$$

where $d_r = \chi_r(1)$ is the dimension of the representation r . We have used a formula

$$\int d\Omega \chi_{r_1}(U_1 \Omega) \chi_{r_2}(\Omega^{-1} U_2) = \frac{1}{d_{r_1}} \chi_{r_1}(U_1 U_2) \delta_{r_1, r_2} \quad (\text{A.10})$$

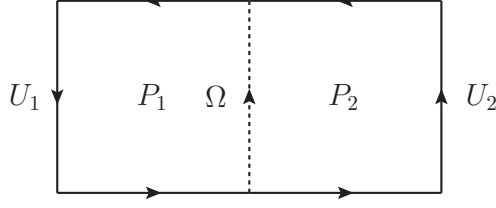


Figure A.2: The K-functional $K_{2 \times 1}$ for a 2×1 rectangle is obtained by gluing the K-functional for the two plaquettes $P_1 = U_1 \Omega$ and $P_2 = \Omega^{-1} U_2$ by integrating out the shared link variable Ω .

to combine two characters. Iterating this procedure, we obtain the K-functional for any simply connected region A as

$$K_A(\Gamma) = \sum_r d_r \left(\frac{\lambda_r}{d_r} \right)^{|A|} \chi_r(\Gamma), \quad (\text{A.11})$$

where $|A|$ represents the number of plaquettes in A , and Γ is defined by (A.3).

In the case of $U(1)$ gauge theory, the representation can be labeled simply by the charge $n \in \mathbb{Z}$, and the dimension of the representation is $d_n = 1$ for any n . Since the character for the plaquette $P = e^{i\phi}$ is given by $\chi_n(P) = e^{in\phi}$, the K-functional for a single plaquette (A.6) reduces to the Fourier series

$$K(P) = \sum_{n \in \mathbb{Z}} \lambda_n e^{in\phi}. \quad (\text{A.12})$$

The coefficient λ_n is a function of θ and β , which is given explicitly by an integral

$$\begin{aligned} \lambda_n &= \mathcal{I}(n, \theta, \beta) \\ &:= \frac{1}{2\pi} \int_{-\pi}^{\pi} d\phi e^{-in\phi} K(P = e^{i\phi}) \\ &= \frac{1}{2\pi} \int_{-\pi}^{\pi} d\phi \exp \left[\beta \cos \phi + i \left(\frac{\theta}{2\pi} - n \right) \phi \right] \end{aligned} \quad (\text{A.13})$$

using (A.4) with $P = e^{i\phi}$. Note that this function reduces to the modified Bessel function of the first kind for $\theta = 0$.

The character expansion for the $U(N)$ group is much more complicated, so we show the results only here. The detailed derivation can be found, for example, in the appendix of [30]. The representation of the $U(N)$ group is labeled by N integers

$$\rho = (\rho_1, \rho_2, \dots, \rho_N) \in \mathbb{Z}^N \quad (\text{A.14})$$

satisfying $\rho_i \geq \rho_{i+1}$, and the dimension of the representation ρ is given by

$$d_\rho = \chi_\rho(1) = \prod_{i>j}^N \left(1 - \frac{\rho_i - \rho_j}{i - j} \right). \quad (\text{A.15})$$

The coefficient λ_ρ for the representation ρ in the character expansion (A.6) is expressed as a determinant

$$\lambda_\rho = \det \mathcal{M}(\rho, \theta, \beta) \quad (\text{A.16})$$

of the matrix $\mathcal{M}(\rho, \theta, \beta)$, which is defined by

$$\mathcal{M}_{jk}(\rho, \theta, \beta) := \frac{1}{2\pi} \int_{-\pi}^{\pi} d\phi \exp \left[\beta \cos \phi + i \left(\frac{\theta}{2\pi} + \rho_k + j - k \right) \phi \right]. \quad (\text{A.17})$$

This matrix can be regarded as a generalization of (A.13).

A.2 Partition function for the non-punctured model

First, we evaluate the partition function of the 2D $U(N)$ lattice gauge theory on a torus. We first consider the K-functional $K_{L_1 \times L_2}$ for a rectangle composed of $V := L_1 \times L_2$ plaquettes, which can be expressed as (A.11). As shown in Fig. A.3, we identify the top and bottom sides represented by U^{-1} and U , respectively, and also identify the left and right sides represented by W^{-1} and W . By integrating out the group elements U and W , we obtain the partition function for the non-punctured model as

$$\begin{aligned} Z_{\text{nonpunc}} &= \int dU dW K_{L_1 \times L_2}(UWU^{-1}W^{-1}) \\ &= \sum_r d_r \left(\frac{\lambda_r}{d_r} \right)^V \int dU dW \chi_r(UWU^{-1}W^{-1}) \\ &= \sum_r \left(\frac{\lambda_r}{d_r} \right)^V \int dU \chi_r(U) \chi_r(U^{-1}) \\ &= \sum_r \left(\frac{\lambda_r}{d_r} \right)^V, \end{aligned} \quad (\text{A.18})$$

where we have used the orthogonality relation (A.7) and a formula

$$\int d\Omega \chi_r(U\Omega W\Omega^{-1}) = \frac{1}{d_r} \chi_r(U) \chi_r(W). \quad (\text{A.19})$$

For the $U(1)$ gauge theory, the partition function (A.18) reduces to

$$Z_{\text{nonpunc}} = \sum_{n \in \mathbb{Z}} [\mathcal{I}(n, \theta, \beta)]^V. \quad (\text{A.20})$$

As we can see from (A.13), the integral $\mathcal{I}(n, \theta, \beta)$ has a property

$$\mathcal{I}(n, \theta + 2\pi k, \beta) = \mathcal{I}(n - k, \theta, \beta) \quad (\text{A.21})$$

for $\forall k \in \mathbb{Z}$, which indeed guarantees the 2π periodicity of θ in the partition function (A.20).

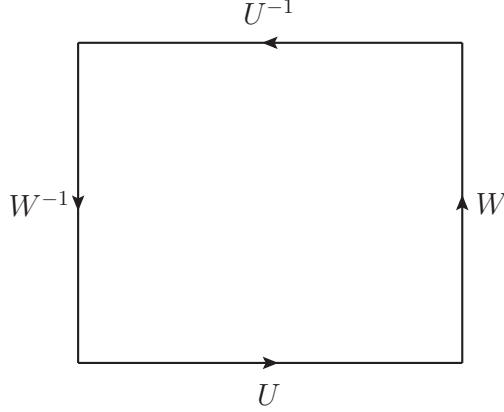


Figure A.3: The partition function of 2D $U(N)$ gauge theory on a torus is obtained from the K-functional for the rectangle by integrating out the group elements U and W corresponding to the identified sides.

Then let us consider the continuum limit, which corresponds to taking the $V \rightarrow \infty$ and $\beta \rightarrow \infty$ limits simultaneously with the fixed physical volume $V_{\text{phys}} := V/\beta$. In this limit, the integral (A.13) can be evaluated as

$$\mathcal{I}(n, \theta, \beta) \simeq \frac{1}{\sqrt{2\pi\beta}} \exp \left[\beta - \frac{1}{2\beta} \left(\frac{\theta}{2\pi} - n \right)^2 \right]. \quad (\text{A.22})$$

Substituting this expression into (A.20), we obtain the partition function of the continuum theory

$$\begin{aligned} Z_{\text{nonpunc}} &\simeq \left(\frac{e^\beta}{\sqrt{2\pi\beta}} \right)^V \sum_{n \in \mathbb{Z}} \exp \left[-\frac{V}{2\beta} \left(\frac{\theta}{2\pi} - n \right)^2 \right] \\ &\sim \sum_{n \in \mathbb{Z}} \exp \left[-\frac{1}{2} V_{\text{phys}} \left(\frac{\theta}{2\pi} - n \right)^2 \right], \end{aligned} \quad (\text{A.23})$$

omitting the divergent constant factor.

A.3 Partition function for the punctured model

Next, we extend the calculation in the previous section to the punctured model. As a building block, we calculate the K-functional for a rectangle with a hole shown in Fig. A.4. It can be divided into two regions A_1 and A_2 by cutting along two segments Ω_1 and Ω_2 . The outer and inner boundaries of the rectangle are divided into two segments (U_1, U_2)

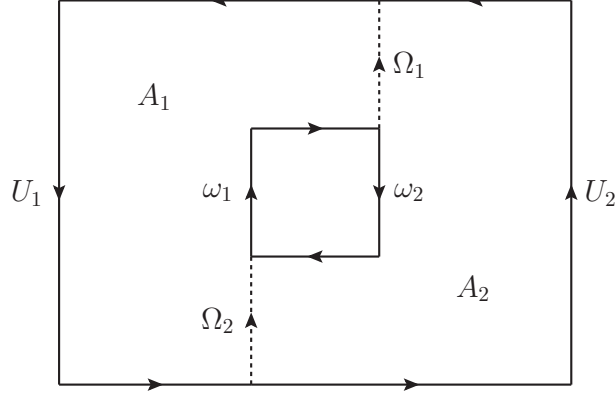


Figure A.4: The K-functional for a rectangle with a hole is obtained by gluing the two regions A_1 and A_2 . Then, the K-functional for the punctured torus is obtained just as we did in Fig. A.3. By integrating out the link variables surrounding the puncture, we obtain the partition function of 2D $U(N)$ gauge theory on a punctured torus.

and (ω_1, ω_2) , respectively. Then, the K-functional for each region is given as follows.

$$K_{A_1}(U_1 \Omega_2 \omega_1 \Omega_1) = \sum_{r_1} d_{r_1} \left(\frac{\lambda_{r_1}}{d_{r_1}} \right)^{|A_1|} \chi_{r_1}(U_1 \Omega_2 \omega_1 \Omega_1) \quad (\text{A.24})$$

$$K_{A_2}(\Omega_1^{-1} \omega_2 \Omega_2^{-1} U_2) = \sum_{r_2} d_{r_2} \left(\frac{\lambda_{r_2}}{d_{r_2}} \right)^{|A_2|} \chi_{r_2}(\Omega_1^{-1} \omega_2 \Omega_2^{-1} U_2) \quad (\text{A.25})$$

By gluing the two regions A_1 and A_2 together at Ω_1 and Ω_2 , we obtain the K-functional for the rectangle with a hole as

$$\begin{aligned} K_{A_1 \cup A_2} &= \int d\Omega_1 d\Omega_2 K_{A_1}(U_1 \Omega_2 \omega_1 \Omega_1) K_{A_2}(\Omega_1^{-1} \omega_2 \Omega_2^{-1} U_2) \\ &= \sum_{r_1, r_2} d_{r_1} d_{r_2} \left(\frac{\lambda_{r_1}}{d_{r_1}} \right)^{|A_1|} \left(\frac{\lambda_{r_2}}{d_{r_2}} \right)^{|A_2|} \int d\Omega_1 d\Omega_2 \chi_{r_1}(U_1 \Omega_2 \omega_1 \Omega_1) \chi_{r_2}(\Omega_1^{-1} \omega_2 \Omega_2^{-1} U_2) \\ &= \sum_r d_r \left(\frac{\lambda_r}{d_r} \right)^{|A_1|} \left(\frac{\lambda_r}{d_r} \right)^{|A_2|} \int d\Omega_2 \chi_r(U_1 \Omega_2 \omega_1 \omega_2 \Omega_2^{-1} U_2) \\ &= \sum_r \left(\frac{\lambda_r}{d_r} \right)^V \chi_r(U_1 U_2) \chi_r(\omega_1 \omega_2), \end{aligned} \quad (\text{A.26})$$

where we have defined $V := |A_1 \cup A_2| = |A_1| + |A_2|$.

Let us introduce the group elements U and W for the outer boundary as we did in Fig. A.3 so that $U_1 U_2 = U W U^{-1} W^{-1}$, and define $\omega := \omega_1 \omega_2$ for the inner boundary. By integrating out the group elements U and W , we obtain the K-functional for the

punctured torus as

$$\begin{aligned}
K_{\text{punc}}(\omega) &= \sum_r \left(\frac{\lambda_r}{d_r} \right)^V \chi_r(\omega) \int dU dW \chi_r(UWU^{-1}W^{-1}) \\
&= \sum_r \left(\frac{\lambda_r}{d_r} \right)^V \chi_r(\omega) \int dU \frac{1}{d_r} \chi_r(U) \chi_r(U^{-1}) \\
&= \sum_r \frac{1}{d_r} \left(\frac{\lambda_r}{d_r} \right)^V \chi_r(\omega).
\end{aligned} \tag{A.27}$$

Finally, we have to integrate out the remaining degree of freedom ω around the puncture. Then we obtain the partition function for the punctured model as

$$Z_{\text{punc}} = \int d\omega K_{\text{punc}}(\omega) = \sum_r \frac{1}{d_r} \left(\frac{\lambda_r}{d_r} \right)^V \delta_{r,0} = (\lambda_0)^V, \tag{A.28}$$

where $r = 0$ corresponds to the trivial representation with the dimension $d_0 = 1$.

In the case of $U(1)$, the partition function reduces to

$$Z_{\text{punc}} = [\mathcal{I}(0, \theta, \beta)]^V, \tag{A.29}$$

which does not have the 2π periodicity of θ as expected.

We next consider taking the continuum limit, namely $V \rightarrow \infty$ and $\beta \rightarrow \infty$ limits simultaneously with the fixed physical volume $V_{\text{phys}} := V/\beta$. Similarly to the case of the non-punctured model, which is discussed in Section A.2, we obtain

$$\begin{aligned}
Z_{\text{punc}} &\simeq \left(\frac{e^\beta}{\sqrt{2\pi\beta}} \right)^V \exp \left[-\frac{V}{2\beta} \left(\frac{\theta}{2\pi} \right)^2 \right] \\
&\sim \exp \left[-\frac{1}{2} V_{\text{phys}} \left(\frac{\theta}{2\pi} \right)^2 \right],
\end{aligned} \tag{A.30}$$

omitting the divergent constant factor. This coincides with the infinite volume limit $V_{\text{phys}} \rightarrow \infty$ of (A.23) within the range $|\theta| < \pi$. Note, however, that the equivalence between the punctured and non-punctured models does not hold for finite physical volume V_{phys} .

A.4 Evaluation of the observables

We can evaluate the expectation values of various observables defined in Section 3.2 from the partition function derived above, namely (A.20) for the non-punctured model and (A.29) for the punctured model. Since the latter case is straightforward because of the absence of an infinite sum, we only discuss the former case below.

The average plaquette w defined by (3.15) is given by

$$w = \frac{1}{Z_{\text{nonpunc}}} \sum_{n \in \mathbb{Z}} \mathcal{A}(n, \theta, \beta) [\mathcal{I}(n, \theta, \beta)]^V, \tag{A.31}$$

where we have defined

$$\begin{aligned}
\mathcal{A}(n, \theta, \beta) &:= \frac{\partial}{\partial \beta} \log \mathcal{I}(n, \theta, \beta) \\
&= \frac{1}{\mathcal{I}(n, \theta, \beta)} \frac{1}{2\pi} \int_{-\pi}^{\pi} d\phi \cos \phi \exp \left[\beta \cos \phi + i \left(\frac{\theta}{2\pi} - n \right) \phi \right] \\
&= \frac{\mathcal{I}(n-1, \theta, \beta) + \mathcal{I}(n+1, \theta, \beta)}{2\mathcal{I}(n, \theta, \beta)}.
\end{aligned} \tag{A.32}$$

Similarly, the topological charge density defined by (3.16) can be obtained from

$$\langle Q \rangle = -i \frac{V}{Z_{\text{nonpunc}}} \sum_{n \in \mathbb{Z}} \mathcal{B}(n, \theta, \beta) [\mathcal{I}(n, \theta, \beta)]^V, \tag{A.33}$$

where we have defined

$$\begin{aligned}
\mathcal{B}(n, \theta, \beta) &:= \frac{1}{\mathcal{I}(n, \theta, \beta)} \frac{\partial}{\partial \theta} \mathcal{I}(n, \theta, \beta) \\
&= \frac{i}{\mathcal{I}(n, \theta, \beta)} \frac{1}{4\pi^2} \int_{-\pi}^{\pi} d\phi \phi \exp \left[\beta \cos \phi + i \left(\frac{\theta}{2\pi} - n \right) \phi \right].
\end{aligned} \tag{A.34}$$

Finally, the topological susceptibility defined by (3.17) can be obtained from

$$\langle Q^2 \rangle = -\frac{V}{Z_{\text{nonpunc}}} \sum_{n=-\infty}^{+\infty} [\mathcal{C}(n, \theta, \beta) + (V-1)\mathcal{B}(n, \theta, \beta)^2] [\mathcal{I}(n, \theta, \beta)]^V, \tag{A.35}$$

where we have defined

$$\begin{aligned}
\mathcal{C}(n, \theta, \beta) &:= \frac{1}{\mathcal{I}(n, \theta, \beta)} \frac{\partial^2}{\partial \theta^2} \mathcal{I}(n, \theta, \beta) \\
&= -\frac{1}{\mathcal{I}(n, \theta, \beta)} \frac{1}{8\pi^3} \int_{-\pi}^{\pi} d\phi \phi^2 \exp \left[\beta \cos \phi + i \left(\frac{\theta}{2\pi} - n \right) \phi \right].
\end{aligned} \tag{A.36}$$

Note that $\mathcal{I}(n, \theta, \beta)$ and the functions (A.32), (56) and (A.36) derived from it are all real-valued, and we can calculate them by numerical integration with sufficient precision. When we evaluate the infinite sum in the expressions (A.31), (A.33) and (A.35), we have to truncate it at some n . Note here that $|\mathcal{I}(n, \theta, \beta)|$ decays quickly as $|\theta/2\pi - n|$ increases. We can therefore evaluate the infinite sum with sufficient precision by keeping only a few terms when the volume V_{phys} is sufficiently large.

So far we have derived the exact results for the log definition (2.11) of the topological charge. As is clear from the derivation, we can obtain the exact results for the sine definition (2.12) by simply replacing $\mathcal{I}(n, \theta, \beta)$ by

$$\tilde{\mathcal{I}}(n, \theta, \beta) := \frac{1}{2\pi} \int_{-\pi}^{\pi} d\phi \exp \left[\beta \cos \phi + i \frac{\theta}{2\pi} \sin \phi - in\phi \right]. \tag{A.37}$$

B The punctured model with the sine definition Q_{\sin}

In Sections 3.4 and 3.5, we have discussed the punctured model with the log definition (2.11) of the topological charge for simplicity. In fact, we also obtained the results by using the sine definition (2.12) for the punctured model. Here we show the results, which are qualitatively similar to those with the log definition.

The drift terms for the sine definition are given already for the non-punctured model in Section 3.1. When we consider the punctured model, the only modification from the original model appears in the drift terms for the four link variables surrounding the puncture, namely $U_{K,1}$, $U_{K+\hat{2},1}$, $U_{K,2}$ and $U_{K+\hat{1},2}$. Thus, the drift terms are given as follows.

$$D_{n,1}S = \begin{cases} -i\frac{\beta}{2}(P_n - P_n^{-1} - P_{n-\hat{2}} + P_{n-\hat{2}}^{-1}) - i\frac{\theta}{4\pi}(P_n + P_n^{-1} - P_{n-\hat{2}} - P_{n-\hat{2}}^{-1}) & \text{for } n \neq K, K + \hat{2} \\ -i\frac{\beta}{2}(-P_{K-\hat{2}} + P_{K-\hat{2}}^{-1}) + i\frac{\theta}{4\pi}(P_{K-\hat{2}} + P_{K-\hat{2}}^{-1}) & \text{for } n = K \\ -i\frac{\beta}{2}(P_{K+\hat{2}} - P_{K+\hat{2}}^{-1}) - i\frac{\theta}{4\pi}(P_{K+\hat{2}} + P_{K+\hat{2}}^{-1}) & \text{for } n = K + \hat{2} \end{cases} \quad (\text{B.1})$$

$$D_{n,2}S = \begin{cases} -i\frac{\beta}{2}(-P_n + P_n^{-1} + P_{n-\hat{1}} - P_{n-\hat{1}}^{-1}) - i\frac{\theta}{4\pi}(-P_n - P_n^{-1} + P_{n-\hat{1}} + P_{n-\hat{1}}^{-1}) & \text{for } n \neq K, K + \hat{1} \\ -i\frac{\beta}{2}(P_{K-\hat{1}} - P_{K-\hat{1}}^{-1}) - i\frac{\theta}{4\pi}(P_{K-\hat{1}} + P_{K-\hat{1}}^{-1}) & \text{for } n = K \\ -i\frac{\beta}{2}(-P_{K+\hat{1}} + P_{K+\hat{1}}^{-1}) + i\frac{\theta}{4\pi}(P_{K+\hat{1}} + P_{K+\hat{1}}^{-1}) & \text{for } n = K + \hat{1} \end{cases} \quad (\text{B.2})$$

At large β , all the plaquettes except the removed one P_K approach unity. The drift term from the theta term therefore vanishes for all the link variables except for those surrounding the puncture, which have constant drifts $\pm i\frac{\theta}{2\pi}$. Thus, in the continuum limit, the drift terms for the sine definition agree with those for the log definition given by (3.30) and (3.31). This relation makes it easier to understand why we can safely ignore the singularity in the drift term for the log definition discussed in Section 3.1.

It is therefore expected that the results of the CLM for the sine definition are essentially the same as those for the log definition for large β . In Fig. B.1, we show our results for the punctured model with the sine definition for the same (β, L) as those in Fig. 3.7 with the log definition. For the fine lattice $(\beta, L) = (12, 20)$, we found that the histogram of the magnitude u of the drift term falls off rapidly. In addition, the histogram of $\text{Re } Q_{\sin}$ obtained by the CLM is widely distributed. Hence, the topology freezing problem is circumvented without causing large drifts similarly to the situation with the log definition.

On the other hand, for the coarse lattice $(\beta, L) = (3, 10)$, we find that the histogram of the magnitude u of the drift term falls off fast. It means that the condition for the validity of the CLM is satisfied unlike the case of the log definition. As a result, all the observables are in complete agreement with the exact results for all values of θ even for $(\beta, L) = (3, 10)$. This can be seen from Fig. B.2, where we show the results for the punctured model with the sine definition for the same values of (β, L) as the ones used in Fig. 3.11. For coarser lattice $(\beta, L) = (1.92, 8)$ with the same $V_{\text{phys}} = L^2/\beta$, however, we actually found that the histogram has a power-law tail. Therefore, the difference between the two definitions is merely a small shift in the validity region of the CLM.

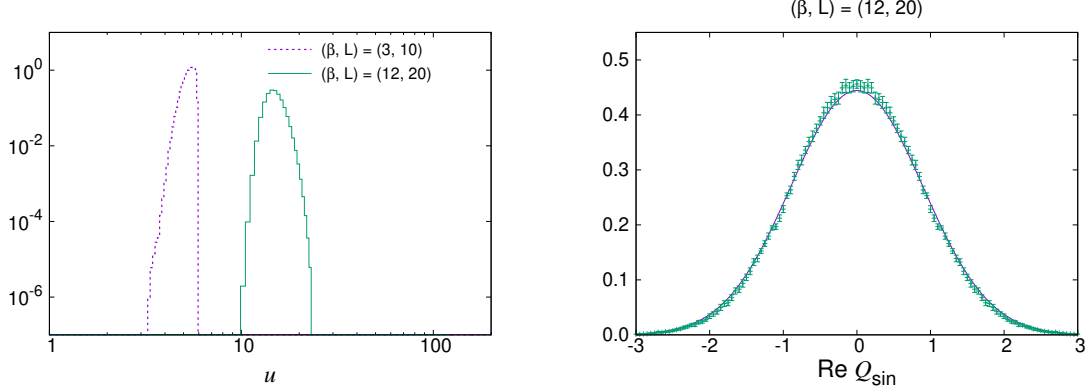


Figure B.1: The results obtained by the CLM for the punctured model using the sine definition of the topological charge. (Left) The histogram of the magnitude u of the drift term is shown for $(\beta, L) = (3, 10)$ and $(12, 20)$ with $\theta = \pi$. (Right) The histogram of $\text{Re } Q_{\text{sin}}$ for the punctured model is shown for $(\beta, L) = (12, 20)$ with $\theta = \pi$. The exact result obtained for $(\beta, L) = (12, 20)$ with $\theta = 0$ is shown by the solid line for comparison.

We also show the exact results for the punctured model with the log and sine definitions for comparison. They tend to agree with each other as β is increased with fixed V_{phys} , which corresponds to the continuum limit.

C Derivation of the formulae for the stout smearing

The stout smearing was first proposed in [11] for the HMC simulation of QCD. It was also applied to the complex Langevin simulation of QCD at finite baryon chemical potential [25]. In this section, we review the derivation of the formulae for the stout smearing focusing on the case of SU(2) gauge theory.

The procedure of the stout smearing is given by the iteration of the smearing step, starting from the original configuration $U_{n,\mu}$.

$$U_{n,\mu} = U_{n,\mu}^{(0)} \rightarrow U_{n,\mu}^{(1)} \rightarrow \dots \rightarrow U_{n,\mu}^{(N_\rho)} = \tilde{U}_{n,\mu} \quad (\text{C.1})$$

After N_ρ iterations we obtain the smeared configuration $\tilde{U}_{n,\mu}$. In one (isotropic) smearing step from k to $k+1$, the link variable $U_{n,\mu}^{(k)} \in \text{SL}(2, \mathbb{C})$ is mapped to $U_{n,\mu}^{(k+1)} \in \text{SL}(2, \mathbb{C})$ defined by following formulae.

$$U_{n,\mu}^{(k+1)} := e^{iY_{n,\mu}} U_{n,\mu}^{(k)}, \quad (\text{C.2})$$

$$iY_{n,\mu} := -\frac{\rho}{2} \text{Tr} [J_{n,\mu}^{(\beta)} t^a] t^a = -\frac{\rho}{2} \left(J_{n,\mu}^{(\beta)} - \frac{1}{N} \text{Tr} [J_{n,\mu}^{(\beta)}] \mathbb{1} \right) \quad (\text{C.3})$$

$$J_{n,\mu}^{(\beta)} := U_{n,\mu} \Omega_{n,\mu} - \bar{\Omega}_{n,\mu} U_{n,\mu}^{-1} \quad (\text{C.4})$$

$$\Omega_{n,\mu} := \sum_{\sigma (\neq \mu)} (U_{n+\mu,\sigma} U_{n+\sigma,\mu}^{-1} U_{n,\sigma}^{-1} + U_{n+\mu-\sigma,\sigma}^{-1} U_{n-\sigma,\mu}^{-1} U_{n-\sigma,\sigma}) \quad (\text{C.5})$$

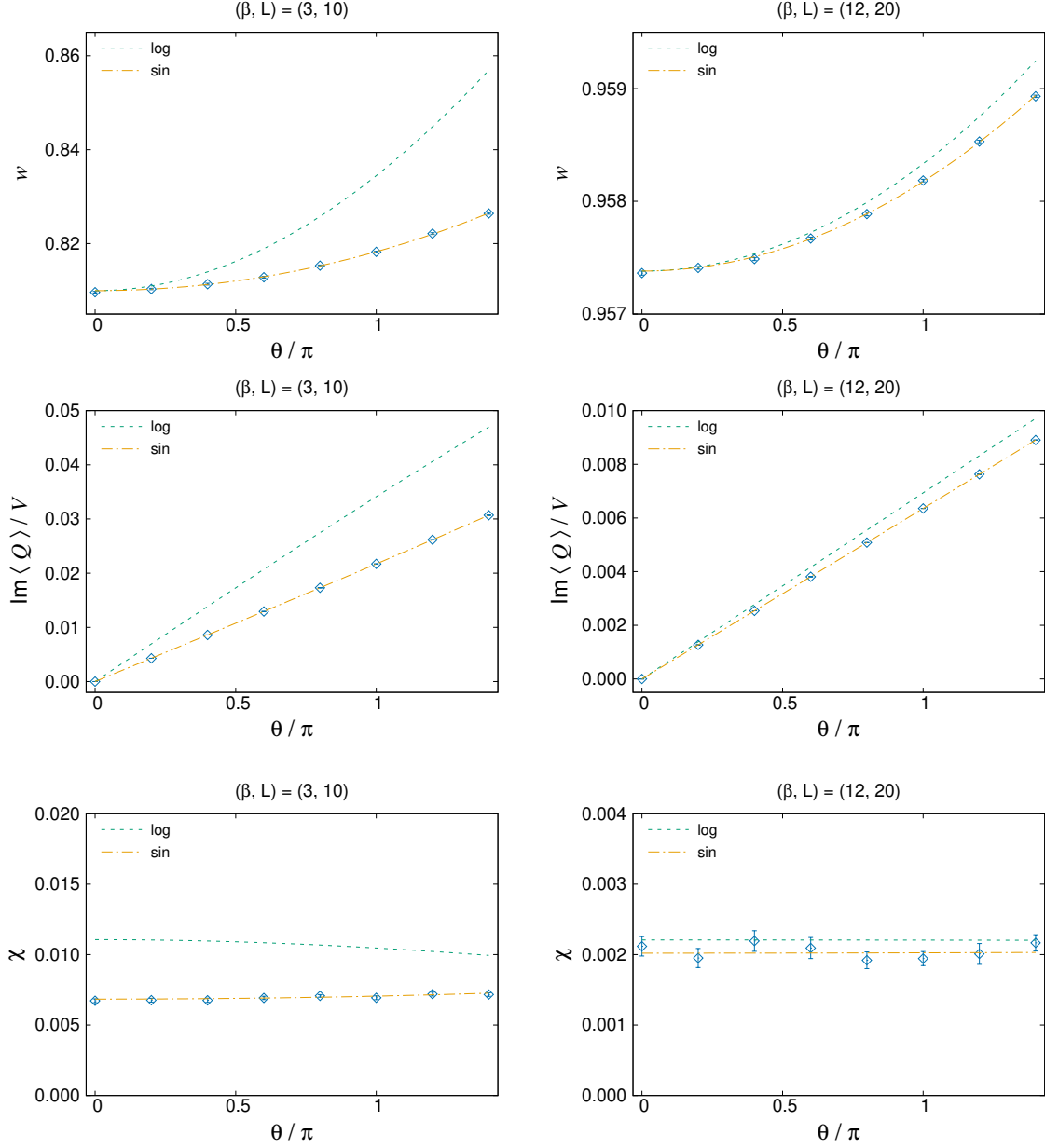


Figure B.2: The results for various observables obtained by the CLM for the punctured model with the sine definition Q_{sin} . The average plaquette (Top), the imaginary part of the topological charge density (Middle), the topological susceptibility (Bottom) are plotted against θ/π for $(\beta, L) = (3, 10)$ (Left) and $(12, 20)$ (Right). The exact results for the punctured model with the log and sine definitions are shown for the same (β, L) by the dashed lines and the dash-dotted lines, respectively, for comparison.

$$\bar{\Omega}_{n,\mu} := \sum_{\sigma(\neq\mu)} (U_{n,\sigma} U_{n+\sigma,\mu} U_{n+\mu,\sigma}^{-1} + U_{n-\sigma,\sigma}^{-1} U_{n-\sigma,\mu} U_{n+\mu-\sigma,\sigma}) \quad (\text{C.6})$$

In the update (C.2), the matrix exponential of the traceless 2×2 matrix $Y_{n,\mu}$ can be calculated by

$$e^{iY_{n,\mu}} = \cos \kappa_{n,\mu} \mathbb{1} + f(\kappa_{n,\mu}) iY_{n,\mu}, \quad (\text{C.7})$$

where $\pm \kappa_{n,\mu}$ are the eigenvalues of $Y_{n,\mu}$

$$\kappa_{n,\mu} := \sqrt{-\det Y_{n,\mu}} = \sqrt{\frac{1}{2} \text{Tr} Y_{n,\mu}^2} \quad (\text{C.8})$$

and $f(x)$ is the analytic function of $x \in \mathbb{C}$.

$$f(x) := \frac{\sin x}{x} = 1 - \frac{1}{6}x^2 + \mathcal{O}(x^4) \quad (\text{C.9})$$

Next, we consider the calculation of the drift term for the action $S[\tilde{U}(U)]$ which is calculated from the smeared link variables. Although $S[\tilde{U}(U)]$ is a complicated function of the original link variable $U_{n,\mu}$, it is possible to calculate the drift force

$$F_{n,\mu} = i\tau^a D_{n,\mu}^a S \quad (\text{C.10})$$

by reversing the smearing steps. We define the drift force for the link variables $U_{n,\mu}^{(k)}$ as

$$F_{n,\mu}^{(k)} = i\tau^a D_{n,\mu}^{(k)a} S_\theta, \quad (\text{C.11})$$

where $D_{n,\mu}^{(k)a}$ represents a differential operation with respect to $U_{n,\mu}^{(k)}$. Once we obtain the drift force $\tilde{F}_{n,\mu} = F_{n,\mu}^{(N_\rho)}$ of the smeared links, the subsequent ones are given by the map from $F_{n,\mu}^{(k)}$ to $F_{n,\mu}^{(k-1)}$ iteratively.

$$\tilde{F}_{n,\mu} = F_{n,\mu}^{(N_\rho)} \rightarrow F_{n,\mu}^{(N_\rho-1)} \rightarrow \dots \rightarrow F_{n,\mu}^{(0)} = F_{n,\mu} \quad (\text{C.12})$$

In order to derive the formulae of the map $F_{n,\mu}^{(k)} \rightarrow F_{n,\mu}^{(k-1)}$, we focus on the first smearing step $U_{n,\mu} \rightarrow U_{n,\mu}^{(1)} =: U'_{n,\mu}$ and calculate the drift term $D_{n,\mu}^a S[U'(U)]$ of the original link variable. First, we define the variation of U'

$$\Delta_{n,\mu;m,\nu}^{a;b} := -2i\text{Tr} [(D_{n,\mu}^a U'_{m,\nu}) U'^{-1}_{m,\nu} t^b] \quad (\text{C.13})$$

which satisfies

$$i\alpha^a \Delta_{n,\mu;m,\nu}^{a;b} t^b = 2\alpha^a \text{Tr} [(D_{n,\mu}^a U'_{m,\nu}) U'^{-1}_{m,\nu} t^b] t^b = \alpha^a (D_{n,\mu}^a U'_{m,\nu}) U'^{-1}_{m,\nu} \quad (\text{C.14})$$

for any $\alpha^a \in \mathbb{R}$ ($a = 1, 2, 3$). This equation can be show by using the formula

$$\text{Tr} [W t^a] t^a = \frac{1}{2} \left(W - \frac{1}{N} \text{Tr} [W] \mathbb{1} \right) \quad (\text{C.15})$$

for the $SU(N)$ generators, which is based on the identity

$$t_{ij}^a t_{kl}^a = \frac{1}{2} \left(\delta_{il} \delta_{jk} - \frac{1}{N} \delta_{ij} \delta_{kl} \right). \quad (\text{C.16})$$

Note that the trace part vanishes in this case.

$$\begin{aligned} \text{Tr} \left[(D_{n,\mu}^a U'_{m,\nu}) U'^{-1}_{m,\nu} \right] &= \text{Tr} \left[D_{n,\mu}^a (e^{iY_{m,\nu}} U_{m,\nu}) U_{m,\nu}^{-1} e^{-iY_{m,\nu}} \right] \\ &= \text{Tr} \left[e^{-iY_{m,\nu}} D_{n,\mu}^a e^{iY_{m,\nu}} + U_{m,\nu}^{-1} D_{n,\mu}^a U_{m,\nu} \right] \\ &= \text{Tr} \left[e^{-iY_{m,\nu}} (D_{n,\mu}^a iY_{m,\nu}) e^{iY_{m,\nu}} + i\delta_{n,m} \delta_{\mu,\nu} U_{m,\nu}^{-1} t^a U_{m,\nu} \right] \\ &= D_{n,\mu}^a \text{Tr} [iY_{m,\nu}] + i\delta_{n,m} \delta_{\mu,\nu} \text{Tr} [t^a] \\ &= 0 \end{aligned} \quad (\text{C.17})$$

By using (C.13), the small change of $U_{n,\mu}$ can be rephrased by that of $U'_{n,\mu}$ up to the first order in α^a .

$$\begin{aligned} U'_{m,\nu} (e^{i\alpha^a t^a} U_{n,\mu}) &\approx U'_{m,\nu} + \alpha^a \left[\frac{\partial}{\partial \epsilon} U'_{m,\nu} (e^{i\epsilon t^a} U_{n,\mu}) \right]_{\epsilon=0} \\ &= [\mathbb{1} + \alpha^a (D_{n,\mu}^a U'_{m,\nu}) U'^{-1}_{m,\nu}] U'_{m,\nu} \\ &\approx e^{i\alpha^a \Delta_{n,\mu;m,\nu}^{a;b} t^b} U'_{m,\nu} \end{aligned} \quad (\text{C.18})$$

Thus, we obtain the chain rule of $D_{n,\mu}^a$.

$$\begin{aligned} D_{n,\mu}^a S[U'(U)] &= \sum_{m,\nu} \frac{d}{d\epsilon} S[U'_{m,\nu} (e^{i\epsilon t^a} U_{n,\mu})] \Big|_{\epsilon \rightarrow 0} \\ &= \sum_{m,\nu} \frac{d}{d\epsilon} S[e^{i\epsilon \Delta_{n,\mu;m,\nu}^{a;b} t^b} U'_{m,\nu}] \Big|_{\epsilon \rightarrow 0} \\ &= \sum_{m,\nu} \Delta_{n,\mu;m,\nu}^{a;b} \frac{d}{d\epsilon'} S[e^{i\epsilon' t^b} U'_{m,\nu}] \Big|_{\epsilon' \rightarrow 0} \\ &= \sum_{m,\nu} \Delta_{n,\mu;m,\nu}^{a;b} D_{m,\nu}^{b'} S[U'] \end{aligned} \quad (\text{C.19})$$

In the third line, ϵ is rescaled to $\epsilon' = \epsilon \Delta_{n,\mu;m,\nu}^{a;b}$. Then, the relation between the drift

$$F'_{n,\mu} := i t^a D_{n,\mu}^{a'} S[U'(U)] \quad (\text{C.20})$$

of the smeared link and the drift $F_{n,\mu}$ of the original link is obtained.

$$\begin{aligned}
F_{n,\mu} &:= it^a D_{n,\mu}^a S[U'(U)] \\
&= it^a \sum_{m,\nu} \Delta_{n,\mu;m,\nu}^{a;b} D_{m,\nu}^b S[U'] \\
&= it^a \sum_{m,\nu} (-2i) \text{Tr} [(D_{n,\mu}^a U'_{m,\nu}) U_{m,\nu}^{-1} t^b] D_{m,\nu}^b S[U'] \\
&= -2it^a \sum_{m,\nu} \text{Tr} [\{(D_{n,\mu}^a e^{iY_{m,\nu}}) e^{-iY_{m,\nu}} + e^{iY_{m,\nu}} (D_{n,\mu}^a U_{m,\nu}) U_{m,\nu}^{-1} e^{-iY_{m,\nu}}\} F'_{m,\nu}] \\
&= -2it^a \sum_{m,\nu} \{\text{Tr} [e^{-iY_{m,\nu}} F'_{m,\nu} D_{n,\mu}^a e^{iY_{m,\nu}}] + i\delta_{nm} \delta_{\mu\nu} \text{Tr} [e^{iY_{m,\nu}} t^a e^{-iY_{m,\nu}} F'_{m,\nu}]\} \\
&= -2it^a \sum_{m,\nu} \text{Tr} [e^{-iY_{m,\nu}} F'_{m,\nu} D_{n,\mu}^a e^{iY_{m,\nu}}] + e^{-iY_{n,\mu}} F'_{n,\mu} e^{iY_{n,\mu}} \tag{C.21}
\end{aligned}$$

In the last line, the trace part vanishes since $F'_{n,\mu}$ is traceless.

$$\text{Tr} [e^{-iY_{n,\mu}} F'_{n,\mu} e^{iY_{n,\mu}}] = \text{Tr} F'_{n,\mu} = 0 \tag{C.22}$$

The derivative $D_{n,\mu}^a e^{iY_{m,\nu}}$ in the first term of (C.21) can be decomposed as follows.

$$\begin{aligned}
&\text{Tr} [e^{-iY_{m,\nu}} F'_{m,\nu} D_{n,\mu}^a e^{iY_{m,\nu}}] \\
&= \text{Tr} [e^{-iY_{m,\nu}} F'_{m,\nu} D_{n,\mu}^a (\cos \kappa_{m,\nu} \mathbb{1} + f(\kappa_{m,\nu}) iY_{m,\nu})] \\
&= \text{Tr} [e^{-iY_{m,\nu}} F'_{m,\nu} \{(f'(\kappa_{m,\nu}) iY_{m,\nu} - \sin \kappa_{m,\nu} \mathbb{1}) D_{n,\mu}^a \kappa_{m,\nu} + f(\kappa_{m,\nu}) iD_{n,\mu}^a Y_{m,\nu}\}] \tag{C.23}
\end{aligned}$$

The first term in this trace part can be further simplified by using the property $Y_{m,\nu}^2 = \kappa_{m,\nu}^2 \mathbb{1}$ of the 2×2 traceless matrix and $\text{Tr} F'_{n,\mu} = 0$.

$$\begin{aligned}
&\text{Tr} [e^{-iY_{m,\nu}} F'_{m,\nu} (f'(\kappa_{m,\nu}) iY_{m,\nu} - \sin \kappa_{m,\nu} \mathbb{1})] \\
&= \text{Tr} [(\cos \kappa_{m,\nu} \mathbb{1} - f(\kappa_{m,\nu}) iY_{m,\nu}) F'_{m,\nu} (f'(\kappa_{m,\nu}) iY_{m,\nu} - \sin \kappa_{m,\nu} \mathbb{1})] \\
&= (\kappa_{m,\nu}^2 f(\kappa_{m,\nu}) f'(\kappa_{m,\nu}) - \cos \kappa_{m,\nu} \sin \kappa_{m,\nu}) \text{Tr} F'_{m,\nu} \\
&\quad + (f'(\kappa_{m,\nu}) \cos \kappa_{m,\nu} + f(\kappa_{m,\nu}) \sin \kappa_{m,\nu}) \text{Tr} [F'_{m,\nu} iY_{m,\nu}] \\
&= \left[\left(\frac{\cos \kappa_{m,\nu}}{\kappa_{m,\nu}} - \frac{\sin \kappa_{m,\nu}}{\kappa_{m,\nu}^2} \right) \cos \kappa_{m,\nu} + \frac{\sin^2 \kappa_{m,\nu}}{\kappa_{m,\nu}} \right] \text{Tr} [F'_{m,\nu} iY_{m,\nu}] \\
&= \frac{1 - f(2\kappa_{m,\nu})}{\kappa_{m,\nu}} \text{Tr} [F'_{m,\nu} iY_{m,\nu}] \tag{C.24}
\end{aligned}$$

Since the derivative of $\kappa_{m,\nu}$ can be converted to the derivative of $Y_{m,\nu}$,

$$D_{n,\mu}^a \kappa_{m,\nu} = D_{n,\mu}^a \sqrt{\frac{1}{2} \text{Tr} Y_{m,\nu}^2} = -\frac{1}{2\kappa_{m,\nu}} \text{Tr} [iY_{m,\nu} iD_{n,\mu}^a Y_{m,\nu}] \tag{C.25}$$

all the derivatives in the trace part of (C.21) are reduced to $D_{n,\mu}^a Y_{m,\nu}$.

$$\begin{aligned}
& \text{Tr} [e^{-iY_{m,\nu}} F'_{m,\nu} D_{n,\mu}^a e^{iY_{m,\nu}}] \\
&= -\frac{1-f(2\kappa_{m,\nu})}{2\kappa_{m,\nu}^2} \text{Tr} [F'_{m,\nu} iY_{m,\nu}] \text{Tr} [iY_{m,\nu} iD_{n,\mu}^a Y_{m,\nu}] + f(\kappa_{m,\nu}) \text{Tr} [e^{-iY_{m,\nu}} F'_{m,\nu} iD_{n,\mu}^a Y_{m,\nu}] \\
&= \text{Tr} \left[\left\{ -\frac{1-f(2\kappa_{m,\nu})}{2\kappa_{m,\nu}^2} \text{Tr} [F'_{m,\nu} iY_{m,\nu}] iY_{m,\nu} + f(\kappa_{m,\nu}) e^{-iY_{m,\nu}} F'_{m,\nu} \right\} iD_{n,\mu}^a Y_{m,\nu} \right] \\
&=: \text{Tr} [\hat{\Lambda}_{m,\nu} iD_{n,\mu}^a Y_{m,\nu}]
\end{aligned} \tag{C.26}$$

Thus we the formula (C.21) is now rewritten in the following form.

$$F_{n,\mu} = -2it^a \sum_{m,\nu} \text{Tr} [\hat{\Lambda}_{m,\nu} iD_{n,\mu}^a Y_{m,\nu}] + e^{-iY_{n,\mu}} F'_{n,\mu} e^{iY_{n,\mu}} \tag{C.27}$$

$$\hat{\Lambda}_{m,\nu} = -\frac{1-f(2\kappa_{m,\nu})}{2\kappa_{m,\nu}^2} \text{Tr} [F'_{m,\nu} iY_{m,\nu}] iY_{m,\nu} + f(\kappa_{m,\nu}) e^{-iY_{m,\nu}} F'_{m,\nu} \tag{C.28}$$

For later convenience, we define the traceless matrix $\Lambda_{m,\nu}$ by subtracting the trace part from $\hat{\Lambda}_{m,\nu}$.

$$\Lambda_{m,\nu} := \text{Tr} [\hat{\Lambda}_{m,\nu} t^b] t^b = \frac{1}{2} \left(\hat{\Lambda}_{m,\nu} - \frac{1}{2} \text{Tr} [\hat{\Lambda}_{m,\nu}] \right) \tag{C.29}$$

We can replace $\hat{\Lambda}_{m,\nu}$ by $\Lambda_{m,\nu}$ in the trace part of (C.27) since the trace part of $\hat{\Lambda}_{m,\nu}$ does not contribute.

$$\begin{aligned}
-2it^a \sum_{m,\nu} \text{Tr} [\hat{\Lambda}_{m,\nu} iD_{n,\mu}^a Y_{m,\nu}] &= it^a \rho \sum_{m,\nu} \text{Tr} [\hat{\Lambda}_{m,\nu} \text{Tr} \{D_{n,\mu}^a J_{m,\nu}^{(\beta)} t^b\} t^b] \\
&= it^a \rho \sum_{m,\nu} \text{Tr} \left\{ \text{Tr} [\hat{\Lambda}_{m,\nu} t^b] t^b D_{n,\mu}^a J_{m,\nu}^{(\beta)} \right\} \\
&= it^a \rho \sum_{m,\nu} \text{Tr} [\Lambda_{m,\nu} D_{n,\mu}^a J_{m,\nu}^{(\beta)}]
\end{aligned} \tag{C.30}$$

Then the drift force

$$F_{n,\mu} = e^{-iY_{n,\mu}} F'_{n,\mu} e^{iY_{n,\mu}} + it^a \rho \sum_{m,\nu} \text{Tr} [\Lambda_{m,\nu} D_{n,\mu}^a J_{m,\nu}^{(\beta)}] \tag{C.31}$$

is completely determined by calculating the derivative of the $J_{m,\nu}^{(\beta)}$

$$\begin{aligned}
& D_{n,\mu}^a J_{m,\nu}^{(\beta)} \\
&= D_{n,\mu}^a (U_{m,\nu} \Omega_{m,\nu} - \bar{\Omega}_{m,\nu} U_{m,\nu}^{-1}) \\
&= i\delta_{nm} \delta_{\mu\nu} (t^a U_{m,\nu} \Omega_{m,\nu} + \bar{\Omega}_{m,\nu} U_{m,\nu}^{-1} t^a) + U_{m,\nu} (D_{n,\mu}^a \Omega_{m,\nu}) - (D_{n,\mu}^a \bar{\Omega}_{m,\nu}) U_{m,\nu}^{-1}
\end{aligned} \tag{C.32}$$

and also the derivatives of $\Omega_{m,\nu}$ and $\bar{\Omega}_{m,\nu}$.

$$\begin{aligned}
D_{n,\mu}^a \Omega_{m,\nu} &= i(1 - \delta_{\mu\nu}) (\delta_{n,m+\nu} t^a U_{n,\mu} U_{n+\mu-\nu,\nu}^{-1} U_{n-\nu,\mu}^{-1} - \delta_{n,m} U_{n+\nu,\mu} U_{n+\mu,\nu}^{-1} U_{n,\mu}^{-1} t^a \\
&\quad - \delta_{n,m+\nu-\mu} U_{n,\mu}^{-1} t^a U_{n-\nu,\nu}^{-1} U_{n-\nu,\mu} + \delta_{n,m-\mu} U_{n+\nu,\mu}^{-1} U_{n,\nu}^{-1} t^a U_{n,\mu}) \\
&\quad - i\delta_{\mu\nu} \sum_{\sigma(\neq\mu)} (\delta_{n,m+\sigma} U_{n+\mu-\sigma,\sigma} U_{n,\mu}^{-1} t^a U_{n-\sigma,\sigma}^{-1} + \delta_{n,m-\sigma} U_{n+\mu,\sigma}^{-1} U_{n,\mu}^{-1} t^a U_{n,\sigma})
\end{aligned} \tag{C.33}$$

$$\begin{aligned}
D_{n,\mu}^a \bar{\Omega}_{m,\nu} &= i(1 - \delta_{\mu\nu}) (\delta_{n,m} t^a U_{n,\mu} U_{n+\mu,\nu} U_{n+\nu,\mu}^{-1} - \delta_{n,m+\nu} U_{n-\nu,\mu} U_{n+\mu-\nu,\nu} U_{n,\mu}^{-1} t^a \\
&\quad - \delta_{n,m-\mu} U_{n,\mu}^{-1} t^a U_{n,\nu} U_{n+\nu,\mu} + \delta_{n,m+\nu-\mu} U_{n-\nu,\mu}^{-1} U_{n-\nu,\nu} t^a U_{n,\mu}) \\
&\quad + i\delta_{\mu\nu} \sum_{\sigma(\neq\mu)} (\delta_{n,m+\sigma} U_{n-\sigma,\sigma} t^a U_{n,\mu} U_{n+\mu-\sigma,\sigma}^{-1} + \delta_{n,m-\sigma} U_{n,\sigma}^{-1} t^a U_{n,\mu} U_{n+\mu,\sigma})
\end{aligned} \tag{C.34}$$

By substituting these expressions, the trace part of (C.31) is evaluated as follows.

$$\begin{aligned}
&\sum_{m,\nu} \text{Tr} [\Lambda_{m,\nu} D_{n,\mu}^a J_{m,\nu}^{(\beta)}] \\
&= i \text{Tr} \left[\Lambda_{n,\mu} (t^a U_{n,\mu} \Omega_{n,\mu} + \bar{\Omega}_{n,\mu} U_{n,\mu}^{-1} t^a) \right. \\
&\quad + \sum_{\nu(\neq\mu)} (\Lambda_{n-\nu,\nu} U_{n-\nu,\nu} t^a U_{n,\mu} U_{n+\mu-\nu,\nu}^{-1} U_{n-\nu,\mu}^{-1} - \Lambda_{n,\nu} U_{n,\nu} U_{n+\nu,\mu} U_{n+\mu,\nu}^{-1} U_{n,\mu}^{-1} t^a \\
&\quad \quad - \Lambda_{n+\mu-\nu,\nu} U_{n+\mu-\nu,\nu} U_{n,\mu}^{-1} t^a U_{n-\nu,\nu}^{-1} U_{n-\nu,\mu} + \Lambda_{n+\mu,\nu} U_{n+\mu,\nu} U_{n+\nu,\mu}^{-1} U_{n,\nu}^{-1} t^a U_{n,\mu}) \\
&\quad - \sum_{\sigma(\neq\mu)} (\Lambda_{n-\sigma,\mu} U_{n-\sigma,\mu} U_{n+\mu-\sigma,\sigma} U_{n,\mu}^{-1} t^a U_{n-\sigma,\sigma}^{-1} + \Lambda_{n+\sigma,\mu} U_{n+\sigma,\mu} U_{n+\mu,\sigma}^{-1} U_{n,\mu}^{-1} t^a U_{n,\sigma}) \\
&\quad - \sum_{\nu(\neq\mu)} (\Lambda_{n,\nu} t^a U_{n,\mu} U_{n+\mu,\nu} U_{n+\nu,\mu}^{-1} U_{n,\nu}^{-1} - \Lambda_{n-\nu,\nu} U_{n-\nu,\mu} U_{n+\mu-\nu,\nu} U_{n,\mu}^{-1} t^a U_{n-\nu,\nu}^{-1} \\
&\quad \quad - \Lambda_{n+\mu,\nu} U_{n,\mu}^{-1} t^a U_{n,\nu} U_{n+\nu,\mu} U_{n+\mu,\nu}^{-1} + \Lambda_{n+\mu-\nu,\nu} U_{n-\nu,\mu}^{-1} U_{n-\nu,\nu} t^a U_{n,\mu} U_{n+\mu-\nu,\nu}^{-1}) \\
&\quad \left. - \sum_{\sigma(\neq\mu)} (\Lambda_{n-\sigma,\mu} U_{n-\sigma,\sigma} t^a U_{n,\mu} U_{n+\mu-\sigma,\sigma}^{-1} U_{n-\sigma,\mu}^{-1} + \Lambda_{n+\sigma,\mu} U_{n,\sigma}^{-1} t^a U_{n,\mu} U_{n+\mu,\sigma} U_{n+\sigma,\mu}^{-1}) \right]
\end{aligned} \tag{C.35}$$

We can combine the sum over ν and σ . By reordering the matrices and factoring out t^a ,

the trace part is further simplified.

$$\begin{aligned}
& \sum_{m,\nu} \text{Tr} [\Lambda_{m,\nu} D_{n,\mu}^a J_{m,\nu}^{(\beta)}] \\
&= i \text{Tr} \left[\left\{ U_{n,\mu} \Omega_{n,\mu} \Lambda_{n,\mu} + \Lambda_{n,\mu} \bar{\Omega}_{n,\mu} U_{n,\mu}^{-1} \right. \right. \\
&+ \sum_{\nu(\neq\mu)} (U_{n,\mu} U_{n+\mu-\nu,\nu}^{-1} U_{n-\nu,\mu}^{-1} \Lambda_{n-\nu,\nu} U_{n-\nu,\nu} - \Lambda_{n,\nu} U_{n,\nu} U_{n+\nu,\mu} U_{n+\mu,\nu}^{-1} U_{n,\mu}^{-1} \\
&- U_{n-\nu,\nu}^{-1} U_{n-\nu,\mu} \Lambda_{n+\mu-\nu,\nu} U_{n+\mu-\nu,\nu} U_{n,\mu}^{-1} + U_{n,\mu} \Lambda_{n+\mu,\nu} U_{n+\mu,\nu} U_{n+\nu,\mu}^{-1} U_{n,\nu}^{-1} \\
&- U_{n-\nu,\nu}^{-1} \Lambda_{n-\nu,\mu} U_{n-\nu,\mu} U_{n+\mu-\nu,\nu} U_{n,\mu}^{-1} - U_{n,\nu} \Lambda_{n+\nu,\mu} U_{n+\nu,\mu} U_{n+\mu,\nu}^{-1} U_{n,\nu}^{-1} \\
&- U_{n,\mu} U_{n+\mu,\nu} U_{n+\nu,\mu}^{-1} U_{n,\nu}^{-1} \Lambda_{n,\nu} + U_{n-\nu,\nu}^{-1} \Lambda_{n-\nu,\nu} U_{n-\nu,\mu} U_{n+\mu-\nu,\nu} U_{n,\mu}^{-1} \\
&+ U_{n,\nu} U_{n+\nu,\mu} U_{n+\mu,\nu}^{-1} \Lambda_{n+\mu,\nu} U_{n,\mu}^{-1} - U_{n,\mu} U_{n+\mu-\nu,\nu}^{-1} \Lambda_{n+\mu-\nu,\nu} U_{n-\nu,\mu}^{-1} U_{n-\nu,\nu} \\
&\left. \left. - U_{n,\mu} U_{n+\mu-\nu,\nu}^{-1} U_{n-\nu,\mu}^{-1} \Lambda_{n-\nu,\mu} U_{n-\nu,\nu} - U_{n,\mu} U_{n+\mu,\nu} U_{n+\nu,\mu}^{-1} \Lambda_{n+\nu,\mu} U_{n,\nu}^{-1} \right) \right\} t^a \Big] \quad (\text{C.36})
\end{aligned}$$

Finally, we obtain the explicit formula of the map $F'_{n,\mu} \rightarrow F_{n,\mu}$.

$$\begin{aligned}
F_{n,\mu} &= e^{-iY_{n,\mu}} F'_{n,\mu} e^{iY_{n,\mu}} + it^a \rho \sum_{m,\nu} \text{Tr} [\Lambda_{m,\nu} D_{n,\mu}^a J_{m,\nu}^{(\beta)}] \\
&= e^{-iY_{n,\mu}} F'_{n,\mu} e^{iY_{n,\mu}} + \rho \text{Tr} [X_{n,\mu} t^a] t^a \\
&= e^{-iY_{n,\mu}} F'_{n,\mu} e^{iY_{n,\mu}} + \frac{\rho}{2} \left(X_{n,\mu} - \frac{1}{2} \text{Tr} [X_{n,\mu}] \right) \quad (\text{C.37})
\end{aligned}$$

$$\begin{aligned}
X_{n,\mu} &:= -U_{n,\mu}\Omega_{n,\mu}\Lambda_{n,\mu} - \Lambda_{n,\mu}\bar{\Omega}_{n,\mu}U_{n,\mu}^{-1} \\
&+ \sum_{\nu(\neq\mu)} (U_{n,\mu}U_{n+\mu,\nu}U_{n+\nu,\mu}^{-1}U_{n,\nu}^{-1}\Lambda_{n,\nu} + \Lambda_{n,\nu}U_{n,\nu}U_{n+\nu,\mu}U_{n+\mu,\nu}^{-1}U_{n,\mu}^{-1} \\
&\quad + U_{n,\mu}U_{n+\mu,\nu}U_{n+\nu,\mu}^{-1}\Lambda_{n+\nu,\mu}U_{n,\nu}^{-1} + U_{n,\nu}\Lambda_{n+\nu,\mu}U_{n+\nu,\mu}U_{n+\mu,\nu}^{-1}U_{n,\mu}^{-1} \\
&\quad - U_{n,\mu}\Lambda_{n+\mu,\nu}U_{n+\mu,\nu}U_{n+\nu,\mu}^{-1}U_{n,\nu}^{-1} - U_{n,\nu}U_{n+\nu,\mu}U_{n+\mu,\nu}^{-1}\Lambda_{n+\mu,\nu}U_{n,\mu}^{-1} \\
&\quad + U_{n,\mu}U_{n+\mu-\nu,\nu}^{-1}\Lambda_{n+\mu-\nu,\nu}U_{n-\nu,\mu}^{-1}U_{n-\nu,\nu} + U_{n-\nu,\nu}^{-1}U_{n-\nu,\mu}\Lambda_{n+\mu-\nu,\nu}U_{n+\mu-\nu,\nu}U_{n,\mu}^{-1} \\
&\quad + U_{n,\mu}U_{n+\mu-\nu,\nu}^{-1}U_{n-\nu,\mu}^{-1}\Lambda_{n-\nu,\mu}U_{n-\nu,\nu} + U_{n-\nu,\nu}^{-1}\Lambda_{n-\nu,\mu}U_{n-\nu,\mu}U_{n+\mu-\nu,\nu}U_{n,\mu}^{-1} \\
&\quad - U_{n,\mu}U_{n+\mu-\nu,\nu}^{-1}U_{n-\nu,\mu}^{-1}\Lambda_{n-\nu,\nu}U_{n-\nu,\nu} - U_{n-\nu,\nu}^{-1}\Lambda_{n-\nu,\nu}U_{n-\nu,\mu}U_{n+\mu-\nu,\nu}U_{n,\mu}^{-1}) \quad (\text{C.38})
\end{aligned}$$

D Topological charge after the smearing

We can define the topological charge which is close to an integer by using the stout smearing as discussed in Section 4.4. We present how the distribution of the topological charge depends on the smearing parameter ρ . For simplicity, we fix the number of smearing steps $N_\rho = 40$ in this discussion. Note that we can see similar behaviors for different values of N_ρ as long as it is large enough. If N_ρ is too small, we cannot obtain an appropriate distribution of the topological charge for any ρ .

In Fig. D.1 we show typical distributions of the topological charge defined by (4.24) for various values of ρ at $\theta = 0$. The number of smearing step is fixed to $N_\rho = 40$. The lattice volume is $V = 16^3 \times 4$ and the temperature is $T/T_{\text{dec}}(0) = 1.0$. The distribution looks like the Gaussian distribution for $\rho = 0.05$, which means that the effect of smearing is not enough. For $\rho = 0.10$ we can see some peaks of the distribution, and they become clearer for $\rho = 0.15$. Thus, the topological property of the gauge field is recovered for $\rho \simeq 0.15$. The distribution suddenly collapses to the single peak for larger ρ as we can see in the result for $\rho = 0.20$.

We also tried some other values of ρ and decided to use $\rho = 0.15$ for the actual calculations on the $16^3 \times 4$ lattice. Since the appropriate value of ρ depends on the lattice size, we use the different value $\rho = 0.09$ for the $20^3 \times 5$ lattice. In fact, there is an ambiguity in the determination of the smearing parameters. One of the possible ways to eliminate this ambiguity is the $\rho \rightarrow 0$ extrapolation of observables in the scaling region of ρ .

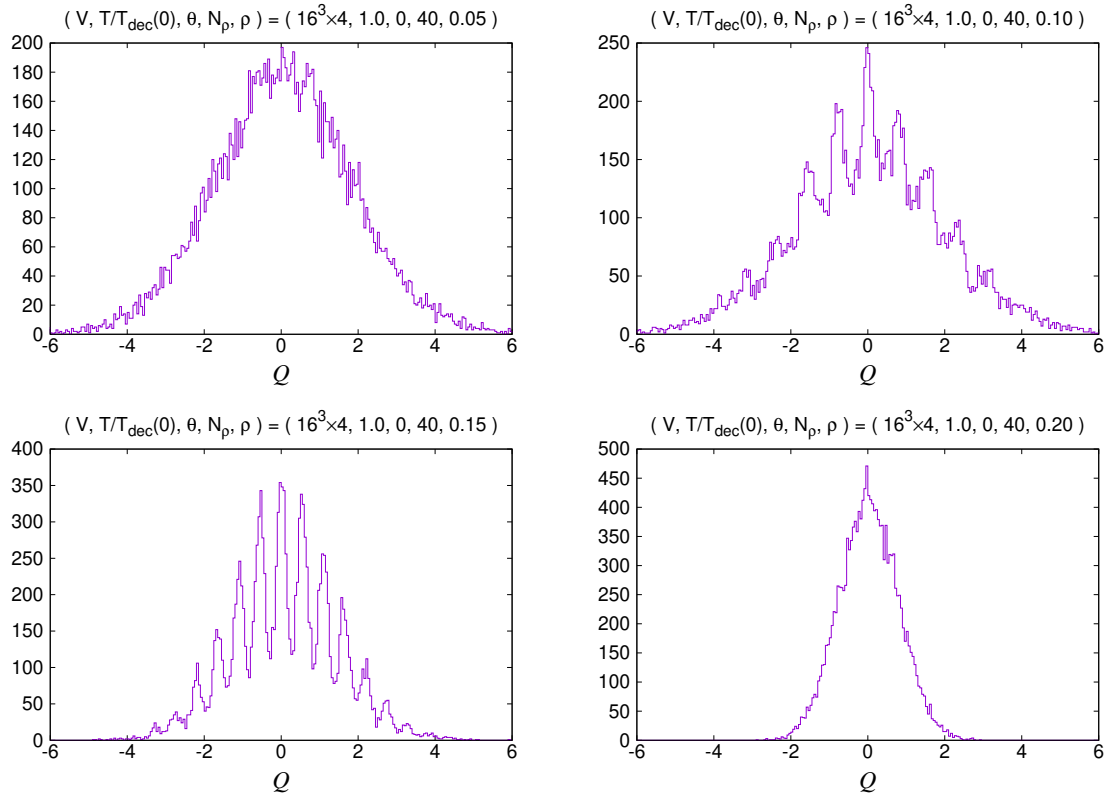


Figure D.1: The distribution of the topological charge defined by (4.24) at $T/T_{\text{dec}}(0) = 1.0$ for $\theta = 0$ on the 16×4 lattice. We set the smearing parameters to $N_\rho = 40$ with $\rho = 0.05$ (Top Left), 0.10 (Top Right), 0.15 (Bottom Left) and 0.20 (Bottom Right).

References

- [1] Davide Gaiotto, Anton Kapustin, Zohar Komargodski, and Nathan Seiberg. Theta, time reversal, and temperature. *JHEP*, 05:091, 2017.
- [2] John R. Klauder. Coherent state Langevin equations for canonical quantum systems with applications to the quantized Hall effect. *Phys. Rev.*, A29:2036–2047, 1984.
- [3] G. Parisi. On complex probabilities. *Phys. Lett.*, 131B:393–395, 1983.
- [4] Keitaro Nagata, Jun Nishimura, and Shinji Shimasaki. Argument for justification of the complex Langevin method and the condition for correct convergence. *Phys. Rev.*, D94(11):114515, 2016.
- [5] Mitsuaki Hirasawa, Akira Matsumoto, Jun Nishimura, and Atis Yosprakob. Complex Langevin analysis of 2D $U(1)$ gauge theory on a torus with a θ term. *JHEP*, 09:023, 2020.
- [6] U.J. Wiese. Numerical simulation of lattice θ vacua: The 2- d $u(1)$ gauge theory as a test case. *Nucl.Phys.B*, 318:153–175, 1989.
- [7] B. E. Rusakov. Loop averages and partition functions in $U(N)$ gauge theory on two-dimensional manifolds. *Mod. Phys. Lett.*, A5:693–703, 1990.
- [8] Claudio Bonati and Paolo Rossi. Topological susceptibility of two-dimensional $U(N)$ gauge theories. *Phys. Rev.*, D99(5):054503, 2019.
- [9] Akira Matsumoto, Kohta Hatakeyama, Mitsuaki Hirasawa, Masazumi Honda, Yuta Ito, Jun Nishimura, and Atis Yosprakob. A new technique for solving the freezing problem in the complex Langevin simulation of 4D $SU(2)$ gauge theory with a theta term. In *38th International Symposium on Lattice Field Theory*, 12 2021.
- [10] P. Di Vecchia, K. Fabricius, G.C. Rossi, and G. Veneziano. Preliminary Evidence for $U(1)$ -A Breaking in QCD from Lattice Calculations. pages 426–442, 5 1981.
- [11] Colin Morningstar and Mike J. Peardon. Analytic smearing of $SU(3)$ link variables in lattice QCD. *Phys. Rev. D*, 69:054501, 2004.
- [12] Ryuichiro Kitano, Norikazu Yamada, and Masahito Yamazaki. Is $N = 2$ Large? *JHEP*, 02:073, 2021.
- [13] Ryuichiro Kitano, Ryutaro Matsudo, Norikazu Yamada, and Masahito Yamazaki. Peeking into the θ vacuum. *Phys. Lett. B*, 822:136657, 2021.
- [14] Shi Chen, Kenji Fukushima, Hiromichi Nishimura, and Yuya Tanizaki. Deconfinement and \mathcal{CP} breaking at $\theta = \pi$ in Yang-Mills theories and a novel phase for $SU(2)$. *Phys. Rev. D*, 102(3):034020, 2020.

- [15] Gert Aarts, Erhard Seiler, and Ion-Olimpiu Stamatescu. The Complex Langevin method: When can it be trusted? *Phys. Rev.*, D81:054508, 2010.
- [16] Gert Aarts, Frank A. James, Erhard Seiler, and Ion-Olimpiu Stamatescu. Complex langevin: Etiology and diagnostics of its main problem. *Eur.Phys.J.C*, 71:1756, 2011.
- [17] Keitaro Nagata, Jun Nishimura, and Shinji Shimasaki. Justification of the complex Langevin method with the gauge cooling procedure. *PTEP*, 2016(1):013B01, 2016.
- [18] Jun Nishimura and Shinji Shimasaki. New insights into the problem with a singular drift term in the complex Langevin method. *Phys. Rev.*, D92(1):011501, 2015.
- [19] Gert Aarts, Erhard Seiler, Denes Sexty, and Ion-Olimpiu Stamatescu. Complex Langevin dynamics and zeroes of the fermion determinant. *JHEP*, 05:044, 2017. [Erratum: JHEP 01, 128 (2018)].
- [20] A. Mollgaard and K. Splittorff. Complex Langevin Dynamics for chiral Random Matrix Theory. *Phys. Rev. D*, 88(11):116007, 2013.
- [21] Jeff Greensite. Comparison of complex Langevin and mean field methods applied to effective Polyakov line models. *Phys. Rev. D*, 90(11):114507, 2014.
- [22] Erhard Seiler, Denes Sexty, and Ion-Olimpiu Stamatescu. Gauge cooling in complex Langevin for QCD with heavy quarks. *Phys. Lett.*, B723:213–216, 2013.
- [23] Zhenning Cai, Yana Di, and Xiaoyu Dong. How does Gauge Cooling Stabilize Complex Langevin? *Commun. Comput. Phys.*, 27(5):1344–1377, 2020.
- [24] Gert Aarts, Frank A. James, Erhard Seiler, and Ion-Olimpiu Stamatescu. Adaptive stepsize and instabilities in complex Langevin dynamics. *Phys. Lett.*, B687:154–159, 2010.
- [25] Dénes Sexty. Calculating the equation of state of dense quark-gluon plasma using the complex Langevin equation. *Phys. Rev. D*, 100(7):074503, 2019.
- [26] Massimo D’Elia and Francesco Negro. θ dependence of the deconfinement temperature in Yang-Mills theories. *Phys. Rev. Lett.*, 109:072001, 2012.
- [27] Massimo D’Elia and Francesco Negro. Phase diagram of Yang-Mills theories in the presence of a θ term. *Phys. Rev. D*, 88(3):034503, 2013.
- [28] Gyan Bhanot and Francois David. The Phases of the O(3) σ Model for Imaginary θ . *Nucl. Phys. B*, 251:127–140, 1985.
- [29] J. Engels, F. Karsch, and K. Redlich. Scaling properties of the energy density in SU(2) lattice gauge theory. *Nucl. Phys. B*, 435:295–310, 1995.
- [30] Jean-Michel Drouffe and Jean-Bernard Zuber. Strong coupling and mean field methods in lattice gauge theories. *Phys. Rept.*, 102:1, 1983.